NASA/CR-20240007834



Hybrid Thermally Efficient Core (HyTEC) HyTEC Phase 1—Advanced Aerodynamics Final Report

Kevin Hetzel, Julio Estrella, and Kunal Bhanushali GE Aerospace, Evendale, Ohio

NASA STI Program Report Series

Since its founding, NASA has been dedicated to the advancement of aeronautics and space science. The NASA scientific and technical information (STI) program plays a key part in helping NASA maintain this important role.

The NASA STI program operates under the auspices of the Agency Chief Information Officer. It collects, organizes, provides for archiving, and disseminates NASA's STI. The NASA STI program provides access to the NTRS Registered and its public interface, the NASA Technical Reports Server, thus providing one of the largest collections of aeronautical and space science STI in the world. Results are published in both non-NASA channels and by NASA in the NASA STI Report Series, which includes the following report types:

• TECHNICAL PUBLICATION.

Reports of completed research or a major significant phase of research that present the results of NASA Programs and include extensive data or theoretical analysis. Includes compilations of significant scientific and technical data and information deemed to be of continuing reference value. NASA counterpart of peer-reviewed formal professional papers but has less stringent limitations on manuscript length and extent of graphic presentations.

TECHNICAL MEMORANDUM.

Scientific and technical findings that are preliminary or of specialized interest, e.g., quick release reports, working papers, and bibliographies that contain minimal annotation. Does not contain extensive analysis.

CONTRACTOR REPORT. Scientific and technical findings by NASA-sponsored contractors and grantees.

CONTRACTOR REPORT. Scientific and technical findings by NASA-sponsored contractors and grantees.

CONFERENCE PUBLICATION. Collected papers from scientific and technical conferences, symposia, seminars, or other meetings sponsored or co-sponsored by NASA.

SPECIAL PUBLICATION. Scientific, technical, or historical information from NASA programs, projects, and missions, often concerned with subjects having substantial public interest.

TECHNICAL TRANSLATION. English-language translations of foreign scientific and technical material pertinent to NASA's mission.

Specialized services also include organizing and publishing research results, distributing specialized research announcements and feeds, providing information desk and personal search support, and enabling data exchange services.

For more information about the NASA STI program, see the following:

 Access the NASA STI program home page at http://www.sti.nasa.gov

NASA/CR-20240007834



Hybrid Thermally Efficient Core (HyTEC) HyTEC Phase 1—Advanced Aerodynamics Final Report

Kevin Hetzel, Julio Estrella, and Kunal Bhanushali GE Aerospace, Evendale, Ohio

Prepared under Contract 80GRC021CA006

National Aeronautics and Space Administration

Glenn Research Center Cleveland, Ohio 44135

Acknowledgments

This material is based upon work supported under NASA contract number 80GRC021CA006 with Ian Park (NASA Glenn) as contracting officer and Doug Thurman (NASA Glenn) as technical monitor. The authors are grateful for the following individuals who made significant contributions to the project and allowed for the successful execution and completion of the task objectives:

GE Aerospace: Sophia Moak, Ruby Precourt, Paul Vitt, Lyle Dailey, Scott Carson, Connor Shirley, Tim Swenson, Kathleen Brossart, Matias Oyarzun, John Davis, Nathan Hermanson, Randy Kuntz, Adam Stammen, Johnny Deleon, Scott Keller, Brad Lusk, Bob Groves, Alain Ouellette, and Sanjiv Tewani

Notre Dame Turbomachinery Laboratory: Josh Cameron, Doug Wise, Ethan Perez, Ryan Rivard, Tom Neiter, David Hipskind, and Jim Hock

NASA Glenn: Paul Giel, Kyle Monaghan, Michael Perez, Garret Baker, Joseph Wisniewski, Jacob Jaksic, Jonathan Mitchell, Doug Thurman, Tim Dunlap, Joshua Abood, Leah Nakley, and Laura Evans

The authors also thank numerous other individuals from GE Aerospace, Notre Dame Turbomachinery Laboratory, and NASA for their technical guidance. This work was sponsored by the HyTEC Project at NASA Glenn.

This work was sponsored by the Advanced Air Vehicles Program at the NASA Glenn Research Center.

Trade names and trademarks are used in this report for identification only. Their usage does not constitute an official endorsement, either expressed or implied, by the National Aeronautics and Space Administration.

Level of Review: This material has been technically reviewed by expert reviewer(s).

This report is available in electronic form at https://www.sti.nasa.gov/ and https://ntrs.nasa.gov/

NASA STI Program/Mail Stop 050 NASA Langley Research Center Hampton, VA 23681-2199

Contents

	itents	
List	of Figures	V
List	of Tables	ix
	of Acronyms	
	cutive Summary	
	Introduction	
	Technology Background	
	2.1 High Lift/Low Solidity Airfoils	
	2.2 Advanced Blade Tips	
	2.3 Endwall Contouring	
	2.4 Aerothermal Ceramic Matrix Composite Stage 2 Nozzle	
	Aerodynamic Design	
	3.1 CW22 Stage 2 Nozzle	
	3.2 CW22 Stage 1 Blade	
	3.3 Transonic Research Turbine	
	3.3.1 Aero Design Overview	
	3.3.2 Design Procedure	
	3.3.3 Baseline Design	
	3.3.4 Low Solidity Design	
	3.3.5 Advanced Tips - Flare & Winglet Design	
	3.3.6 Hub Platform Contouring Design	
	3.4 Stage 2 Nozzle Annular	
4.	Test Program.	
	4.1 CW22 Stage 2 Nozzle	
	4.1.1 Objectives	
	4.1.2 Test Facility	
	4.1.2.1 Instrumentation	
	4.1.2.2 Background Oriented Schneren 4.1.2.3 Facility Test Enabling Hardware	
	4.1.2.5 Facility Test Enabling Hardware 4.1.3 Test Plan	
	4.1.4 Test Article Design	
	4.1.5 Summary of Completed Testing	
	4.2 CW22 Stage 1 Blade	
	4.2.1 Test Objective	
	4.2.2 Test Gojective 4.2.2 Test Facility.	
	4.2.2.1 Cascade Instrumentation	
	4.2.2.2 Pressure Sensitive Paint Instrumentation	
	4.2.3 Test Plan	
	4.2.4 Test Article Design	
	4.2.5 Summary of Completed Testing	
	4.3 Transonic Research Turbine	
	4.3.1 Objectives	
	4.3.2 Test Facility	
	4.3.2.1 Instrumentation	
	4.3.3 Test Plan	
	4.3.3.1 Test Operations	
	4.3.4 Test Article Design Summary	
	4.3.5 Summary of Completed Testing	
	4.4 Stage 2 Nozzle Annular	
	4.4.1 Test Objectives	
	4.4.2 Test Facility	

	4.4.2.1 Facility and Rig Design.	39
	4.4.2.2 Instrumentation	41
	4.4.3 Test Plan	41
	4.4.4 Test Articles	42
	4.4.5 Summary of Completed Testing	42
5.	Test Results and Analysis	
	5.1 CW22 Stage 2 Nozzle	
	5.1.1 Data Summary	
	5.1.2 Data Acquisition and Reduction	
	5.1.3 Rig Aerodynamic Validation	
	5.1.3.1 Inlet Characterization	44
	5.1.3.2 Cascade Operating Conditions	
	5.1.3.3 As-Tested Hardware vs. Design Intent	
	5.1.3.4 Probe Data Corrections	
	5.1.4 Uncooled Aerodynamic Data Summary	
	5.1.4.1 Design Point Performance	50
	5.1.4.2 Off-Design Performance & Derivatives	
	5.1.5 Cooled Aerodynamic Data Summary	
	5.1.5.1 Design Point Performance	
	5.1.5.2 Off-Design Performance & Derivatives	
	5.1.5.3 Background Oriented Schlieren	
	5.1.6 Aerodynamic Design Validation	
	5.1.6.1 Prediction Models, Uncooled	
	5.1.6.2 Prediction Models, Cooled	
	5.1.7 Cascade Test Results Conclusion	
	5.1.7.1 Performance Conclusions	
	5.2 CW22 Stage 1 Blade	
	5.2.1 Data Acquisition and Reduction	
	5.2.2 Rig Aerodynamic Validation	
	5.2.2.1 Inlet Characterization	
	5.2.2.2 As Tested Hardware vs. Design Intent	70
	5.2.2.3 Probe Mach Number Correction	70
	5.2.3 Design Point Performance	
	5.2.3.1 Probe Mach Number Correction	
	5.2.3.2 Variation with Incidence	
	5.2.3.3 Stagnation Region Assessment	75
	5.2.4 Off-Design Performance and Derivatives	76
	5.2.4.1 Reynolds Number Derivative	76
	5.2.4.2 Pressure Ratio Derivative	77
	5.2.5 Pressure Sensitive Paint Data	77
	5.2.6 Test Results Conclusion	78
	5.3 Transonic Research Turbine	79
	5.3.1 Data Summary	79
	5.3.2 Data Acquisition and Reduction	
	5.3.2.1 Data Acquisition Systems	
	5.3.2.2 Data Acquisition Strategy	
	5.3.2.3 Data Reduction.	
	5.3.3 Rig Aerodynamic Validation	
	5.3.3.1 Aerodynamic Quantities	
	5.3.3.2 Tip Clearance Variation	
	5.3.3.3 Purge Mass Flow Issues	
	5.3.4 Aerodynamic Data Discussion	
	5.3.4.1 Low Solidity	
	C.C LOT SOMETH THE CONTRACT OF THE CONTRA	

	5.3.4.2 Hub Platform Contouring	92
	5.3.4.3 Tip Treatment	
	5.3.5 Test Results Conclusion	95
	5.4 Stage 2 Nozzle Annular	95
	5.4.1 Data Summary	
	5.4.2 Data Acquisition and Reduction	
	5.4.2.1 Data Acquisition Approach	
	5.4.2.2 Data Reduction Approach	
	5.4.3 Rig Aero Validation	97
	5.4.3.1 Inlet Characterization	97
	5.4.3.2 Cascade Operating Conditions	98
	5.4.3.3 As Tested Hardware vs Design Intent	99
	5.4.3.4 Data Corrections	
	5.4.3.5 Sources of Additional Uncertainty	99
	5.4.4 Data Discussion and Comparison to Analytical Models	100
	5.4.4.1 Flow Function Results	100
	5.4.4.2 Nozzle Performance Results	
	5.4.5 Test Conclusions	108
6.	Assessment Against Technical Performance Measures and Key Performance Parameters	
	6.1 Methodology	109
	6.2 Assessments	109
	6.2.1 Low Solidity	
	6.2.2 Advanced Tip Treatment	
	6.2.3 Platform Contouring	
	6.2.4 Compact Core Stage 2 Nozzle	
7.	Technology Readiness Assessment	
	7.1 Low Solidity	
	7.2 Advanced Tip Treatments	
	7.3 Platform Contouring	
	7.4 Compact Core Stage 2 Nozzle	
8.	Technology Maturity Plan	
	Conclusion	
Αp	pendix A – Lessons Learned	
Re	ferences	121

List of Figures	
Figure 1: View of Three Solidity Configurations	4
Figure 2: Blisk Configurations.	
Figure 3: Rig Flowpath Cross-section	
Figure 4: Stage 1 Vane 3D Design.	
Figure 5: Stage 1 Blade 3D Design	
Figure 6: Low Solidity Stage 1 Blade 3D Design	
Figure 7: Pitchline Baseline vs. Low Solidity Loading (50% span)	
Figure 8: Pre-Test Predictions of Low Solidity to Baseline	
Figure 9: Rainbow with Tip Features	
Figure 10: Pre-Test Predictions of Advanced Tip	
Figure 11: Platform Contouring Flow Physics	
Figure 12: Rainbow with and without Platform Contouring	
Figure 13: Pre-Test Predictions of Platform Contouring	
Figure 14: Airfoil Section of Annular Test Article	15
Figure 15: Annular S2N Loading Comparison, 50% Span	
Figure 16: Downstream Radial Profile, Total Pressure	
Figure 17: NASA Glenn Transonic Turbine Blade Cascade with Feature Callouts	
Figure 18: NASA Glenn Transonic Turbine Blade Cascade	
Figure 19: NASA Glenn Transonic Turbine Blade Cascade Cross Section	
Figure 20: S2N Measurement Set-Up Cross Section	
Figure 21: Static Pressure Instrumentation on Baseline Nozzle	
Figure 22: Five-Hole Probe Specifications	
Figure 23: BOS Installation in CW-22	
Figure 24: CW22 Operating Envelope	
Figure 25: Cooled Nozzle Configuration with Three Cooling Rows	
Figure 26: Flowchart Demonstrating Data Transfer Process	
Figure 27: Uninstrumented Test Articles for (a) Baseline (b) Medium and (c) Low Solidity	
Figure 28: Instrumented Test Articles for Cooled (a) Medium and (b) Low Solidity	
Figure 29: S1B Measurement Set-Up Cross Section	
Figure 30: Baseline Blade Static Pressure Instrumentation - Close-up of Ps Taps	
Figure 31: PSP Setup and Quartz Window Specifications	
Figure 32: Rails and Damper for Borescope Stability	
Figure 33: Painted Instrumented Airfoil	
Figure 34: Sidewall comparison between East and West (x3 for each different solidity build)	
Figure 35: TRT Test Cell Schematic	
Figure 36: TRT Rig Instrumentation Layout	
Figure 37: High Level Test Plan	
Figure 38: TRT Control Room.	
Figure 39: Baseline Blisk 3D FEM Results	
Figure 40: Main Airflow Choked Flow Venturis	
Figure 41 :Test Rig Cross Section	
Figure 42: 5HP Installed on Aft Side of Rig	
Figure 43: Modeled and installed instrumentations	
Figure 44: Variable Upper and Lower Gaps for Inlet Control	
Figure 45: Before and After Inlet Characterization	
Figure 46: Nonzero Cp _T Highlighted in Inlet Profile	
Figure 47: Kiel Probe and Inlet Traverse Location	
Figure 48: Direction of 5HP Travel to Visualize Bow Wave	
Figure 49: Loading Differences Caused by Traverse Bow Wave	
Figure 50: Traverse Data, with Freestream Region Highlighted	
Figure 51: Design Point Trends, Uncooled Solidity Nozzles	
, , ,	

Figure 52: Design Point, Wake Plots	51
Figure 53: Design Point, Airfoil Loadings	51
Figure 54: Reynolds Number Variation at Negative Incidence	52
Figure 55: Reynolds Number Variation at Design Incidence	52
Figure 56: Pressure Ratio Variation at Negative Incidence	53
Figure 57: Pressure Ratio Variation at Design Incidence	53
Figure 58: Pressure Ratio Variation at Positive Incidence	53
Figure 59: Inlet Angle Variation at Positive Incidence	
Figure 60: Traverse Wake Data for Zero Turbulence Run	
Figure 61: Design Point Trends, Cooled Solidity Nozzles	
Figure 62: Design Point Wake Plots, All Holes Open	56
Figure 63: Design Point Airfoil Loadings, All Holes Open	56
Figure 64: Design Point Airfoil Loadings, Forward Holes Open	57
Figure 65: Design Point Airfoil Loadings, Middle Holes Open	
Figure 66: Design Point Airfoil Loadings, Aft Holes Open	
Figure 67: Cooling Design Point Repeatability	58
Figure 68: Off-Design Trends, Low Solidity	59
Figure 69: Off-Design Wake Plots, Low Solidity	59
Figure 70: Off-Design Loadings, Low Solidity, All Holes Open	60
Figure 71: Off-Design Trends, Medium Solidity	
Figure 72: Off-Design Wake Plots, Medium Solidity	
Figure 73: Off-Design Loadings, Medium Solidity, All Holes Open	61
Figure 74: Magnitude of Density Gradient Diagram	
Figure 75: BOS Results at Aerodynamic Design Point	62
Figure 76: BOS Reynolds Variation for Low Solidity Cooled Nozzle	63
Figure 77: BOS Reynolds Variation for Medium Solidity Cooled Nozzle	
Figure 78: BOS Cascade Pressure Ratio Variation for Low Solidity Cooled Nozzle	63
Figure 79: BOS Cascade Pressure Ratio Variation for Medium Solidity Cooled Nozzle	64
Figure 80: BOS Coolant Pressure Ratio Variation for Low Solidity Cooled Nozzle	64
Figure 81: BOS Coolant Pressure Ratio Variation for Medium Solidity Cooled Nozzle	64
Figure 82: Comparison to CFD, Reynolds Number Variation	65
Figure 83: Comparison to CFD, Overall Pressure Ratio Variation	66
Figure 84: Comparison to CFD, Inlet Angle Variation	
Figure 85: Improvement of Exit Swirl Angle from Adjust Inlet Characterization on Baseline Blade	69
Figure 86: Cascade Blockage Plate Configurations for Low Solidity Blade	
Figure 87: Design Point Trends	71
Figure 88: Design Point, Wake Plots	71
Figure 89: Design Point, Airfoil Loadings	
Figure 90: Blade Loading Variance with Incidence at Design PR/Re	72
Figure 91: Baseline Wake Variance with Incidence	73
Figure 92: Baseline Exit Angle Variance with Incidence	73
Figure 93: Medium Solidity Wake Variance with Incidence	74
Figure 94: Medium Solidity Exit Angle Variance with Incidence	74
Figure 95: Low Solidity Wake Variance with Incidence	75
Figure 96: Low Solidity Exit Angle Variance with Incidence	75
Figure 97: Close-up of Stagnation Region in Blade Loading	76
Figure 98: Reynolds Number Variation at Design PR	
Figure 99: Pressure Ratio Variation at Design Reynolds Number	
Figure 100: PSP Data for selected conditions	
Figure 101: FRAP data reduction process	
Figure 102: Baseline Blisk ADP Exit Total Pressure Profile from Rake and FRAP Measurements	
Figure 103: Magnetic Bearing W/V Axis Transformation to Cartesian X/Y Axis	
Figure 104: Rotor Whirl Linear Relationship to Magnetic Bearing Radial Displacement	

Figure 105: Calculated Rotor Whirl Pattern for Baseline Blisk at ADP	87
Figure 106: Post-test purge leakage checks – FWD tip purge and AFT hub purge leakages	89
Figure 107: Baseline and Low Solidity Blisk Cp _T Contours	
Figure 108: CFD and FRAP ΔCp _T Profiles – Low Solidity Blisk Compared to Baseline Blisk	91
Figure 109: No Platform Contouring and Platform Contouring Blisk CpT Contours	92
Figure 110: CFD and FRAP ΔCp _T Profiles – Hub Platform Contouring	93
Figure 111: Baseline and Tip Treatment Rainbow B4 Blisk Cp _T Contours	94
Figure 112: CFD and FRAP ΔCp _T Profiles – Tip Treatment Compared to Baseline	94
Figure 113: Inlet Plenum Pressures, Design Point	97
Figure 114: Inlet Plenum Temperature Distribution	98
Figure 115: Reported Downstream Pressure as a function of Traverse Probe Position	98
Figure 116: S2N Flow Function, Full Pressure Sweep	100
Figure 117: S2N Flow Function, Near Design Point	101
Figure 118: Effect of Cooling on S2N Flow Function	101
Figure 119: Baseline Contour, PT	102
Figure 120: Baseline Contour, Air Exit Angle	102
Figure 121: Low Solidity Contour, PT	103
Figure 122: Low Solidity Contour, Air exit angle	103
Figure 123: S2N Solidity Comparison of Loss	104
Figure 124: Radial Profile, Baseline Vs Low Solidity	105
Figure 125: Radial Profile, ΔCp _T , Solidity	105
Figure 126: Baseline Loss for Various Cooling Levels	106
Figure 127: Low Solidity Loss for Various Cooling Levels	106
Figure 128: Delta Loss, Nominal to No Cooling	107
Figure 129: S2N Exit Air Angles	108
Figure 130: Fiducials and Static Pressure Taps Close-Up	117
Figure 131: Wind-off Condition (left) and Wind-on Condition with Vibration (right)	117

List of Tables

Table 1: HyTEC Project KPPs	1
Table 2: HPT Aerodynamics TPMs	
Table 3: Engine vs. TRT Rig Conditions	
Table 4: Low Solidity Pre-Test Performance Delta	
Table 5: Advanced Tip Pre-Test Performance Deltas	
Table 6: Hub Platform Contouring Pre-Test Performance Delta for Both Design Success Criteria	
Table 7: Design Deltas, Baseline vs Low Solidity	
Table 8: Solidity Test Cases and Derivative Studies	
Table 9: Cooling Test Cases and Derivative Studies	
Table 10: Final Executed Test Plan.	
Table 11: Test Matrix Controlled Parameters	
Table 12: Quantitative Comparison of 3 Tested Solidity Blades	31
Table 13: Final Executed Test Plan.	
Table 14: Mechanical Design Requirements & Criteria	38
Table 15: S2N Annular Test Matrix	
Table 16: S2N Annular Final Executed Test Plan	
Table 17: Reported Operating Conditions Variation Assessment	
Table 18: Throat Measurements for Uncooled Test Articles	
Table 19: Design Point Airfoil Turning, Delta from Pre-Test CFD.	51
Table 20: Cooled Design Point Airfoil Turning, Delta from Uncooled	58
Table 21: Comparison to CFD with Post-Throat Cooling	
Table 22: Performance Results for TPM Estimates	
Table 23: Design Point Airfoil Turning	
Table 24: Performance Results for TPM Estimates	
Table 25: Overview of TRT DAQ Systems and Capabilities	
Table 26: Monte-Carlo Simulation 2-sigma Uncertainty Values	82
Table 27: Uncertainty in ΔCp_T Comparison	83
Table 28: Baseline Blisk ADP Operating Condition	83
Table 29: Low Solidity Blisk ADP Operating Condition Compared to Baseline Blisk	84
Table 30: Rainbow B5 Blisk ADP Operating Condition Compared to Baseline Blisk	85
Table 31: Rainbow B4 Blisk ADP Operating Condition Compared to Baseline Blisk	85
Table 32: Reprocessed Purge Mass Flow Impact	88
Table 33: Tip Purge Pressure Tap Measurement for All Nominal Builds	
Table 34: Hub FWD Purge Pressure Tap Measurement for All Nominal Builds	90
Table 35: Hub AFT Purge Pressure Tap Measurement for All Nominal Builds	
Table 36: Low Solidity to Baseline 1D ΔCp _T	92
Table 37: Low Solidity to Baseline 1D ΔCp_T and Cp_T -Based $\Delta \eta_{TT}$	
Table 38: Tip Feature Compared to Baseline 1D ΔCp_T and Cp_T -Based $\Delta \eta_{TT}$	
Table 39: S2N Annular Test Traverse Program	
Table 40: Flow Function Results	
Table 41: Delta Loss for Solidity Changes	
Table 42: Delta Losses for Cooling Changes from Nominal Cooling	
Table 43: S2N Exit Gas Angles	
Table 44: Aerodynamic Performance Assessment of Each Technology Against TPMs	

List of Acronyms

Acronym	Definition	
5HP	5-Hole Probe	
ADP	Aero Design Point	
ALF	Aft Looking Forward	
ARMD	Aeronautics Research Mission Directorate	
BOS	Background Oriented Schlieren	
BTU	British Thermal Unit	
CAP	Capacitance Clearance Probe	
CFD	Computational Fluid Dynamic	
CMC	Ceramic Matrix Composite	
DAQ	Data Acquisition System	
DOE	Design of Experiments	
EIS	Entry into Service	
EWC	Endwall Contouring	
FEM	Finite Element Model	
FF	Flow Function	
FRAP	Fast-Response Aerodynamic Probe	
GEA	GE Aerospace	
HPT	High Pressure Turbine	
HyTEC	Hybrid Thermally Efficient Core	
IOI	Items of Interest	
KPPs	Key Performance Parameters	
Lbf	Pound force	
LE	Leading Edge	
LEAP	Leading Edge Aviation Propulsion	
MCO	Mechanical Check Out	
NASA	National Aeronautics and Space Administration	
NDTL	Notre Dame Turbomachinery Laboratory	
OGV	Outlet Guide Vane	
PLC	Programmable Logic Controller	
Pps	Pounds per Second	
PR	Pressure Ratio	
PSP	Pressure Sensitive Paint	
PT	Total Pressure	
PTR	Relative Total Pressure	
RANS	Reynolds Averaged Navier-Stokes	
Re	Reynolds Number	
RPM	Rotations Per Minute	
RTV	Room-Temperature Vulcanizing	
S1B	Stage 1 Blade	

S2N	Stage 2 Nozzle
SFC	Specific Fuel Consumption
SLA	Stereolithography
SoA	State of the Art
SS	Suction Side
TCL	Tip Clearance
TE	Trail Edge
TI	Turbulence Intensity
TP	Thrust Piston
TPM	Technical Performance Measure
TRL	Technology Readiness Level
TRT	Transonic Research Turbine
VFD	Variable Frequency Drive

Executive Summary

The objective of the Hybrid Thermally Efficient Core (HyTEC) – Advanced High Pressure Turbine (HPT) Aerodynamics project is to develop technology for a compact core that contributes to significant fuel burn reductions of 5-10% over current generation technologies. To accomplish this, the HPT is incorporating a range of aerodynamic features and technologies to improve component efficiency and provide favorable systems level trades. In particular, this project explored low solidity airfoils, advanced tip treatments, platform contouring, and advanced ceramic matrix composite (CMC) Stage 2 Nozzle (S2N) airfoils to eliminate the need for post throat cooling in a compact core environment. The maturation of these technology areas is expected to provide a significant improvement in component efficiencies, and consequently reductions in fuel burn, over the current state of the art (SoA).

To mature these technologies to Technology Readiness Level (TRL) 4, a test campaign was performed that consisted of four tests at three facilities. TRL 3 testing was performed in the CW22 linear cascade at NASA Glenn for blade and nozzle technologies, TRL 4 nozzle testing was performed at GE Aerospace (GEA) Test Cell A8, and TRL 4 blade testing was performed at the Notre Dame Turbomachinery Laboratory (NDTL) using the Transonic Research Turbine (TRT) rig.

Low solidity was successfully demonstrated to a TRL 4 level. Low solidity nozzles showed benefits in line with pre-project expectations, while low solidity blades were shown to have an aerodynamic penalty. Crucially, this program only considered the aerodynamic losses, and systems trades such as reductions in cooling flows are expected to continue to make low solidity blades a net positive. By successfully quantifying the aerodynamic performance in this project, these trades can be conducted to determine where in the engine architecture low solidity blades will contribute positively to system operation.

Platform contouring was demonstrated to a TRL 4 level, with performance in line with the lower end of the pre-project expected range. Advanced tip treatments performance levels were indeterminate, showing the expected improvements to flow physics but with a performance level confounded by several rig issues including whirl mode induced variation in tip clearance.

The elimination of post-throat cooling on the S2N was successfully demonstrated to provide a performance benefit, however that benefit was approximately half the level that was expected in pre-project predictions.

Overall, the technology maturation plan for HyTEC Phase 1 was successful, bringing the suite of technologies to TRL 4.

1. Introduction

The NASA Aeronautics Research Mission Directorate (ARMD) is currently operating an integrated subsonic transport technology maturation program, the Advanced Air Vehicles Program. A part of this program is the HyTEC project, which focuses on accelerating technology development for compact core technologies, with the objective of meeting the Key Performance Parameters (KPPs) shown in Table 1. As a part of this effort, GEA is under contract to mature HPT aerodynamic technologies for the next generation of narrowbody transport engines.

Table 1: HyTEC Project KPPs

КРР#	КРР	Full Success Single Aisle ~2035 Entry Into Service (EIS)	Minimum Success Single Aisle ~2035 EIS
KPP-1	Fuel burn reduction attributed to the high power density core of the original equipment manufacturer's vision turbofan engine	10%	5%
KPP-2	Engine Bypass Ratio	>15	>12
KPP-3	Engine Overall Pressure Ratio (defined at top of climb)	>50	>45
KPP-4	KPP-4 Durability, measured in operating hours between major refurbishments		Meet SOA of baseline
KPP-5	Degree of hybridization measured by level of power extraction from the turbofan engine at altitude	20%	10%
KPP-6	High Pressure Compressor Exit Corrected Flow	< 3 lbm/s	<3.5 lbm/s

For the HPT specific technologies, the relevant KPP for this contract is KPP-1, though in a future vision system, some of the benefits of the technologies may enable improvements to KPP-4 (durability) at the expense of performance. These trades are outside the scope of the present work.

2. Technology Background

Four technology areas were developed under the present work, focusing on both turbine vanes and blades. The key technology areas are briefly described in the following sections. The overall potential benefits of these technologies were defined as Technical Performance Measures (TPMs) for the subject work and are summarized in Table 2.

ltem	HPT Predicted Fuel Burn Improvement	Analysis & Test Measurement
Advance Tip Treatment	0.10 to 0.24	Relative total pressure loss
Integrated Rim Seals & Endwall Contouring (EWC)	0.00 to 0.05	Relative total pressure loss
Low Solidity Optimized Airfoil	0.10 to 0.23	Absolute or relative total pressure loss
Compact Core Stage 2 Nozzle	0.20 to 0.30	Absolute total pressure loss

Table 2: HPT Aerodynamics TPMs

2.1 High Lift/Low Solidity Airfoils

Reduced solidity relative to SoA airfoils have the potential to reduce aerodynamic losses due to reduced trailing edge blockage and profile loss, though the potential for increased secondary losses must be mitigated. The current work focused on leveraging advanced design and analysis tools to develop and validate innovative low solidity geometries for increased aerodynamic performance. Additional weight and coolant benefits are expected to be realized as well, though these effects are outside the scope of the current work.

Low solidity maturation under this program was conducted in two phases. TRL 3 level work was performed in the CW-22 linear cascade facility at NASA Glenn Research Center. Linear cascade work was performed on a S2N to validate the optimal solidity reduction to target for future TRL 4 level work.

Additionally, linear cascade work was performed for stage 1 blade (S1B) concepts to understand incidence effects for low solidity airfoils that were not able to be adequately tested in a TRL 4 level environment.

In addition to the TRL 3 level testing, higher fidelity testing was performed to advance low solidity concepts to TRL 4. For nozzle technologies, a full annular cascade was run at the GEA Evendale A8 facility to capture data on both flow function and airfoil losses. For blade technologies, a low solidity set of airfoils was run in a single stage rotating rig at the TRT facility at the NDTL.

2.2 Advanced Blade Tips

Advanced blade tip technology was at TRL3 prior to the subject work; proof-of-concept demonstrations had been completed by GEA in rotating rigs and engines. To integrate the technology with a compact core design and verify performance, advanced tip technology was included as part of a rainbow wheel on NDTL TRT rig. This approach provided a direct measurement of back-to-back performance relative to current SoA design, with the goal of advancing the technology to TRL4.

2.3 Endwall Contouring

In addition to improving turbine efficiency by reducing secondary flow loss near the platform and the root, non-axisymmetric EWC is used to control flow purged from the forward and aft cavities and is designed specific to the angel wing configuration. EWC has been used in various GEA products, and at the start of

the subject work, was consistent with TRL3 for compact core application. To advance to TRL4, a back-to-back assessment with and without a mechanically balanced EWC design was conducted in the NDTL TRT rig.

2.4 Aerothermal Ceramic Matrix Composite Stage 2 Nozzle

Improved aero design technology is required for high thickness and low solidity nozzle concepts to support compact core architectures. At the start of the subject work, ceramic matrix composite (CMC) S2N design was at TRL2, due to compact core design requirements. A stepwise approach was executed to advance the aero design to TRL4. The impact of various high thickness-to-chord nozzle designs was investigated in the NASA CW-22 linear cascade. Following this work, linear cascade testing was conducted to understand the aerodynamic impacts of post-throat cooling to conduct compact core architecture trades. Following completion of this testing, these results were leveraged to design a full 3D nozzle which was tested in GEA's Cell A8 annular cascade to validate the aero design to TRL4.

3. Aerodynamic Design

The aerodynamic design of each test article is discussed in this section. Baseline test articles were either used directly from existing designs or adapted to rig requirements as discussed in each section. New designs tested under this effort were designed using GEA standard processes and best practices.

3.1 CW22 Stage 2 Nozzle

Three solidity designs were planned for the first part of testing for solidity (Figure 1): baseline, reduced solidity with short chord (denoted medium solidity), and low solidity with increased pitch spacing.

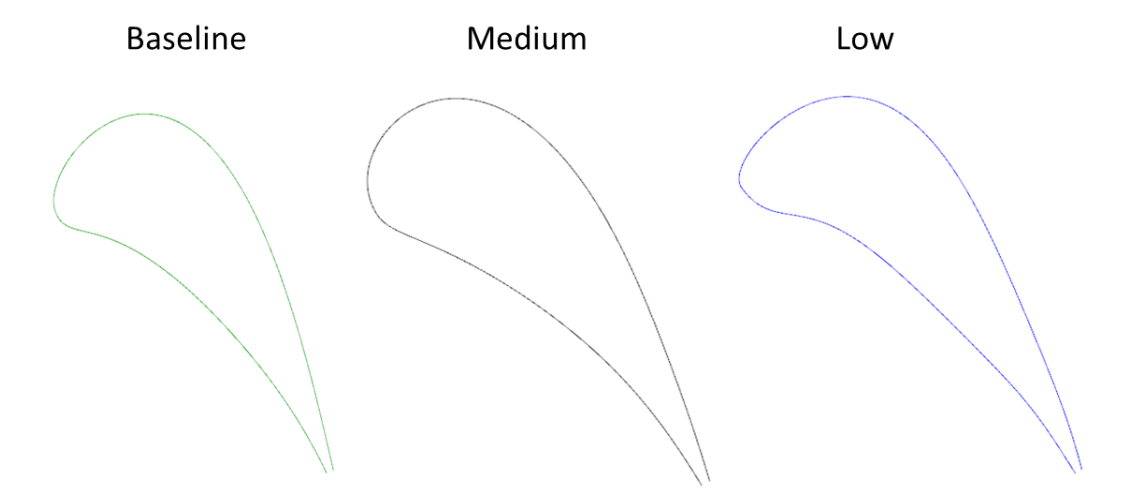


Figure 1: View of Three Solidity Configurations

The test articles were designed to achieve specific levels of loading, defined by the incompressible Zweifel coefficient, given by:

$$Zw_{inc} = 2\cos^2\alpha_2 * \frac{S}{C_z}(\tan\alpha_1 + \tan\alpha_2)$$

where α designates airflow angles (inlet and exit for subscripts 1 and 2 respectively), S is the pitch, and C_z is the axial chord. The baseline airfoil Zweifel loading was set based on traditional GEA airfoil count and the vision product axial length, which resulted in lower Zweifel loading than the current SoA. The medium solidity airfoil was designed to achieve the current SoA loading for metal blades by maintaining count and shortening axial chord while meeting design constraints for CMCs. The low solidity airfoil was designed to a Zweifel above the current SoA, while meeting the same design constraints as the medium solidity airfoil. To do this, axial chord was held constant to the baseline, and airfoil count was reduced.

The solidity test articles were created with a uniform profile across the span to capture only differences in profile loss between the three solidities. Secondary flows were out of scope for the linear cascade testing. The trailing edge thickness was consistent between the three solidity nozzles. The baseline solidity configuration was a midspan section of an HPT nozzle representative of engine hardware. Low and medium solidity configurations were both designed to the same design point as the baseline.

All airfoil sections were designed using GEA best practices. The primary difference in loading characteristics was increasing degrees of suction side forward loading as Zweifel increased. The baseline and medium solidity retained a traditional suction side loading with acceleration over most of the airfoil.

However, the low solidity loading necessitated a forward peak isentropic Mach number and diffusion over most of the suction side. Airfoil loadings are shown, compared to test data, in Section 5.1.4.

For cooling design, an open literature 7-7-7 hole form was selected. Three film rows were defined for study to bound the area of the airfoil where post-throat cooling flows might be introduced, with the intent of having the ability to study the effects on losses over a range of injection locations and loading profiles as solidity varied.

3.2 CW22 Stage 1 Blade

The tested profiles for this test campaign had been previously designed for solidity reduction analyses in advance of the HyTEC project. The airfoils chosen for the test included a baseline count based on a type design commercial HPT pitchline airfoil to serve as a baseline, a medium solidity airfoil which consisted of the pitchline profile for the airfoil tested in the TRT rig low solidity blisk, and a low solidity airfoil to explore the limits of reducing solidity. Solidity is defined as:

$$s = \frac{Axial\ Width}{Pitch}$$

A GEA proprietary Reynolds averaging Navier-Stokes (RANS) Computational Fluid Dynamics (CFD) code was used to predict test results. This data was used as a benchmark to judge the cascade's performance to expectations, and deviations were investigated further to understand the underlying physics. Three different meshes for the three different S1B geometries were created to assess airfoil loadings, aerodynamic losses, and leading-edge flow stagnation data. The RANS CFD was run with a k-omega turbulence model, and the turbulence values from past NASA characterization of the linear cascade were utilized [1]. See details in Section 5.2 for comparison to test results.

3.3 Transonic Research Turbine

3.3.1 Aero Design Overview

The transonic research turbine (TRT) rig is a single stage design with a nozzle and blade. The flowpath and baseline airfoils were initially designed for a current State of the Art (SoA) commercial high-pressure turbine (HPT). The baseline airfoils did not require any additional design work. There are four advanced, aero technologies designed as unique blades for the TRT rig: a low solidity blade, a blade with a tip flare, a blade with a tip winglet, and a blade with hub platform contouring. The low solidity technology consists of a reduced blade count as well as a unique airfoil design to minimize aerodynamic losses. Due to the count and airfoil changes required, this design was incorporated onto a full wheel blisk. The other three technologies are applied to a baseline airfoil as performance enhancement features to minimize secondary losses. These three features were included into quadrants on rainbow wheel blisks. For the advanced tip features, the benefit comes from the reduction and re-location of the tip vortex off the airfoil surface. For the hub platform contouring feature, the benefit comes from reducing the cross-passage pressure gradient and reducing the strength of the hub secondary flow vortices. Below is a brief summary of the aerodynamics tools and methods used to design the advanced features, followed by a detailed description of each of the designs.

3.3.2 Design Procedure

Airfoil design followed GEA best practices. Each design was assessed to determine whether the difference from baseline could be measured based on a pressure loss-based efficiency measurement from the fast

response aero probe (FRAP) that is phase locked to the rotor placed in the downstream area traverse. The test measurement and instrumentation will be discussed in more detail in Section 5.3, but a short summary of both criteria will be presented here.

The TRT rig configuration was initially designed and first tested in 2011 and ran over a two-year period with over 30 builds. Monte Carlo assessment and past rig operation has demonstrated uncertainty of the rig absolute stage efficiency measurement to be within $\pm 0.35\%$. There were some lessons learned after the first set of testing, and after implementation of key changes, the rig repeatability was measured to be $\pm 0.12\%$ delta stage efficiency in 2013. The rig measured repeatability was set to be the target delta efficiency measurement minimum threshold since the back-to-back deltas were being compared in this test. A Monte Carlo based uncertainty assessment was completed on the FRAP probe to determine an absolute measurement capability of $\pm 0.10\%$ PTR on a 2σ basis. This set the measurement criterion for a measurable PTR difference in the rig. The four different blisk builds are shown below in Figure 2.

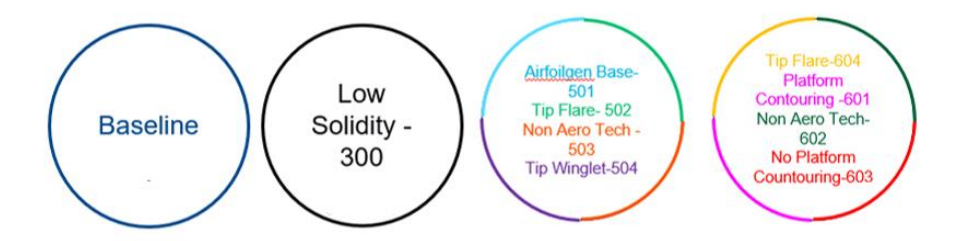


Figure 2: Blisk Configurations

The baseline and the low solidity designs are full wheel blisks, therefore torque based and FRAP based efficiency measurements are possible. However, for the two rainbow rotor blisks containing the advanced tips and the hub platform contouring, only FRAP efficiency can be used. The full wheel blisks will be used to create a transfer function that can be applied to the rainbow rotors to convert the pressure-loss based measurement to a torque-based efficiency measurement.

3.3.3 Baseline Design

The baseline blade airfoil design was completed in 2012 for a SoA HPT design. The design establishes a performance baseline that all the following turbine technologies are compared against. The flowpath and airfoils were initially designed at engine conditions before being converted to the rig design. In 2012, a 1D model had been created and used to set the rig conditions to match the engine rotor exit Mach number, Vz/U, and maintain the engine to rig scale at 1:1. As a result, the rig Reynolds number is lower than an engine condition Reynolds number. Table 3 below shows ratio rig conditions normalized by the engine conditions.

	TRT 1D model Normalized to Engine Conditions	
Relative Tip Mach Number	1.00	
Vz/U	1.01	
Reynolds Number	0.39	

Table 3: Engine vs. TRT Rig Conditions

The 1-D model contains the aerodynamic operating conditions, stage count, flowpath geometry, design speed, worksplit, airfoil counts, and evaluates the overall turbine rig performance. After completing the 1D model, the 3D geometry was designed. Figure 3 below shows the rig flowpath cross section containing a set of vane and blades.

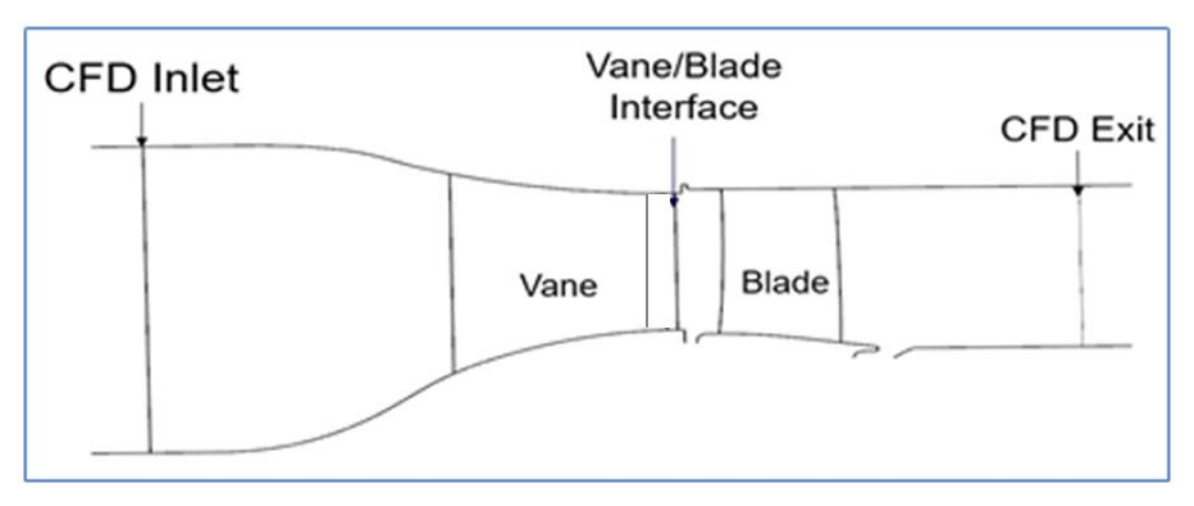


Figure 3: Rig Flowpath Cross-section

Due to the rig design and facility limitations, both the vane and the blade are solid metal designs with no internal cooling. The vane 3D geometry is shown in Figure 4.

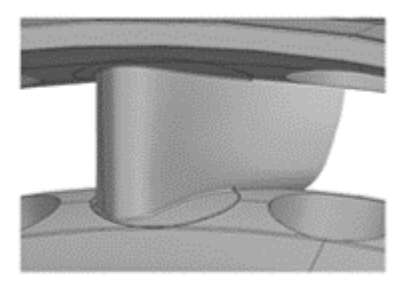


Figure 4: Stage 1 Vane 3D Design

The nozzle is assembled using a method leveraged from a compressor vane assembly and results in is a button feature on the hub and case that can be seen in Figure 4. As a result, there is a small gap between the nozzle and the bands over the last \sim 50% of the airfoil chord. The blade 3D geometry is shown in Figure 5.



Figure 5: Stage 1 Blade 3D Design

The blade 3D image in Figure 5 is a single blade out of a full blisk. The platform contouring has no circumferential gaps between airfoils since the hub surface is a single machined surface. Airfoil tip features must be designed for a single cutting tool to fit in between airfoils. The blisk includes two unique

mechanical features: a balance rim to allow for blisk balancing at the manufacturing vendor and a trilobe interface for assembly onto the shaft.

For the current rig test, the existing baseline 3D geometry was meshed and evaluated in a multi-row, CFD solution to ensure consistency with the mesh and solution of the new technology designs. Figure 3 shows the CFD domain for each airfoil. The vane inlet was extended forward of the vane leading edge. The vane-blade interface was set to provide a sufficient number of mesh cells in front of the forward blade cavity. The blade exit domain was extended aft of the blade trailing edge to encompass both the exit traverse and exit rake instrumentation in the rig. Both the hub and aft cavities were modeled in the blade domain with purge flow applied at the bottom of each cavity. All boundary conditions applied were based on previous test experience. A consistent domain and set of boundary conditions were used for all the blade technology designs to evaluate both torqued based stage performance and relative pressure loss across the blade. No baseline results are shown in this section, but instead will be a reference to show delta performance for each of the advanced technologies.

3.3.4 Low Solidity Design

The low solidity design followed the design process outlined above (section 3.1) and was designed at TRT rig conditions. The 1D model was updated for the reduced blade count to provide a reference against the CFD results. The 1D tool does not have sufficient capability to capture the impacts of the change in the unique 2D airfoil design profile or the full 3D airfoil. The airfoil shapes were optimized to maximize torque-based efficiency for the reduced blade count design using a machine learning based optimizer built on top of a parametric airfoil design tool. All design iterations were evaluated using the CFD methodology outlined in the baseline design section. Figure 6 below shows the final 3D airfoil.



Figure 6: Low Solidity Stage 1 Blade 3D Design

Some important distinctions between the baseline airfoil design and the low solidity airfoil design are the larger hub fillet for the low solidity blade and modifications to the 2D sections designs. Both were iterated to minimize performance loss while meeting aeromechanics design margin requirements. The highest performing designs for the low solidity blade all had high airfoil stagger and were forward loaded. The 2D airfoil design for low solidity increases the curvature around the leading edge and high curvature region of the airfoil. The increased forward curvature loads the airfoil as shown in Figure 7 with a longer region of post throat diffusion than the baseline airfoil.

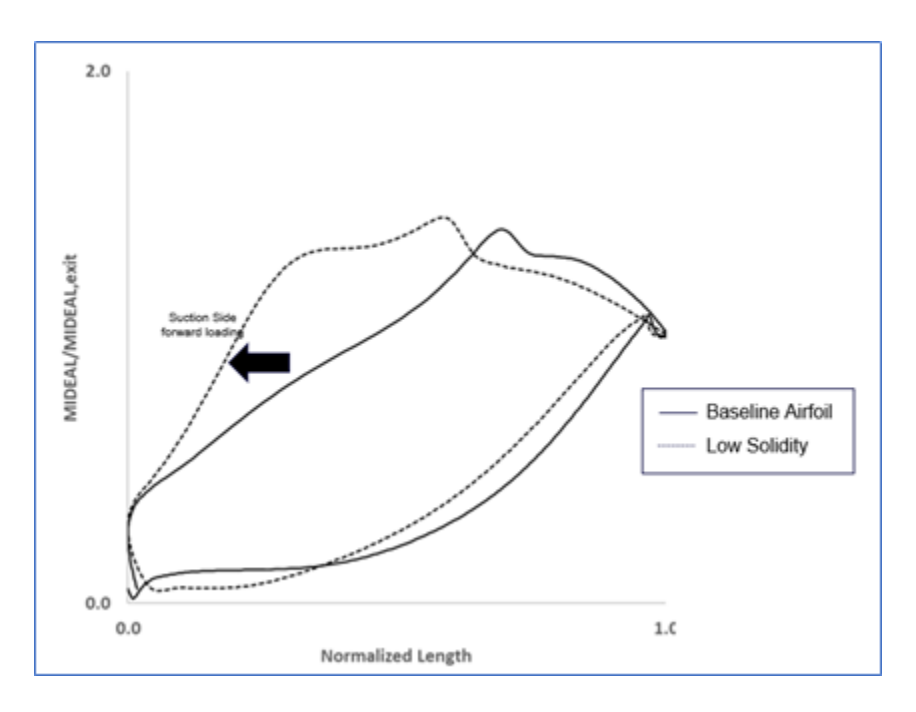


Figure 7: Pitchline Baseline vs. Low Solidity Loading (50% span)

The forward loading must be spread out over the front of the airfoil to avoid a significant Mach number spike forward of the throat. There is a large region of low Mach number fluid on the pressure side surface near the leading edge as a result of the design. A throat adjustment was required to match flow function and re-adjust the airfoil turning utilizing CFD.

The low solidity design is a full wheel blisk configuration. Therefore, the design success criteria is both stage torque based efficiency and blade relative total pressure based efficiency. Table 4 shows the pre-test performance delta for stage efficiency, flow function, and the max delta of the relative total pressure (PTR) profile relative to the baseline airfoil from the CFD.

Table 4: Low Solidity Pre-Test Performance Delta

Description	Δ% Stage Efficiency	%Difference Flow Function	Max ΔPTR (absolute pounds per square inch (psia))
Base	-	-	-
Low Solidity	-0.04%	-0.07%	-0.45/+0.65

The flow function deviation was reduced using CFD as guidance for throat setting. The airfoil throat was reset via a small adjustment to the airfoil shape until the flow function was within $\pm 0.1\%$. This process was used on all the airfoils with technologies. The stage efficiency delta of -0.04% will not be a measurable delta in the rig since the rig uncertainty is $\pm 0.13\%$. However, the difference in the relative total pressure should be measurable by the FRAP probe in the downstream traverse as indicated by Figure 8b. Figure 8 below shows the exit relative pressure 2D contour and average radial profile at the exit traverse location of the rig as a delta to the baseline design.

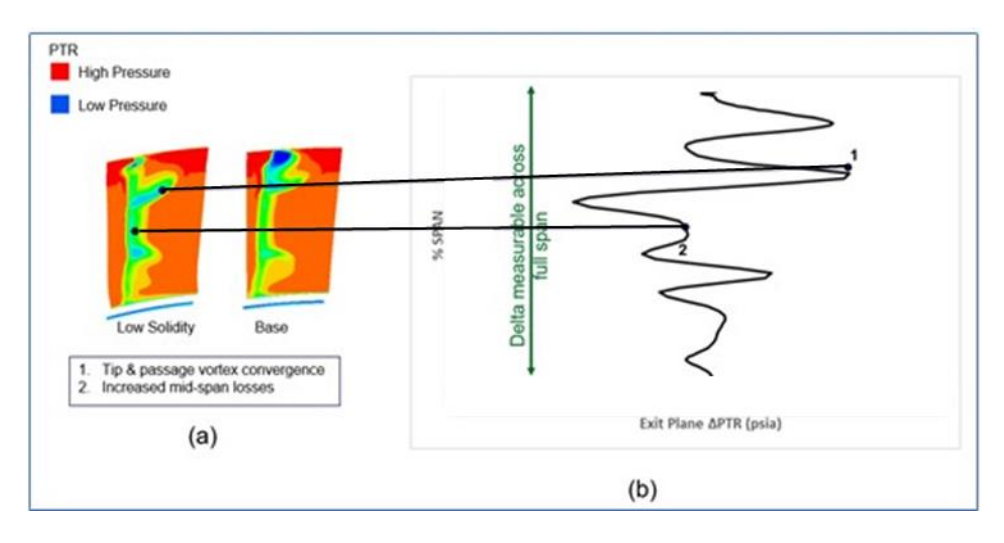


Figure 8: Pre-Test Predictions of Low Solidity to Baseline
(a) 2D Exit PTR Contours (psia); (b) 2D Exit PTR Profile Delta to Baseline (psia)

The low solidity design has a smaller tip vortex in the 80%-100% span region. This is due to a portion of the tip vortex and passage vortex converging creating a larger loss in the 70% span range identified as item #1 of Figure 8. The radial extent of the mid-span region of predominantly axial flow is reduced for the low solidity design, with the hub, secondary loss vortex moving up the span to consume greater than 40% of the airfoil span.

3.3.5 Advanced Tips - Flare & Winglet Design

In an unshrouded blade, the pressure difference between the suction side and pressure side of the blade drives leakage flow over the tip. The flow that leaks over the tip as unworked fluid feeds the tip vortex driving additional aero losses. The tip vortex component of the blade loss is a large contributor to the overall blade losses and reducing this source of loss can yield significant overall turbine performance improvements. The purpose of an advanced tip feature is to decrease losses over and around the tip by manipulating the leakages, tip vortex, and case cross passage vortex. Both a flare and a winglet are shown to improve performance by reducing the tip vortex losses.

The flare and winglet designs are isolated to the baseline blade tip region only. The flare design is shown in the upper right quadrant of the rainbow blisk (green) in Figure 9. The winglet design is shown in the bottom left quadrant of the rainbow blisk (purple).

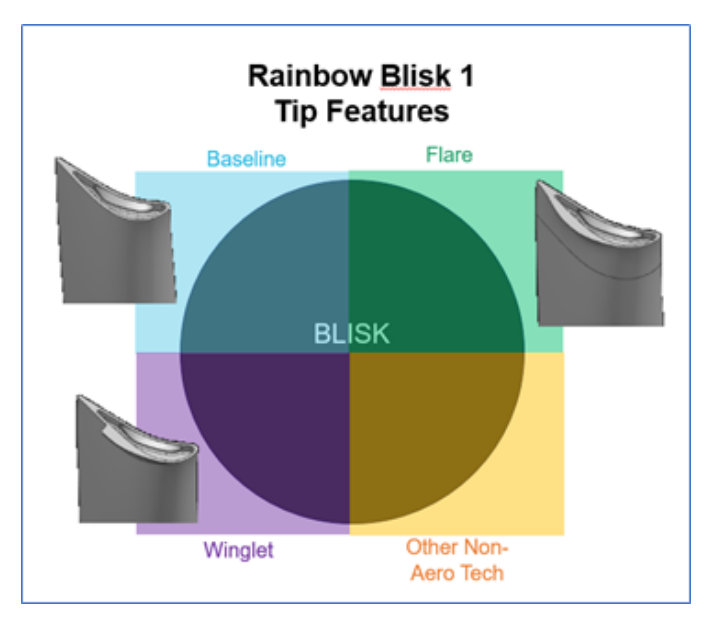


Figure 9: Rainbow with Tip Features –
Tip Flare Upper Right Quadrant (green) & Tip Winglet Lower Left Quadrant (purple)

The flare tip feature was initially optimized using CFD at engine conditions for the baseline airfoil as part of a SoA HPT system. A trade between added weight and aero performance was completed to down select to the final shape. Once optimized, it was applied to the baseline airfoil in the rig conditions and evaluated at the rig conditions using the CFD method above to determine if deltas would be detectable. The winglet was then designed to have a similar tangential offset thickness at the tip as the flare. The radial height of the winglet was determined based on the manufacturing thickness capability.

The intent of the design was to prove a winglet would provide the same performance improvement as a flare if both were of equal size. The pre-test results from the CFD at rig conditions in Table 5 shows that to be true for both stage efficiency deltas and relative pressure loss deltas.

Table 5: Advanced Tip Pre-Test Performance Deltas

Description	Δ% Stage Efficiency	%Difference Flow Function
Base	-	-
Tip Winglet	+0.3%	+0.0%
Tip Flare	+0.3%	+0.1%

Adding tip features impacts the throat plane and the airfoil throat was re-set via a small airfoil shape adjustment to match the baseline configuration to within $\pm 0.05\%$ flow function. Both advance tip technologies are only on a rainbow blisk, therefore the only measurement to validate their performance will be with the FRAP system. Figure 10 below shows the exit relative pressure 2D contour and average radial profile at the exit traverse location of the rig of the rig as a delta to the baseline design.

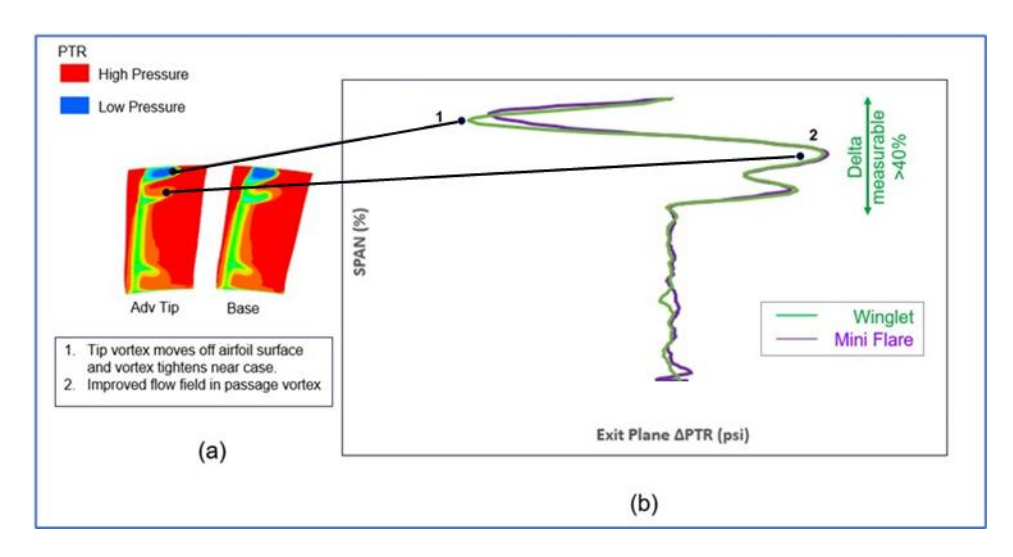


Figure 10: Pre-Test Predictions of Advanced Tip
(a) 2D Exit PTR Contours (psia) (b) 2D Exit PTR Profile Delta to Baseline

Figure 10a shows the reduced tip vortex and the reduced passage vortex denoted as items #1 and #2 respectively. The impact on the relative pressure contour when compared to the baseline is shown in Figure 10b. For both the tip winglet and tip flare, the impact on the upper 40% of PTR should be measurable by the FRAP traverse relative to the baseline design. However, the difference between the winglet (green) and flare (purple) feature are indistinguishable.

3.3.6 Hub Platform Contouring Design

Hub platform contouring is a technology targeting reduction in hub secondary losses which includes the endwall crossflow, counter vortex, and passage vortex. Figure 11a below shows the mechanisms of secondary loss in the hub and Figure 11b shows the reduction in the passage and counter vortex strength.

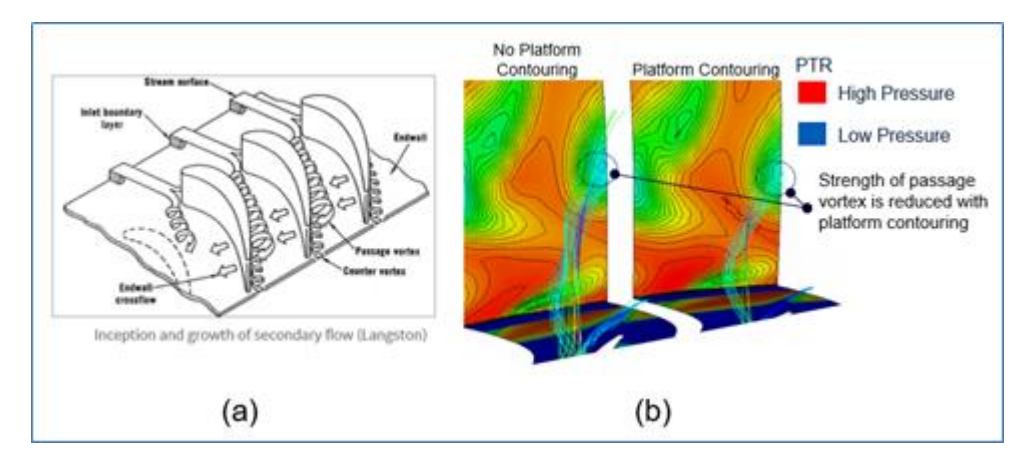


Figure 11: Platform Contouring Flow Physics: (a) Mechanisms of Secondary Loss (Langston [2])

(b) Impact on Secondary Loss Core due to Platform Contouring

Platform contouring already existed on the rig baseline blisk. To obtain a back-to-back delta PTR plot, the platform contouring was removed for one quadrant of a rainbow blisk. This allowed for a comparison of the platform contouring impact on the downstream relative pressure field to be measured by the FRAP exit traverse. Figure 12 below shows the rainbow blisk quadrants with and without platform contouring.

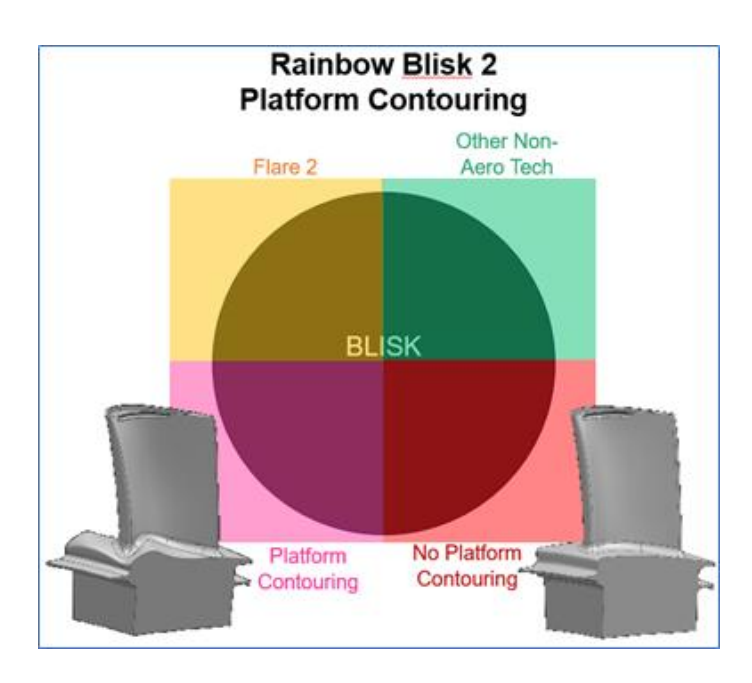


Figure 12: Rainbow with and without Platform Contouring – Base Airfoil with Platform Contouring Lower Left Quadrant (pink) & Base Airfoil without Platform Contouring Lower Right Quadrant (red)

The CFD analysis used to determine the pre-test performance delta expected from platform contouring in TRT is described above and the results are provided in Table 6.

Table 6: Hub Platform Contouring Pre-Test Performance Delta for Both Design Success Criteria

Description	Δ% Stage Efficiency	%Difference Flow Function
No Platform Contouring	-	-
Platform Contouring	+0.2%	+0.1

Removing the hub contouring impacts the throat plane and the airfoil throat was re-set via a small airfoil shape adjustment to match the configuration with hub contouring to within $\pm 0.1\%$ in flow function. The pre-test performance benefit of the platform contouring is +0.2% in stage efficiency if it were to be a full wheel comparison in the rig test. However, this design being a rainbow rotor, the performance assessment must be made with a rotor phase locked FRAP probe in the exit area. The variation in relative exit pressure is shown below in Figure 13.

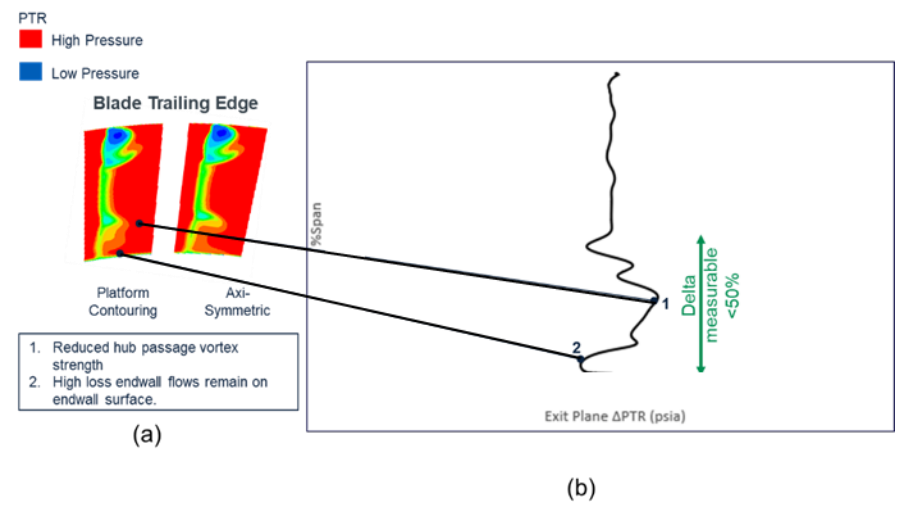


Figure 13: Pre-Test Predictions of Platform Contouring
(a) 2D Exit PTR Contours (psia) (b) 2D Exit PTR Profile Delta to Baseline (psia)

The 2D exit contours of PTR in Figure 13a show the expected improvement in the secondary flow field with a reduced passage vortex strength in the <50% span region. The delta in the PTR radial profile is shown in Figure 13. There is variation in the hub relative pressures below 50% span, however they are nearly un-detectable changes. It may be difficult to discern a benefit from the FRAP probe alone for this rainbow quadrant assessment.

3.4 Stage 2 Nozzle Annular

Two test articles were identified for annular testing following linear cascade testing. The baseline test article consisted of the Stage 2 Nozzle (S2N) aerodynamic shape of GEA's current type certification SoA engine. As this airfoil contour is an existing design in current service, the aerodynamic design of this airfoil is out of the scope of this report and will not be discussed in detail.

The reduced solidity test article was designed with the same axial length as the baseline SoA. The reduced solidity airfoil was designed at engine conditions for the SOA baseline to provide a direct comparison to the baseline. The reduced solidity airfoil was designed to closely match flow function of the baseline case using CFD analysis.

The design process for the 3D airfoil leveraged the low solidity airfoil design of the linear cascade during preliminary design. In detailed design, a multi-parameter optimization process was conducted, exploring variations in radial vortexing, circumferential and axial stacking of design sections, and profile changes on each design section. As a result of this optimization for the 3D flow field, the design sections morphed from those tested in the linear cascade to better manage losses associated with the higher loading levels of this low solidity design. The midspan for the optimized airfoil is shown in Figure 14.

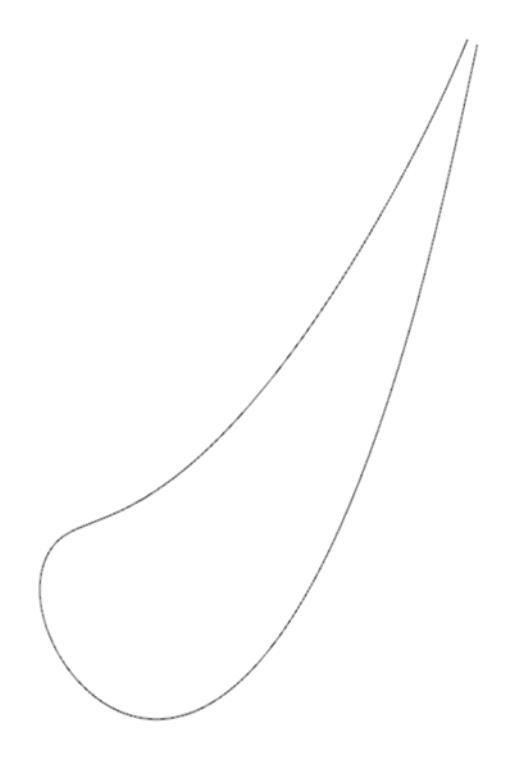


Figure 14: Airfoil Section of Annular Test Article

The optimized sections reduced stagger from the tested low solidity airfoil at the hub, reflecting locally reduced loadings that allow for a more aft-loaded airfoils. The mid-span section remains at nearly the same stagger as the low-solidity linear cascade airfoil, though the pressure and suction side is re-contoured due to the flow field distribution from the 3D aero. The tip section also was reduced in stagger slightly from the low solidity linear cascade design, and the suction and pressure sides recontoured to better mitigate secondary flow losses in the passage. Airfoil loadings at 50% spanwise locations are shown in Figure 15.

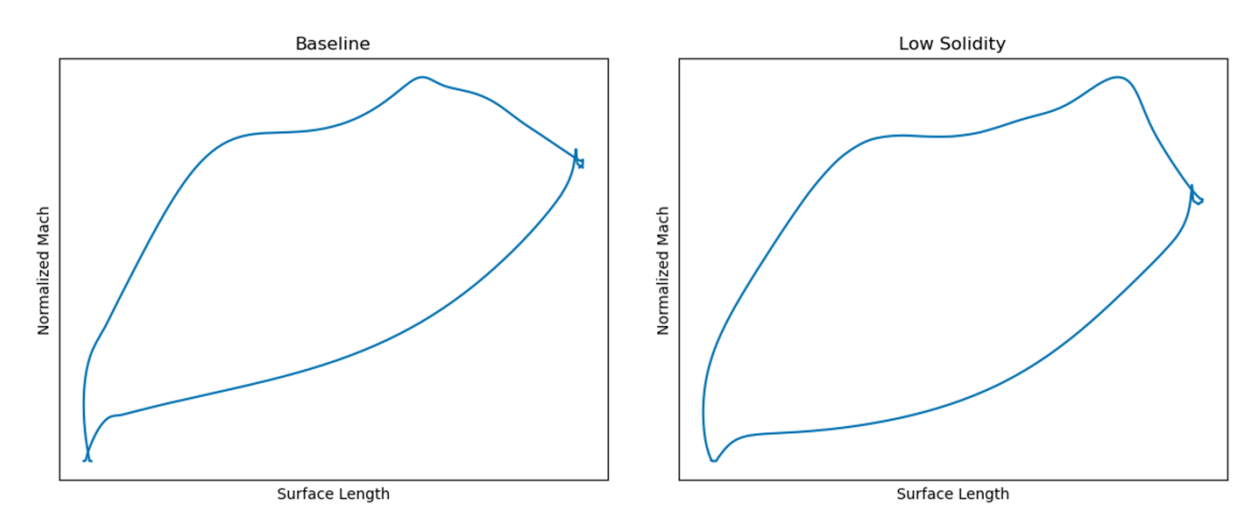


Figure 15: Annular S2N Loading Comparison, 50% Span

Downstream radial total pressure profiles are shown in Figure 16. The optimized low solidity airfoil sees higher losses than the baseline in the midspan region where the loading is increased, but the vortexing and stacking determined in the optimization process result in lower loss in the endwall regions, especially near the outer band.

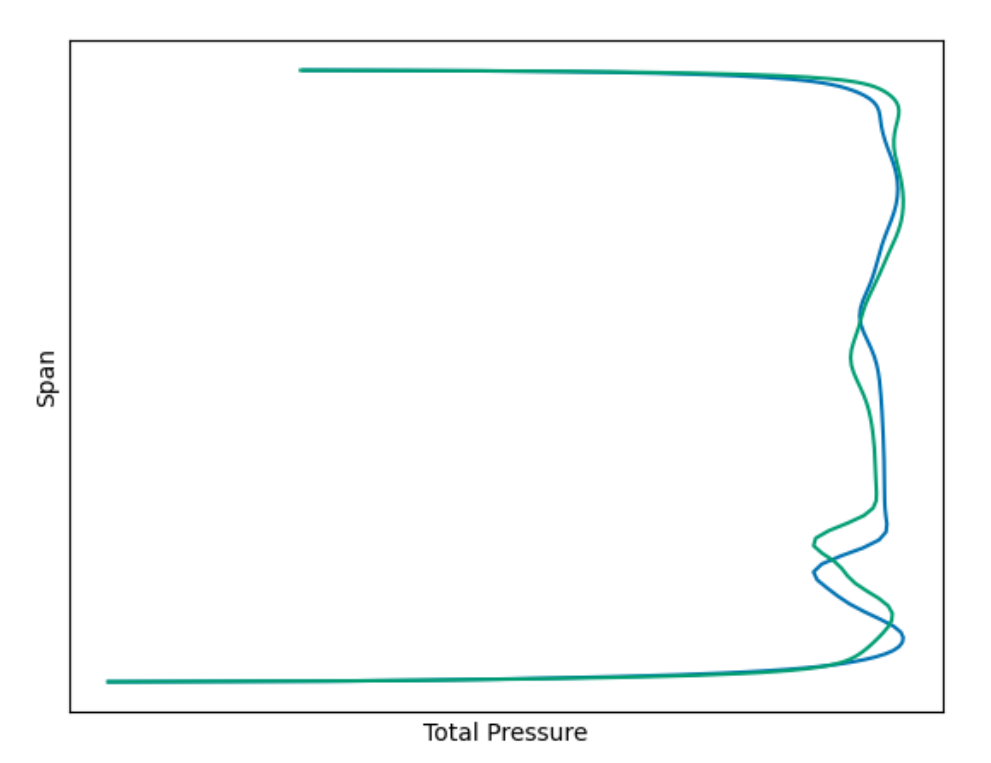


Figure 16: Downstream Radial Profile, Total Pressure

The relative performance predictions during the design process are shown in Table 7. Low solidity was expected to outperform baseline, however the difference in performance was expected to be within the uncertainty of the 5-Hole Probe (5HP) used in the test. The flow function was predicted to be down 0.2% for the low solidity design compared to the baseline as a result of the throat setting methodology, which was within design expectations.

Table 7: Design Deltas, Baseline vs Low Solidity

Delta		
Flow Function	-0.2%	
Cp _T (pts)	-0.1	

4. Test Program

The design of the test program for each rig and test article are discussed in this section. These test programs were developed in consultation with rig personnel at the various facilities and followed GEA best practices.

4.1 CW22 Stage 2 Nozzle

4.1.1 Objectives

The goal of the CW22 S2N linear cascade test was to advance proposed nozzle technologies from TRL2 to TRL3. A secondary goal of the linear cascade test was to drive design recommendations for the S2N annular cascade, which was conducted as a follow-on test in the HyTEC project. Overall, the goal of testing was to understand the performance impact of reduced solidity and the potential benefits of reducing or eliminating post-throat cooling for the elevated temperatures expected in compact core architectures. To meet this objective, two aspects of the linear cascade test were defined:

- a. Determine nozzle performance at a range of solidities, including performance derivatives of pressure ratio, Reynolds Number, incidence, and turbulence.
- b. Quantify performance impacts of post-throat cooling injection at various locations on low solidity airfoils.

The linear cascade test would be considered successful if performance derivatives were obtained and validated for solidity, pressure ratio, Reynolds Number, and coolant blowing ratio. Turbulence derivatives were a secondary objective. Additionally, the test would be successful if the optimal solidity for go-forward TRL4 testing with the S2N annular cascade were identified. The test successfully achieved all main objectives, though as discussed further below, only limited turbulence derivatives were obtained.

4.1.2 Test Facility

This study performed all testing and measurement acquisition in the NASA Glenn Transonic Turbine Blade Cascade (Figure 17). This large-scale facility has historically been utilized for aerodynamic and heat transfer studies of turbine blade geometries for propulsion applications. The facility features large ranges of possible airflow turning, adjustable incidence angles, and high transonic flow rates.

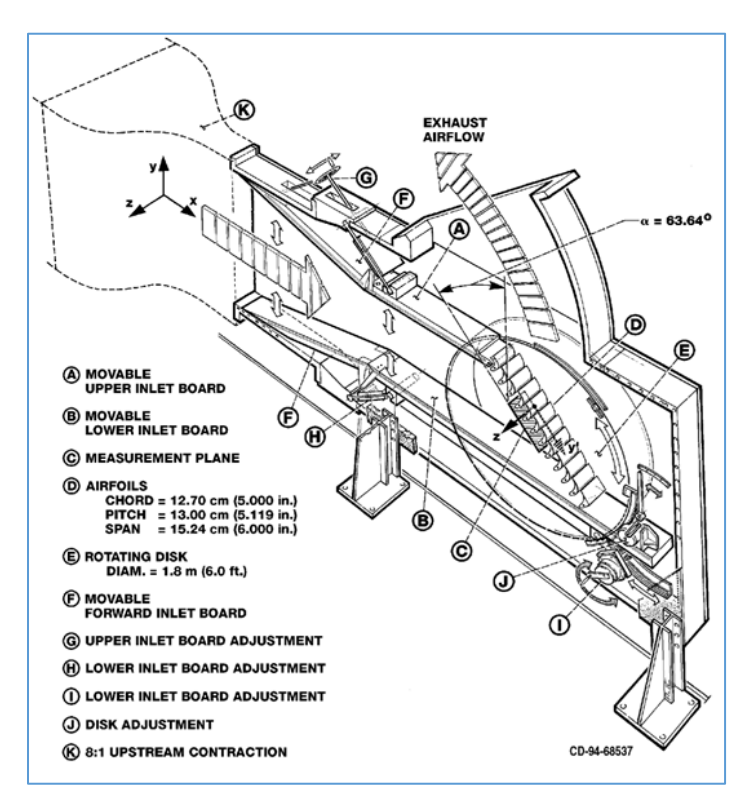


Figure 17: NASA Glenn Transonic Turbine Blade Cascade with Feature Callouts

Figure 18 shows how facility air travels from inlet to exhaust through the rig. Inlet air was supplied by a facility 40 psig (276 kPa) combustion air system, which entered the facility as clean, dry, ambient temperature air throttled at a maximum inlet pressure of 18.3 psia (126 kPa). Supply air flowed through an acoustically lined plenum chamber, which transitioned into a rectangular cross section. Next, flow conditioning and an 8:1 contraction section directed the flow into the cascade test section, and air discharged into an exhaust header of approximately 2 psia (14 kPa) minimum. A turbulence grid between the contraction section and test section provided desired turbulence levels for the test. The well-documented inlet boundary layer was nominally 1.0 inch (25.4 mm) [3]. Throttling valves between the test section and exhaust header allowed the Reynolds and Mach numbers of the rig air to be controlled and tuned independently. The ratio of total inlet pressure to exit static pressure determined the rig operating pressure ratio. Rig exit static pressure was tuned to adjust the overall rig pressure ratio during test. Inlet total pressure was tuned to adjust the overall rig pressure ratio during test.



Figure 18: NASA Glenn Transonic Turbine Blade Cascade

Cascade airfoils were mounted on a rotating disk, which could be set manually to a wide range of inlet flow angles by rotating the circular test section of the rig. Figure 19 shows a cross-section of the facility with the rotating circular test section for airfoils. The cascade fit 10 to 12 airfoils, which were installed between upper and lower inlet boards. The facility test section allowed for a fixed airfoil span of 6.0" (152.4mm) and fixed pitch of 5.119" (130.0 mm). The baseline and medium solidity configurations had the same pitch as provided by the facility. However, the low solidity configuration had an increased pitch which required facility adjustments (described in Section 4.1.2.3). Blade loading data (surface static pressure taps) and downstream probe survey data (five-hole traverse probe) were acquired for all points in the test matrix, for each test configuration. The probe survey data extended over three airfoil pitches (for the baseline and medium solidity airfoils, two for the low solidity) to verify periodicity downstream of the test section, and data was taken behind the test articles at the airfoil midspan location.

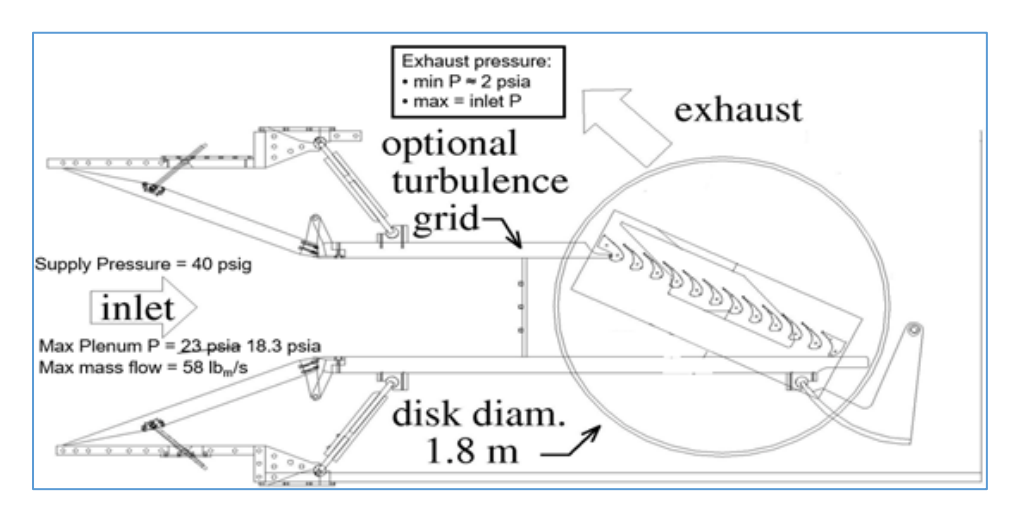


Figure 19: NASA Glenn Transonic Turbine Blade Cascade Cross Section

A carbon dioxide system was used to supply coolant flow for film cooling to the test articles to better match density ratios between main air and coolant to engine applications. The carbon dioxide was held in an external jacketed vacuum tank exterior to the test cell, fed into the facility through controlled valves into three separate carbon dioxide circuits. Mass flow rates of the carbon dioxide were measured using orifice plates in the carbon dioxide circuits. From the carbon dioxide circuits, the coolant flow was fed into a plenum internal to the test articles. Each of the three instrumented test articles were hooked to three independent carbon dioxide circuits outside the test section with connecting tubing for each test nozzle. Carbon dioxide from the plenum exited through cooling hole passages to the exterior surface of the nozzle during test operation. The ratio of coolant density to the main rig airflow was set to resemble engine conditions. During checkout, it was determined that only limited temperature control was possible due to the large thermal mass of the supply system and the low flow rates of carbon dioxide. To better control coolant temperature in future testing, it is recommended that a heat exchanger be installed immediately before the coolant enters the test article to control temperature nearer to the point of interest.

4.1.2.1 Instrumentation

A two-dimensional cross section of the measurement system set-up in the cascade is shown in Figure 20. A static pressure measurement system in the facility included 832 ±15 psid (103 kPa) ports with an atmospheric reference, and 543 of those taps were an array of endwall static pressure taps. A total of 87 endwall taps were located in each of the three test article center passages. The facility data acquisition system (DAQ) provided 120 additional analog channels to be used as needed. Inlet total pressure was measured with one to three Kiel probes located approximately one axial chord upstream from the test article leading edge plane. Target exit Mach number and Reynolds number were set with exit static pressure taps downstream of the airfoil trailing edge plane, and inlet static pressure was measured with five inlet static pressure taps upstream of the airfoils. Five traverse measurement planes were available: this test used an

upstream traverse to characterize the inlet (Station 00) and a downstream traverse to characterize the exit (Station 04).

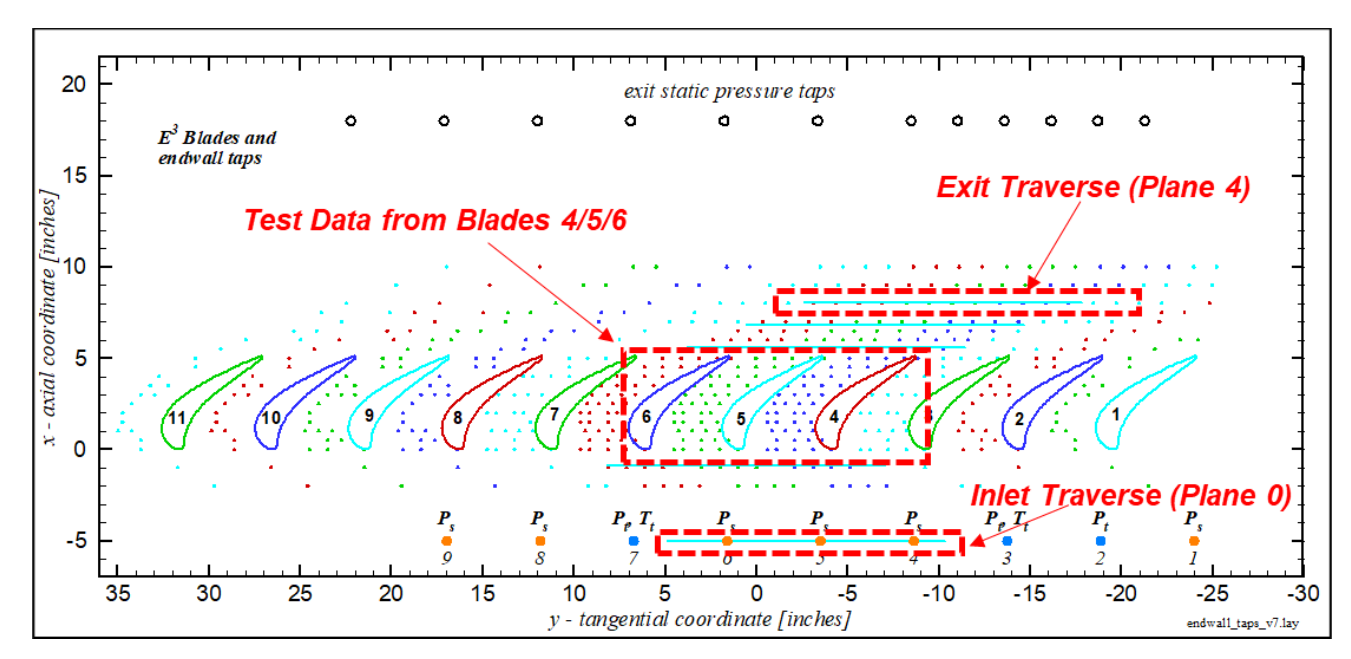


Figure 20: S2N Measurement Set-Up Cross Section

Static pressure measurements were taken on the surface of the test articles to produce airfoil loadings. The static taps were printed directly as part of the test article, with lead-out holes to one end of the airfoil. The static pressure instrumentation tubing was routed by the NASA instrumentation team from the airfoil into a bundle that fed through an opening in the rig endwall to the external transducer. The static pressure instrumentation on one of the nozzle configurations is shown in Figure 21 below. The three test articles had the same number of static taps on the surface, with static taps at the leading edge, trailing edge, along the pressure surface, along the suction surface, and in line with each cooling row. Static taps were included on all test articles to verify periodicity with the final airfoil loadings. An electronically scanned strain gauge measurement system was used to measure surface static pressures. Transducer calibration occurred approximately every hour, with barometric pressure as reference. The repeatability of the pressure measurement system was 0.05%, and estimated uncertainty of blade loading static pressure ranged from 0.07% to 0.44% based on experience.



Figure 21: Static Pressure Instrumentation on Baseline Nozzle

A five-hole traverse probe, shown in Figure 22 below, was used to obtain measurements upstream and downstream of the test section. NASA provided the five-hole traverse probe for the test and calibrated the

probe. The probe was a 45-degree forward-facing pyramid probe with the center port located on the probe shaft centerline. During testing, the probe was positioned by a remote computer-controlled actuator. The traverse probe sampled data in the flow-field for 123 points, spaced along the path of travel behind the test section. At each point, the traverse probe measured 5 pressures, which were input into a probe calibration scheme to produce the following output: total pressure, static pressure, exit angle of the flow, and probe angle. The probe was stop and go, with a 3 second settling time and 5 seconds of data acquisition per point. The traverse probe sampled data at midspan of the test articles. The uncertainty associated with flow angle measurements from the probe was reported as +/-1.5 degrees, and the probe was monitored during test to ensure it remained within angular calibration range. The pressure measurement uncertainty was reported as +/- 0.006 psi (41.4 Pa) based on a continuous check pressure analysis.

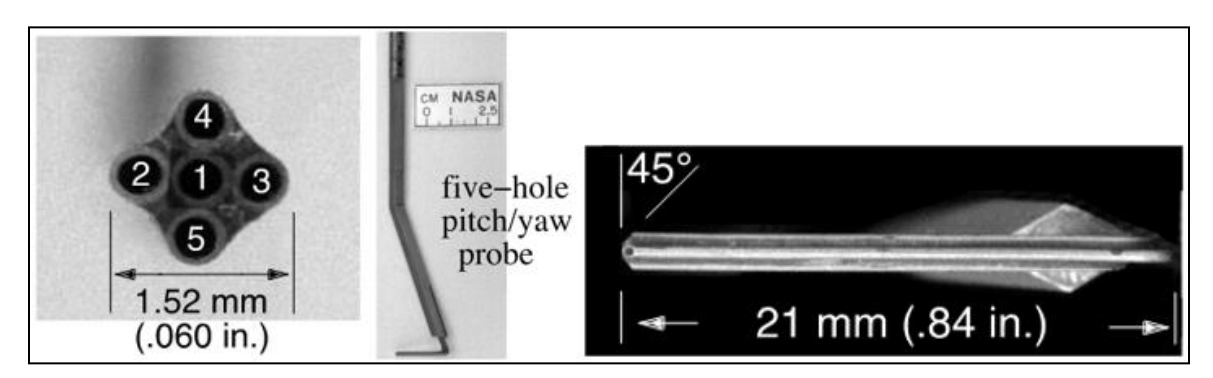


Figure 22: Five-Hole Probe Specifications

4.1.2.2 Background Oriented Schlieren

The Background Oriented Schlieren (BOS) technique was used to visualize the cascade rig flowfield for the cooled nozzle configuration [4]. The BOS technique measured the derivative of the density field and included this gradient in post-processed images. First, a large self-illuminating monitor was set up behind the test section (

Figure 23). The BOS team chose a speckle background for the monitor that allowed the perturbations in density to be visualized. The sum of all flow density variations across the width of the passages caused localized displacements in the speckle pattern. On the other side of the test section, a camera imaged the speckle background while the cascade was running. When the main flow was turned on and coolant was inserted into the test articles, a non-uniform density field was created in the test section that was captured by the camera. Live monitoring of the results was enabled by the computer processing software created by the team.

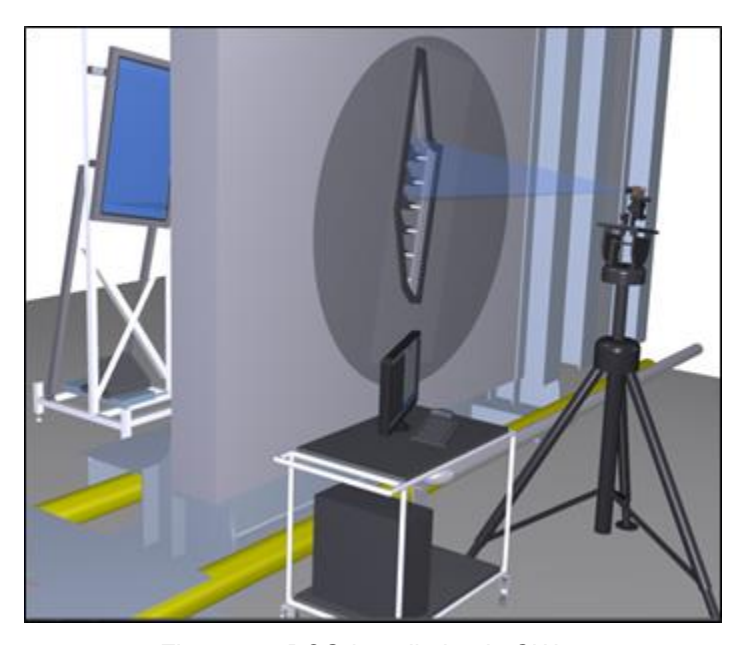


Figure 23: BOS Installation in CW-22

After running the rig with coolant, a reference image was acquired at the same main flow condition without coolant. This reference image was used to subtract out density gradient effects captured by the camera that were not representative of coolant insertion.

The image data was processed by performing a cross-correlation operation, similar to Particle Image Velocimetry data post-processing. The images were divided into small regions, and cross-correlation yielded the local x- and y-components of density variation across the integrated flowpath. The final composite images provided the magnitude of the density variation.

4.1.2.3 Facility Test Enabling Hardware

The facility test section had sidewalls on either side of the cascade which provided instrumentation access ports, traverse probe slots, and attachment points for the airfoils in the cascade. However, the facility sidewall allowed only for a fixed pitch of 5.119" (130.0 mm). While the medium and baseline solidity configurations had the same fixed pitch, the low solidity configuration was set at a larger pitch of 6.399" (161.0 mm). Therefore, a new sidewall was manufactured to interface the low solidity test articles with the facility test section. Additionally, BOS imaging necessitated optical Plexiglass windows. A new optical Plexiglass sidewall was manufactured to interface the low solidity test articles with the facility test section for the BOS portion of testing.

Upon arrival at the test facility, manufacturing defects were observed with the newly manufactured sidewalls. On the west sidewall, the instrumentation slots were tapered, preventing traverse hardware from being installed. The inspection report from the vendor said the slots were in tolerance but only on one side of the wall. The slots tapered inward towards the inboard side by about 0.007" (0.178 mm), likely due to tool deflection. The test team was able to mill the taper to successfully mate the traverse and west sidewall slot. Additionally, the increased pitch sidewalls called for 10-32 screws to hold the traverse hardware to the sidewall, instead of the NASA standard 1/4-28 screws. The east sidewall had incorrectly located lifting bolts, likely due to the use of an older NASA interface model. The lifting pattern should have been consistent between the west and east sidewalls. In future testing, all test facility mating hardware should be fit checked for mating features at the vendor. When a fit check is not possible, more detailed inspection will be required. A Geometric Dimensioning and Tolerancing review on all critical test enabling hardware before assembly with the facility would also be recommended.

The existing turbulence grid which has been used successfully for many years in the facility is an array of 1" (25.4 mm) square bars on a 6" (152.4 mm) pitch, with upstream blowing from a secondary air source to minimize pressure deficits in the wake. The cross bars and vertical bars in the grid are hollow with holes that are fed by shop air. Small holes drilled in the upstream face of the square bars in the grid direct jets of air directly into incoming flow. The air through the turbulence grid holes is measured by a separate mass flowmeter, which controls the amount of air flowing through the turbulence grid holes to a certain percentage of incoming rig air. The percent blowing of the turbulence grid refers to the percentage of incoming rig flow going through the grid holes. For example, 1% blowing means that the mass flow through the turbulence grid is 1% the value of incoming rig air. This turbulence grid generated approximately 13% turbulence. For this application, a lower turbulence level was desired. Several configurations of modified turbulence grids were tested, but none were deemed acceptable. A perforated plate was tested but proved to have excessive pressure drop. Several variations of square bar grids with and without upstream blowing were tested, but all produced unacceptable variation in inlet pressure profiles. While the team was converging on a solution and likely would have found an acceptable answer, schedule pressure resulted in the decision to eliminate the lower turbulence level from the test matrix, as time had not been allotted in the schedule for extensive turbulence grid development work. For future testing, a pre-characterized turbulence grid should be selected, or at least six months should be accounted for to characterize a new grid.

4.1.3 Test Plan

The CW22 facility operating envelope was used to determine the design point and off-design points for the test matrix. Figure 24 shows the rig's historical experience, and the test matrix points were verified to be within historical capabilities.

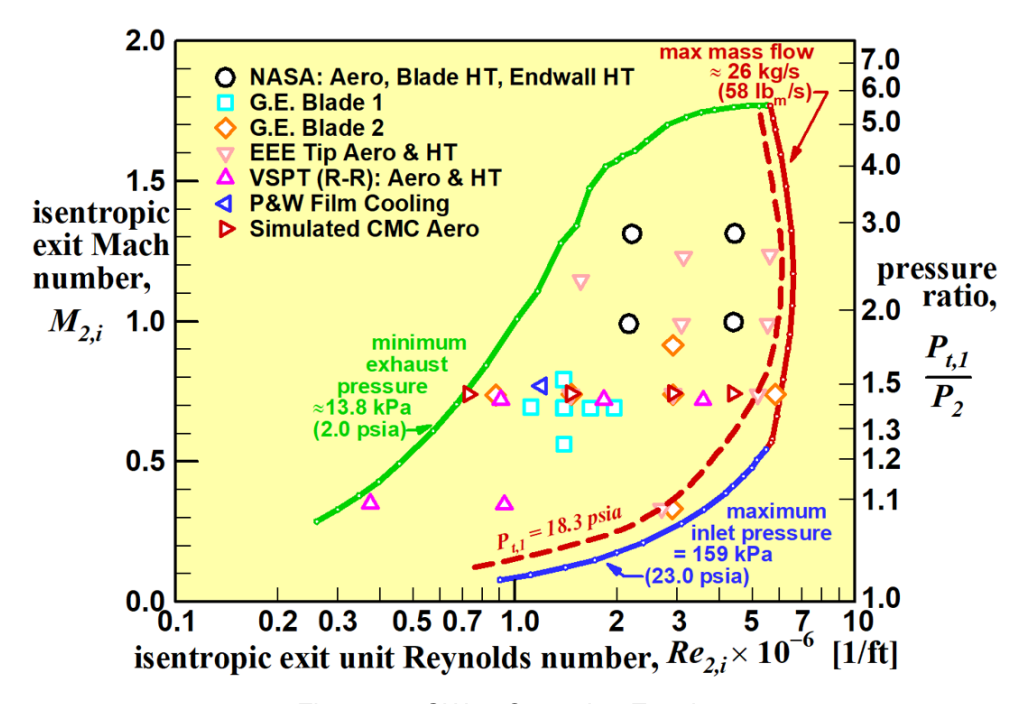


Figure 24: CW22 Operating Envelope

Three solidity builds were planned for the first part of testing for solidity. To create the test matrix plan for each solidity, a Box-Behnken DOE was implemented to understand coupled effects. The cascade allowed for variance of the following parameters: Reynold's number, pressure ratio, incidence, turbulence, and coolant flowrate/blowing ratio. The DOE enabled definition of a quadratic model for each variable pair and 2D maps for each relationship. A single airfoil configuration for the uncooled testing required

25 conditions per traverse location for a full resolution of potential variables, and a coolant airfoil configuration required 13 conditions per traverse location for full resolution of potential variables.

The solidity and coolant studies had different variables of interest. The solidity study focused on aero losses and required a 4-factor Box-Behnken, while the coolant study was focused on coolant mixing losses and required a 3-factor Box-Behnken. The pressure ratio and turbulence settings were consistent between both studies to keep results comparable.

Based on the results of the DOE, a test matrix was created that assessed the different independent rig variables. Table 8 demonstrates the conditions at which each solidity was tested.

Test Parameter	Tested Values		
Solidity	Baseline, Medium, Low		
Incidence Angle [%]	-100, 0, 100		
Reynold's Number	Low, Medium, High		
Rig Pressure Ratio	0.87 of Design, Design, 1.13 of Design		
Turbulence	0%*, 13%		

Table 8: Solidity Test Cases and Derivative Studies

Two builds were planned for the second part of testing for cooling: low solidity with coolant and medium solidity with coolant. Each build had three rows of coolant, labeled as forward, middle, and aft corresponding to the location on the airfoil suction surface (Figure 25). Forward and aft coolant rows had ten cooling holes, while the middle row of medium solidity had nine cooling holes, as they were staggered by half a pitch. Three static pressure taps were in line with each of the three cooling rows to measure external static pressure at the injection site.

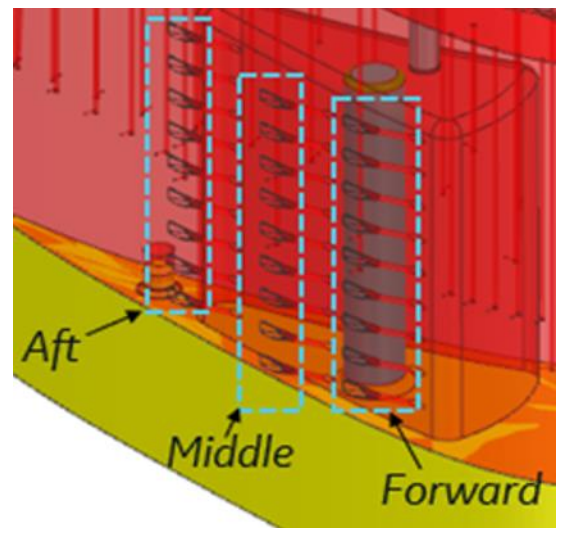


Figure 25: Cooled Nozzle Configuration with Three Cooling Rows

A test matrix was developed for the cooled nozzle configurations based on coolant pressure ratio, as shown in Table 9. The coolant pressure ratio was determined by taking the ratio of plenum pressure inside the test article to the external static pressure near the coolant injection sites. The design coolant pressure ratio was representative of nozzle design conditions. While the test matrix used coolant pressure ratio to control coolant, specifying target coolant mass flow may also be used in future testing to better control coolant. All runs were performed at the rig design point chosen for solidity testing. All three individual rows of coolant were tested, along with all rows open (with coolant) and all rows closed (with no coolant). To test individual rows of coolant at a time, Scotch tape was used to cover the coolant holes while keeping static pressure taps open for measurement acquisition. During the test, visual checks of the tape during runs at higher coolant pressure ratios were performed. While the tape bulged slightly with pressure behind it, a well-sealed area between the hole and edge of tape was confirmed. A configuration with all the cooling rows closed with tape was run to establish a baseline condition and eliminate any effects of the tape on the nozzle surface. BOS measurements were also included in the test matrix for the cooled runs at all design and off-design points.

Table 9: Cooling Test Cases and Derivative Studies

Test Parameter	Tested Values
Solidity	Medium, Low
Coolant PR	0.75*Nominal, 0.875*Nominal, Nominal, 1.125*Nominal, 1.25*Nominal
Configurations	Row 1 Row 2 Row 3 All

When creating the test schedule, all configuration changes were estimated and accounted for. For the test team, a typical test day was estimated to be around 6-7 hours of runtime, with 1-2 hours of start-up and shut-down procedures. Completing data collection with a traverse survey would take 40 minutes, with approximately 10 minutes required to set the next condition, changing Reynolds number or pressure ratio. Based on this, 6-8 test points were planned for each air period. For configuration changes, changing the incidence of the rig was estimated to cost 8 hours. Changing the sidewalls to account for pitch differences between solidity configurations was estimated at 16 hours. While the test team became very proficient at these configuration changes and performed them more quickly than initial estimates, it is recommended that for future testing, more work be done in the test plan to minimize reconfigurations to reduce overall test time and effort.

Certain compromises were made with the test plan to maintain schedule. The test was planned to run at two turbulence levels. However, due to difficulties in obtaining a grid at the lower turbulence level, it was decided to run at a single, readily available turbulence level for all three solidities. A run with near 0% TI was performed for a single condition for low solidity by removing the turbulence grid completely.

For test documentation, Items of Interest (IOIs) were documented by the NASA team for each test run and distributed by the GEA test focal. A rhythm was also set in place between the NASA and GEA team for data processing and handling (Figure 26). After running a test, the NASA test team would post-process the collected data through their script. Then, the post-processed data would be provided to the GEA team through a secure shared folder for interpretation and separate post-processing. Data post-processing time took longer than expected. Initially it was assumed that data would be available the day after testing, however it took up to two weeks, especially at the beginning of testing. This was due to the cadence of

testing called for in the test schedule – NASA personnel were not available to process data as it was taken due to the need to immediately re-configure the rig to the next test condition. In future testing, additional days should be built into the test schedule for data processing.



Figure 26: Flowchart Demonstrating Data Transfer Process

4.1.4 Test Article Design

The span of the test articles was set to fit the facility configuration. Three of the airfoils in the cascade (labeled Blade 4, Blade 5, and Blade 6) were instrumented for obtaining measurements of surface static pressure and downstream total pressure. For solidity testing, the three instrumented airfoils were additively manufactured from plastic Stereolithography (SLA) for incorporation of the static pressure tap passages. A mechanical deflection analysis was performed for the plastic airfoils to quantify flexure of the trailing edge relative to the metal blades. The trailing edge deflection was deemed acceptable as deflections were less than the drawing tolerance. The non-instrumented airfoils were manufactured from metal. Figure 27 compares the three solidity configurations for the metal hardware.



Figure 27: Uninstrumented Test Articles for (a) Baseline (b) Medium and (c) Low Solidity

For cooled nozzle testing, the instrumented nozzles were additively manufactured from plastic for simple incorporation of cooling hole geometry and instrumentation passages (Figure 28). The nozzles were manufactured in two parts and glued together with epoxy for assembly. Upon installation in the rig, leakage was observed at the seam where the two nozzle parts were glued together and where the airfoils met the sidewalls. The leakage was likely due to the brittle adhesive used, which was unable to maintain a seal under pressure. A more flexible adhesive was used to correct this issue.

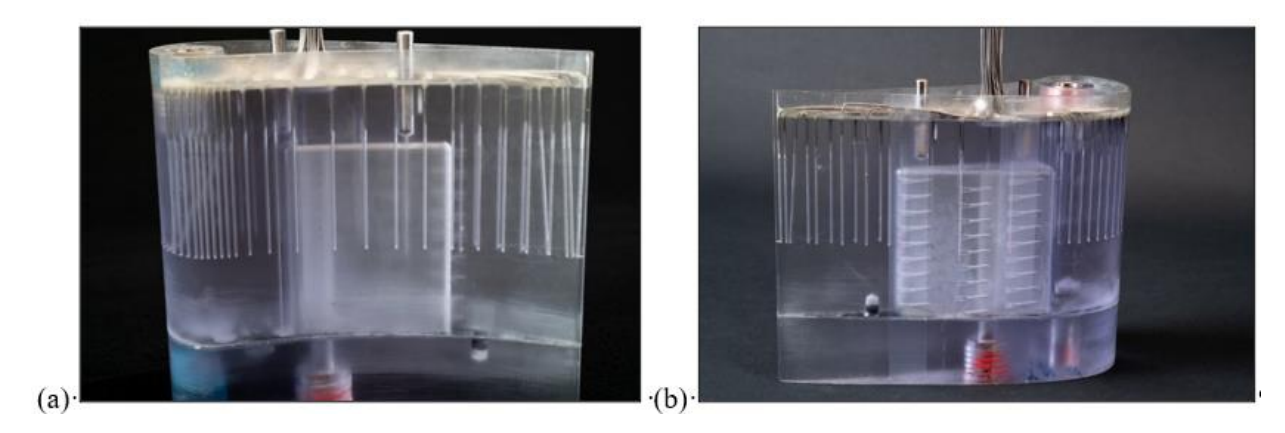


Figure 28: Instrumented Test Articles for Cooled (a) Medium and (b) Low Solidity

4.1.5 Summary of Completed Testing

The CW22 S2N Linear Cascade test campaign began on June 17, 2022, and all required testing was completed on February 16, 2023. The main test objectives were accomplished as shown below:

- ✓ Downstream data collection for three solidity configurations COMPLETE
- ✓ Downstream data collection for two cooling configurations COMPLETE
- ✓ BOS imaging for both solidities with all coolant rows open COMPLETE

Table 10 below shows the final executed test plan.

Table 10: Final Executed Test Plan

	Test Run Type	Configuration	Execution Date
	Inlet Characterization	Baseline, 100% incidence	6/17/22
	Downstream Traverse	Baseline, 100% incidence	6/30/22
	Downstream Traverse	Medium 100% incidence	9/12/22
	Inlet Characterization	Medium, 0% incidence	9/15/22
	Downstream Traverse	Medium 0% incidence	9/19/22
	Downstream Traverse	Baseline 0% incidence	9/22/22
	Inlet Characterization	Baseline, -100% incidence	10/18/22
(1)	Downstream Traverse	Baseline, -100% incidence	10/20/22
Solidity	Downstream Traverse	Medium, -100% incidence	10/25/22
Testing	Inlet Characterization	Low, -100% incidence	11/3/22
	Downstream Traverse	Low, -100% incidence	11/7/22
	Inlet Characterization	Low, 0% incidence	11/10/22
	Downstream Traverse	Low, 0% incidence	11/15/22
	Downstream Traverse (No Turbulence Grid)	Low, 0% incidence	11/16/22
	Inlet Characterization	Low, 100% incidence	11/21/22
	Downstream Traverse	Low, 100% incidence	11/22/22
	Downstream Traverse	Low, All Holes Open	12/14/22
	Downstream Traverse	Low, Forward Holes Open	12/15/22
	Downstream Traverse	Low, Middle Holes Open	12/16/22
	Downstream Traverse – Repeat	Low, All Holes Open	1/11/23
	Downstream Traverse	Low, Aft Holes Open	1/12/23
	Downstream Traverse	Low, All Holes Closed	1/13/23
(2)	BOS	Low	1/18/23
Cooling	BOS – Repeat	Low	1/19/23
Testing	Downstream Traverse – Repeat	Low, Forward Holes Open	1/24/23
resung	Downstream Traverse – Repeat	Low, Middle Holes Open	1/25/23
	Downstream Traverse	Medium, All Holes Open	2/1/23
	Downstream Traverse	Medium, Aft Holes Open	2/6/23
	Downstream Traverse	Medium, Middle Holes Open	2/9/23
	Downstream Traverse	Medium, All Holes Closed	2/10/23
	Downstream Traverse	Medium, Forward Holes Open	2/13/23
	BOS	Medium	2/16/23

4.2 CW22 Stage 1 Blade

4.2.1 Test Objective

The objective of S1B linear cascade testing was to understand the leading-edge stagnation and performance behavior of different low solidity configurations at varying incidence. Leading-edge stagnation data is critical for HPT blade thermal design since the blade leading edge undergoes the most thermal stress during operation. Assessing the stagnation region with incidence will help to design adequate cooling for both on and off design conditions for varying solidity. By comparing pressure loss, blade loading, and stagnation data between each solidity build, the design team was able to meet the test objective. Overall performance was measured via wake pressure loss. Profile, trailing edge, and shock losses combined into the measured wake loss and were analyzed to build a loss bucket for varying incidence. Since the test traversed the center of a linear cascade, secondary effects were assumed to be negligible. GEA designed the test hardware, which consisted of the S1B airfoils and the accompanying test enabling hardware to set the solidity via the pitch of each airfoil. NASA Glenn, provided the test facility, accompanying rig instrumentation, and resources to run the test during the test campaign.

4.2.2 Test Facility

The S1B test was run in the NASA Glenn Transonic Turbine Blade Cascade (CW22). See Section 4.1.2 for details surrounding the facility, instrumentation, and operation (note that Section 4.1.2.2 is not applicable for the S1B as no Background Oriented Schlieren was used).

4.2.2.1 Cascade Instrumentation

A two-dimensional cross section of the measurement system set-up in the cascade is shown in Figure 29. The setup is like that of the S2N Linear Cascade test, except this test used an upstream traverse to characterize the inlet (Plane 0) and a downstream traverse to characterize the exit (Plane 3).

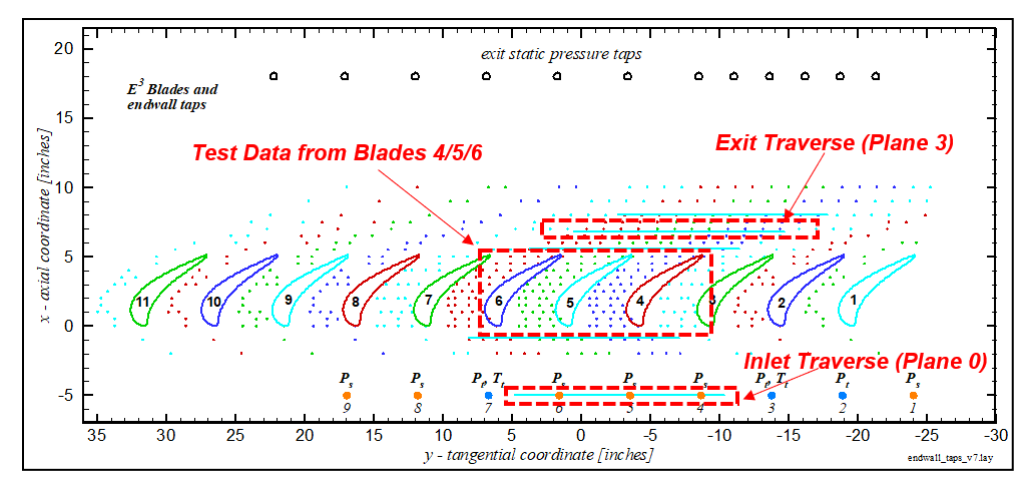


Figure 29: S1B Measurement Set-Up Cross Section

Static pressure measurements were taken on the surface of the test articles to produce airfoil loadings. The static pressure instrumentation tubing was routed by the NASA instrumentation team from the airfoil into a bundle that fed through an opening in the rig endwall to pressure transducers. The static pressure instrumentation on one of the blade configurations is shown in Figure 30 below. The three solidity test articles had the same number of static taps on the surface, with more static taps clustered at the leading edge for understanding the stagnation region. The static pressure taps were used to verify periodicity, obtain

blade loadings under operation, and inform pressure sensitive paint (PSP) testing (detailed in the next section).



Figure 30: Baseline Blade Static Pressure Instrumentation - Close-up of Ps Taps

4.2.2.2 Pressure Sensitive Paint Instrumentation

PSP was implemented for the first time in the facility to better understand the impact of incidence on stagnation region. Static pressure taps on the airfoils help to assess the stagnation point using blade loadings. However, the test objective of understanding the stagnation region and how it migrated across the entire span of the airfoil led the test team to optical instrumentation methods. The team agreed in the design phase that PSP was a promising method to capture and analyze high resolution stagnation region data. The test team helped to procure and test PSP data capture methods with the help of NASA PSP experts.

The paint, which was directly applied to S1B airfoils, was excited by an illumination source and the data near simultaneously captured by a photodetector. A borescope mounted on sidewalls outside of the flowpath was used to transmit the illumination source and photo-capture the data. A quartz window installed in the sidewall was used to transfer the illuminating light from outside the sidewall onto the S1B test article in the flowpath. Quartz was used as the material of choice for its transparency and structural rigidity to withstand rig conditions at atmospheric and near vacuum conditions. Figure 31 below illustrates the process. The borescope was mounted to the sidewall using dampers and rails to help mitigate any vibration outside of the sidewalls (Figure 32). PSP was directly applied to the instrumented airfoils to provide static pressure data in the form of contours of the stagnation region paired with static pressure taps to quantify the levels of those contours. Figure 33 below showcases images of the painted instrumented S1B airfoils.

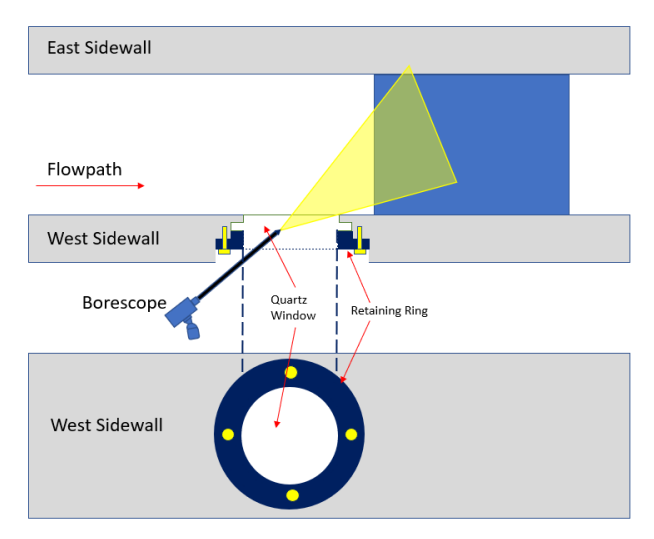


Figure 31: PSP Setup and Quartz Window Specifications

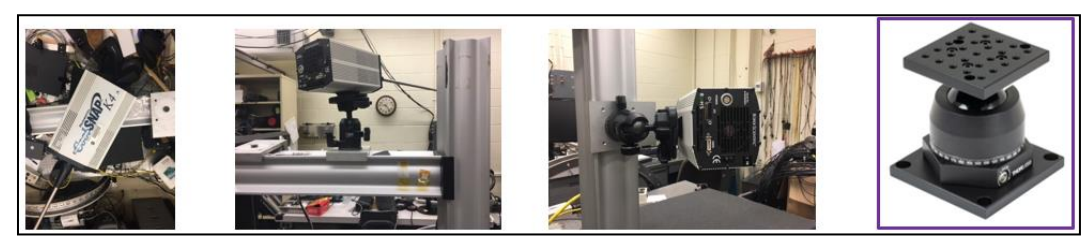


Figure 32: Rails and Damper for Borescope Stability

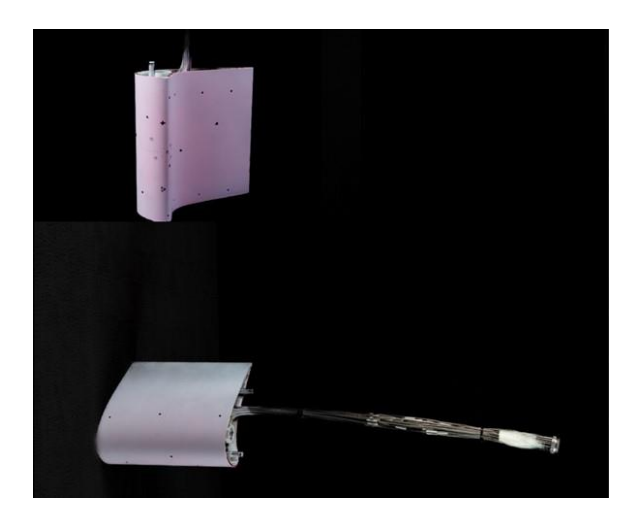


Figure 33: Painted Instrumented Airfoil

4.2.3 Test Plan

To assess conditions reflective of in-flight engines, the design team benchmarked to GEA's type certificated SoA. Table 11 below summarizes all the variables controlled in the test. At each combination of solidity and incidence, all variations of Reynolds Number and pressure ratio were run for a particular test period on the same day.

Controlled Parameter
Pressure Ratio (PR)

0.9*Design / Design /
1.03*Design

Reynolds Number (Re)
Cruise / Takeoff

Turbulence Intensity
13%
Incidence [%]
-100 / -47 / 0.0 / +50 / +100

Solidity
Baseline, Medium, Low

Table 11: Test Matrix Controlled Parameters

4.2.4 Test Article Design

The airfoil sections discussed in Section 3.2. required scaling to fit into the CW22 rig. The span of the test articles was set to fit the facility configuration. Table 12 below provides a comparison of the test article design features.

	Baseline	Medium	Low
Pitch/Pitch _{Ref}	0.8	1.0	1.3
Span	6"	6"	6"
# Blades	11	9	7

Table 12: Quantitative Comparison of 3 Tested Solidity Blades

Two models were created for each solidity: an instrumented version and a non-instrumented version. The non-instrumented airfoils were solid metal and served to establish periodicity in the cascade. The instrumented airfoils were lined with 55 surface static pressure taps in the midspan region to capture loading data.

The design of the test enabling hardware included three new sidewall sets specifically designed, manufactured, and assembled for this test. Solidity was changed by altering the spacing (pitch) between each airfoil. Each sidewall set included an East sidewall to house all facility instrumentation and a West sidewall to house the traverse and PSP instrumentation. See Figure 34 below for a comparison of East and West sidewalls.

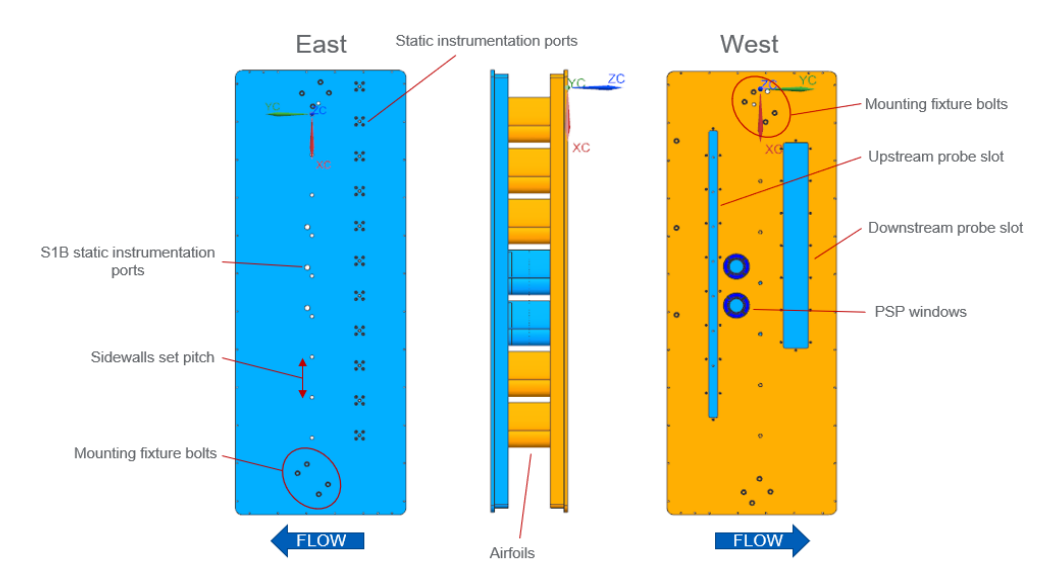


Figure 34: Sidewall comparison between East and West (x3 for each different solidity build)

4.2.5 Summary of Completed Testing

The CW22 S1B Linear Cascade test campaign began on April 6th, 2023, and all required testing was completed on November 21, 2023. The main test objectives were accomplished as shown below. See Section 5.2.5 for discussion on the PSP objectives not being met for two solidities:

- ✓ Downstream data collection for baseline count COMPLETE
- ✓ Downstream data collection for medium solidity COMPLETE
- ✓ Downstream data collection for low solidity COMPLETE
- ➤ PSP data collection for baseline count INCOMPLETE
- ✓ PSP data collection for medium solidity COMPLETE
- **✗** PSP data collection for low solidity − INCOMPLETE

Table 13 below summarizes the final executed test plan.

Table 13: Final Executed Test Plan

Build	Test Run Type	Incidence [%]	Execution Date
	Inlet Characterization	-100	4/11/23 11/29/23
	Downstream Traverse	-100	4/13/23 11/30/23
	Inlet Characterization	-47	4/5/23
	Downstream Traverse	-47	4/6/23 9/19/23
Dogolius Coliditu	Inlet Characterization	0	4/18/23
Baseline Solidity	Downstream Traverse	0	4/20/23 9/13/23
	Inlet Characterization	50	4/25/23 11/17/23
	Downstream Traverse	50	4/27/23 11/21/23
	Inlet Characterization	100	5/2/23
	Downstream Traverse	100	5/4/23

Build	Test Run Type	Incidence [%]	Execution Date
	Inlet Characterization	-100	6/21/23
	Downstream Traverse	-100	6/23/23
	Inlet Characterization	-47	6/8/23
	Downstream Traverse	-47	6/12/23
	Inlet Characterization	0	5/31/23
Medium Solidity	Downstream Traverse	0	6/2/23 11/9/23
	Inlet Characterization	50	5/24/23
	Downstream Traverse	50	5/26/23
	Inlet Characterization	100	5/22/23
	Downstream Traverse	100	5/11/23
	Inlet Characterization	-100	10/11/23
	Downstream Traverse	-100	10/17/23
	Inlet Characterization	-47	10/23/23
	Downstream Traverse	-47	10/25/23
I ow Colidity	Inlet Characterization	0	9/22/23
Low Solidity	Downstream Traverse	0	9/26/23
	Inlet Characterization	50	11/2/23
	Downstream Traverse	50	11/6/23
	Inlet Characterization	100	9/28/23
	Downstream Traverse	100	10/3/23

4.3 Transonic Research Turbine

The TRT is a single stage uncooled rig. This is a proven rig that has demonstrated a rapid change capability between builds. The rig uses magnetic bearings to reduce measurement uncertainty and enable the ability to detect the performance of individual aero features.

4.3.1 Objectives

This test had two main objectives:

- Advance technology performance validation in isolation from other flow features
- Validate use of FRAP to detect performance differences on a rainbow rotor

4.3.2 Test Facility

The rig is located at Notre Dame Turbomachinery Laboratory's White Field lab. The rig is shown in Figure 35.

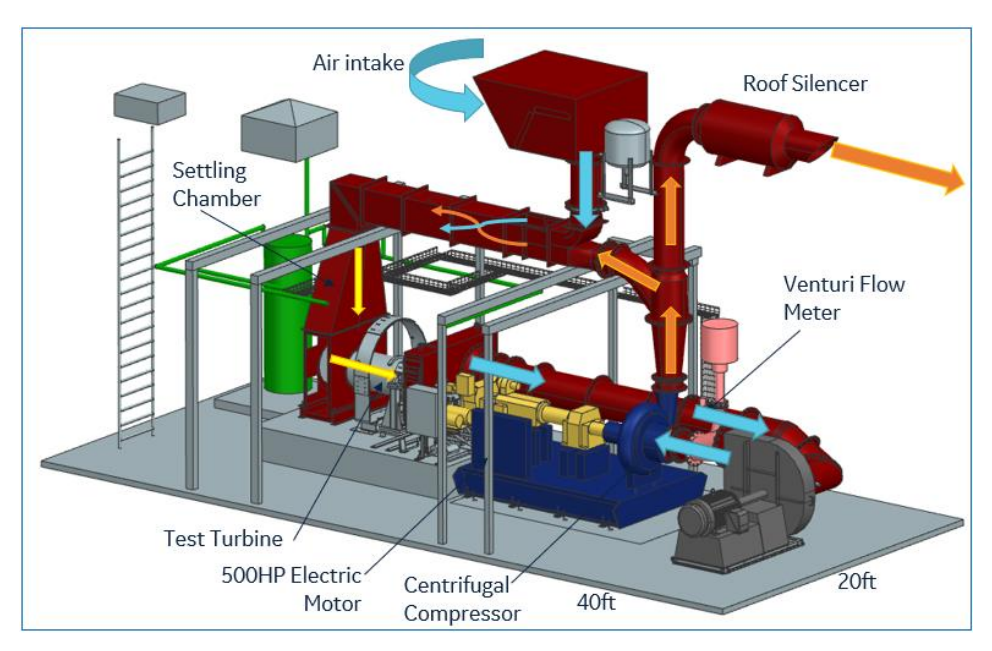


Figure 35: TRT Test Cell Schematic

Air enters the system through the air intake box at the top of the rig from atmosphere. It then flows into the mixer in which it is mixed with warm exhaust air to generate inlet conditions. The facility has an inlet airflow temperature limit of 250° F (121° C) with the nominal inlet temperature condition for this test being set at ~ 210° F (99° C). This air then goes into the inlet plenum before it flows across the test article. The blade tip stationary shroud is metal with an abradable coating. This shroud is heated to fine tune the tip clearance for each build. Aft of the blisk is the exit traverse plane in which the team uses either Fast Response Aero Probe (FRAP) or 5-hole probe to capture flow field detailed traverse surveys.

Downstream of the test article is the main air venturi flowmeter for the rig, which offers flow measurements with a \pm 0.2% uncertainty. Since the main air venturi measures the exit flow, the inlet flow is calculated by subtracting the measured purge flows that enter before and after the blade row. Aft of the main air venturi there are two compressors aligned in series. These compressors aid in pressure and temperature regulation. Upstream of the second compressor there is a recycle valve which opens and shuts to control inlet air temperature. This is done by letting some warm air back into the mixing chamber in which the rig exhaust air and fresh intake air are mixed. The remaining air leaves through the exhaust. Aft of the compressor is the compressor gearbox, a 500HP (373 kW) electric motor, a turbine gearbox, and a torquemeter. This torquemeter is a phase displacement torquemeter which has an uncertainty of \pm 0.1% (1 \pm 0).

Secondary flow systems deliver rig purge flow to the rig from a standalone claw compressor. This purge system includes orifice plates, temperature sensors and three purge lines which delivers purge flow.

4.3.2.1 Instrumentation

The TRT instrumentation is designed to measure the following calculated performance metrics:

- Rig operating conditions (PT and TT inlet, Pressure ratio and wheel speed)
- Rig flow function
- Stage efficiency

Instrumentation Plane and summary for TRT are shown in Figure 36.

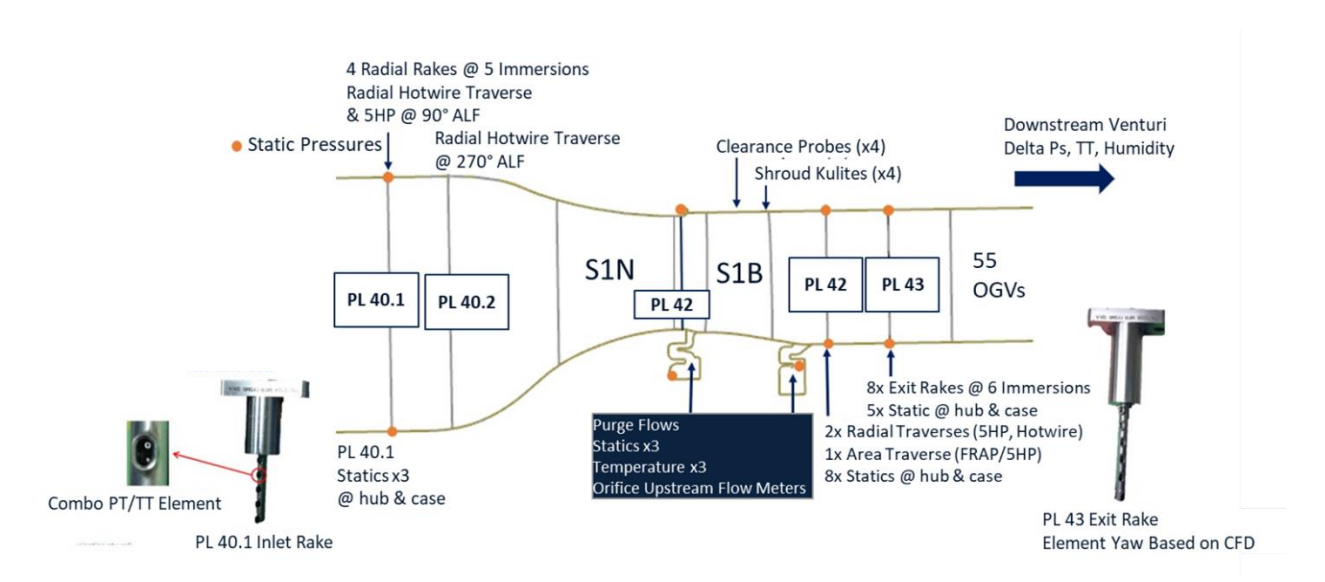


Figure 36: TRT Rig Instrumentation Layout

Below is the Flow path instrumentation for TRT.

- 4 Radial Rakes at plane 40.1
- Radial hotwire traverse at plane 40.2
- 41 Statics static pressure taps where 6 are at plane 40.1, 16 at plane 42 and 10 at plane 43. There are 3 static pressure taps in each of the 3 purge cavities
- 4 Clearance probes over the top of the stage 1 blade tip
- 4 Shroud kulites
- 2 Light probes
- 4 Radial traverse, 1 at plane 40.1, 1 at plane 40.2 and 2 at plane 43 (5-hole probe and a hotwire probe)
- 1 Area traverse (FRAP) at plane 42
- 8 Radial exit rakes at plane 43

Facility Instrumentation

- Torquemeter
- Main air venturi
- Humidity sensors at rig inlet
- Magnetic bearing radial and axial clearance sensors
- Gearbox proximity probes
- Turbine tachometer
- Cooling flow orifice plates and temperature sensors

4.3.3 Test Plan

Figure 37 shows a high-level test plan flowchart which details the general approach to test completion. This test procedure prioritizes balancing technical risk while prioritizing key data collection during testing. Initially the baseline concept will be prioritized as this is the control for the test. The other articles will be tested after and compared to the control test article, i.e., the baseline case. Throughout this planning procedure there will be setup phases in which mechanical checkouts (MCOs) will be conducted as well as calibration of the capacitance clearance probes (CAP). These CAP probes are used to record blade tip

clearances (TCL). For test points in which there are derivatives such as turbine mapping or purge derivatives the key turbine performance data is prioritized over derivative testing to ensure a minimum viable data set is collected as early in testing as possible.

						High Leve	l Test Plan					
Build	Build 1a	Build 1b	Build 1c	Build 2	Build 3	Build 4a	Build 4b	Build 4c	Build 5	Build 6a	Build 6b	Build 6c
Blisk	Baseline	Baseline	Baseline	Low Solidity	Non-Aero Tech 1	Non-Aero Tech 2	Non-Aero Tech 3	Non-Aero Tech 4	Rainbow B5	Rainbow B4	Rainbow B4	Rainbow B4
Purge Derivative	No	Yes	No	Yes	No	No	Yes	No	Yes	No	Yes	No
Turbine Mapping	Yes	Yes	No	Yes	No	No	Yes	No	No	No	No	No
Shroud	Open	Nominal	Closed	Nom	Nom	Open	Nominal	Closed	Nominal	Open	Nominal	Closed
RPM	100%	100%	100%	100%	100%	100%	100%	100%	97%	100%	100%	100%

Figure 37: High Level Test Plan

4.3.3.1 Test Operations

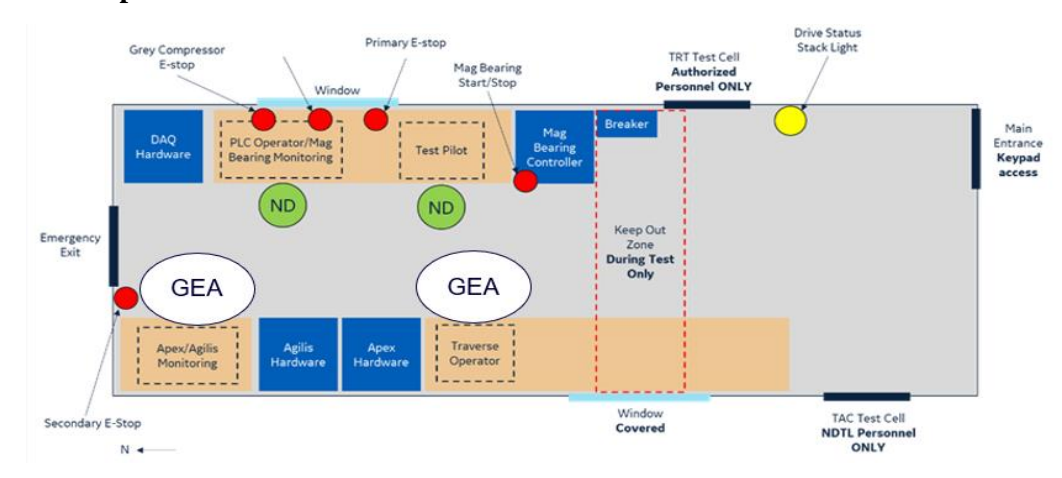


Figure 38: TRT Control Room

Figure 38 above shows a schematic of the test control room and where all personnel are stationed during testing. The test team consisted of a minimum of 4 people to staff each test station of the TRT Facility Control room. The 4 members and their functions were:

- GE Traverse Operator: Installs the traverse probe, and 5-hole and hotwire probes at the inlet and exit sections. Monitors the data collected by the probes throughout the test air period.
- GE Focal Point: Supervises the GE Test Team and makes decisions regarding the general test plan such as the test points for that day.
- NDTL Test pilot: The test pilot operates the rig and sets all the parameters from the specified test plan.
- NDTL Test Director- the test director is always present on-site during testing. The test director grants access the test cell and makes all final test cell operation decisions. The test commands will be given by anyone to the test director and at this point the director will acknowledge the command and make the appropriate action.

The approval to conduct testing was given once the MCOs were complete. The test air period began with a briefing from the test director. Then the ramp-up procedure began. In this procedure the rig was ramped up from stationary to the aero design point. Then data collection commenced, which took approximately 8 hours per test point. Once testing for that day was complete, a shutdown checklist was followed.

On each test day a health check was conducted on the rig. During this health check, steady state data of rig operating parameters were recorded and evaluated. This health check ensured that the recorded data was acceptable and tracked pretest predictions and health checks from previous runs. Pretest predictions were obtained from previous testing and from simulations. If the rig operating condition needed to be adjusted to ensure the data recorded was acceptable, a repeat traverse plunge was conducted. At the beginning of each area traverse survey an alignment radial traverse was performed in which the GEA traverse operator used pre-test predictions for swirl. This data was recorded and reduced to see how well the probe was aligned with the flow. The results obtained were then used to create a new radial distribution of probe yaw preset angle which was used for the full area traverse for that test air period.

LOG FILES

Log files were created for documentation. These files were documented during all aspects of testing to aid in any future TRT work. Main log files included:

- Test log: This log detailed the date, time, reading type, reading number, and data being collected. This log also had descriptions for any events which occur during testing. Upon an entry being made, the GEA/NDTL team determined if that event was a fault and decided if it should be "fix immediately", "fix before next run", or "fix when able" based on criticality to safety, performance, and availability of redundant measurements.
- IOIs: IOIs were documented and distributed by the GEA Test Focal after each test air period.
- Change Log: Changes to the rig configuration or facility were recorded using a change log. These changes include changes to the hardware, facility, and instrumentation. These logs were updated to ensure all information within was accurate.

DATA PROCESSING AND HANDLING

Data was processed from raw sensor signals to engineering units and delivered to GEA for post processing. Those physical measurements were converted to analog or digital signal as appropriate by a transducer. All analog measurements were converted to digital signal. NDTL uses Safran Test Cell's Cyres software for low frequency data acquisition and Apex for high frequency data acquisition.

The tip clearance measurement system is the same for both the steady state DAQ and the dynamic DAQ. A voltage reading was recorded as the capacitance changes with each blade passing the probe. The peak-to-peak voltage was a direct measurement of the clearance between the probe and the target blade tip. The high band amplifier converted the change in capacitance of the measuring system to a change in voltage. This waveform was then processed by the individual DAQs.

Low frequency data was managed in one of two different ways:

- 1. Live View: The data was processed live. This data was broadcasted to monitors in the test cell. Using the information displayed on these screens the test pilot altered rig conditions if necessary.
- 2. Recorded: Important identified data was recorded and stored on the local machine. Upon conclusion of the test day, the data was offloaded and preprocessed by NDTL. This process converted data from raw units to engineering units. NDTL used MATLAB based scripts to further process data to yield other variables of interest. This data was then uploaded to GEA via a secure drive. Once delivered, GEA post processed the data as needed for data analysis.

4.3.4 Test Article Design Summary

The baseline airfoil and blisk design were designed and analyzed in 2011 for yield strength, low cycle fatigue, high cycle fatigue, burst speed, and modal resonance. The baseline blisk ran successfully without any issues in both 2012 and 2013. Due to the age of the models and the fidelity of the past analysis, the

models were updated for the baseline airfoil to complete back-to-back stress analysis on the four new blisks. All blisk configurations met structural and modal resonance requirements as shown in Table 14.

Requirement	Criteria	Result
Yield	Peak Equivalent stress meets requirement	Pass
Low Cycle Fatigue	Peak Equivalent stress meet requirement	Pass
High Cycle Fatigue	Mean and Alternating Stress meets Goodman Envelope Requirement	Pass
Burst Speed	Burst Speed meets requirement	Pass
Modal Resonances	Speed margin on first flex meets requirement	Pass

Table 14: Mechanical Design Requirements & Criteria

The Ansys 3D Finite Element Model (FEM) was also updated to determine airfoil stress. Due to the increase in the mesh refinement, there was a slight increase in the max stress from the 2012 model in the suction side root fillet, but still below mechanical design criteria limits.

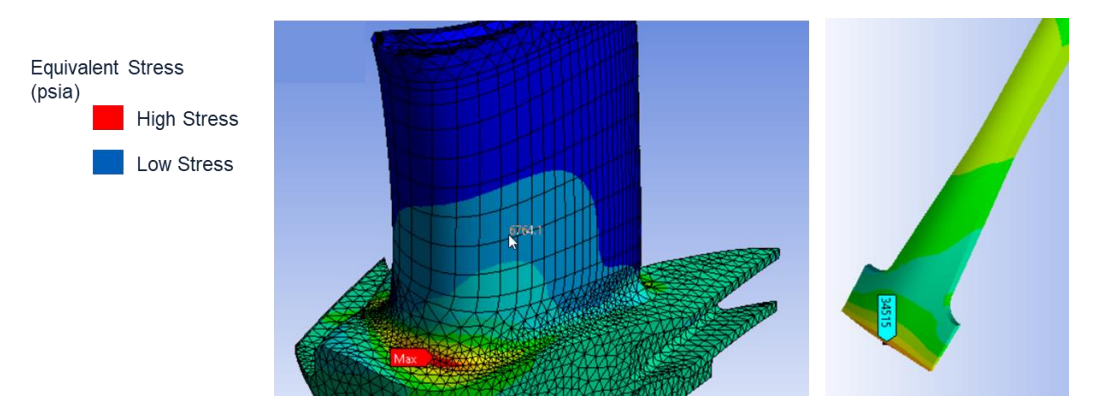


Figure 39: Baseline Blisk 3D FEM Results

The peak stress region was evaluated for crack propagation via a weak link assessment. The results of this assessment indicated the stress in this region was too low for any existing crack or formed crack to propagate. All blisks with platform contouring exhibited similar stress concentrations and location on the suction side fillet and therefore all passed the yield and fatigue requirements successfully.

The low solidity blisk required an increased suction side fillet size and hub 2D section stagger reduction to ensure adequate speed margin on first flex as mentioned in the airfoil design section above. The required geometry changes are included in the pre-test results reported in the low solidity section 3.3.3.

Due to the airfoil designs on the rainbow blisk containing the platform and no platform contouring, the blisk did not meet the speed margin on first flex. Due to the nature of the rainbow rotor, instead of iterating on the airfoils in each of the four quadrants, it would be easier, with minimal performance impact, to run that blisk at lower speeds than the ADP speed to maintain acceptable modal margins and meet design criteria. With the adjustments listed above on the low solidity airfoil design and the speed reduction requirement on rainbow blisk 2 (Figure 39), all blisks passed the modal resonance requirement.

Lastly, there was no update required to the rig dynamic models or the shaft models for each new blisk design.

4.3.5 Summary of Completed Testing

The first air period for the TRT phase 1 test campaign occurred in January of 2023. All required testing was completed on August 23rd, 2023. This test campaign had 12 builds and 4 MCOs. The run summary of the rig is shown below:

- Total TRT Bearing Time: 248 hours 42 minutes
- Total TRT Air Plant Time: 104 hours 42 minutes
- Total Rig Starts: 26
- Maximum Speed Range Cleared: 100%
- Maximum Obtained Total Inlet Pressure: This is atmospheric (~14.2 psia)
- Maximum Obtained Total Inlet Temperature: 671.58-degree Rankine

The main test objectives were accomplished as shown below:

- Mechanical Checkout Completed
- Purge Derivatives Completed
- Tip Clearance Derivatives Completed
- Turbine Mapping Completed
- Exit area traversing with the FRAP- Completed
- ADP Performance Data collected Completed

4.4 Stage 2 Nozzle Annular

4.4.1 Test Objectives

The goal of the S2N Annular test rig was to advance Stage 2 high-pressure turbine nozzle low solidity and high thickness-to-chord airfoils from TRL 3 to TRL 4. These airfoil shapes enable manufacturing techniques and technologies that eliminate the need for post throat cooling. To meet this objective, two test articles were developed:

- Baseline a current SoA S2N airfoil currently type certified and in operation.
- Optimized reduced solidity a new design airfoil, with similar loading level (at pitchline) as demonstrated in the CW22 S2N linear cascade testing, discussed above.

The annular cascade test would be considered successful if flow function vs pressure ratio characteristics for the two test articles can be obtained, and detailed performance data at the design aero point can be taken for a range of cooling flow rates for a representative post-throat cooling configuration for both solidities.

4.4.2 Test Facility

4.4.2.1 Facility and Rig Design

This testing was performed in the A8 test cell in GEA's Evendale facility. This cell is capable of continuous flow of pressurized air, exhausting to ambient at near ambient temperature conditions. This facility is used extensively for cold flow testing of a range of turbine nozzles and has a configurable array of choked flow venturis that can be customized to the flow needs of a given test. Coolant flow can be added by additional, independently controlled and metered circuits, either from shop air (for low flows) or from the main air supply for larger cooling flow demands. Additionally, the facility can support traversing 5-hole pressure probe systems for detailed flow field pressure loss measurements.

Air enters the facility through the array of choked flow venturis, shown in Figure 40, and enters a settling plenum. The settling plenum contains an array of honeycomb for flow straightening, after which the air enters the test rig.



Figure 40: Main Airflow Choked Flow Venturis

A cross section of the S2N test rig is pictured in Figure 41. The rig mates to the facility using the adapter shown in orange. The adapter also carries the inner portion of the fixture and provides pass-throughs for inner band instrumentation so that instrumentation lead-outs do not traverse the exhaust plane. Air is accelerated from the facility plenum through the annular bellmouth to a pre-swirl vane, which is designed to generate a representative inlet swirl condition for the S2N nozzle. The air is then accelerated through the test article, exhausting to ambient. A second flow circuit is used to provide simulated cooling air to the test article. The coolant air enters the rig from the aft through four hoses. These hoses discharge to a plenum inboard of the nozzle ring, then the air enters each airfoil and is discharged to the flow path through the cooling holes. A traverse assembly is mounted aft of the test article. The assembly has the ability to traverse 360° circumferentially around the annulus, however only a limited region of the arc was used for this test. As both the pre-swirl vane and test article are made from SLA printed plastic, retention features are designed to spread the clamping loads of the bolts to avoid damaging the plastic parts. Both parts are retained by a clamp ring that is held in place by a pattern of bolts. Likewise, sponge cord is used for sealing rather than o-rings to minimize the forces imparted on the plastic components.

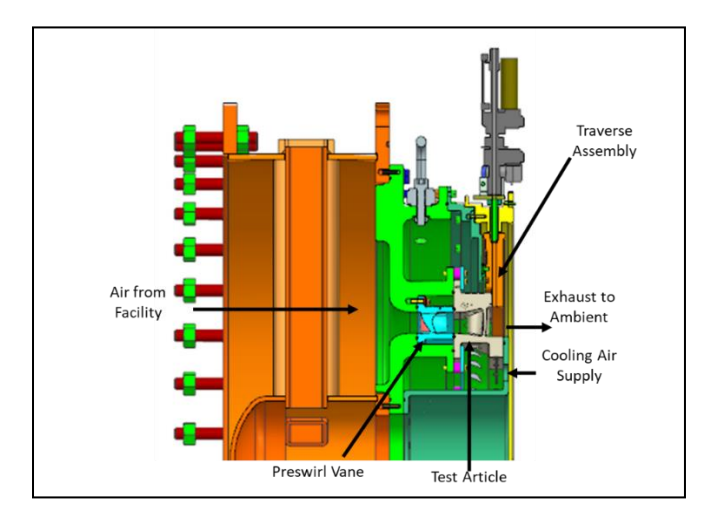


Figure 41: Test Rig Cross Section

4.4.2.2 Instrumentation

This test used the standard facility instrumentation and choked flow venturis for main air and coolant circuits to measure pressures, temperatures, and mass flows of incoming air. Additionally, the test article and rig were instrumented with 60 additional pressure taps, an additional thermocouple, and a five-hole probe. Verniered pressure taps were located aft of the nozzle, on both the inner and outer bands, to provide downstream pressure measurement for condition setting. Three pressure baskets and a thermocouple were arrayed around the cooling plenum to provide inlet conditions for the coolant circuit. Additionally, three airfoil cavities were instrumented with a pressure tap as a second witness to the coolant conditions in the flow circuit. This included ensuring that there was not significant pressure loss prior to coolant entering the cooling holes and that flow was equally distributed around the annulus.

A 5HP, as shown in Figure 42, was used to take detailed pressure measurements of the downstream flow field. It is capable of circumferential and radial movement to provide an area traverse behind the nozzle. Due to difficulties with the 5HP while on test, discussed further in Section 4.4.5, a Kiel probe was also used to provide a reliable indication of total pressure, independent of the flow angle.

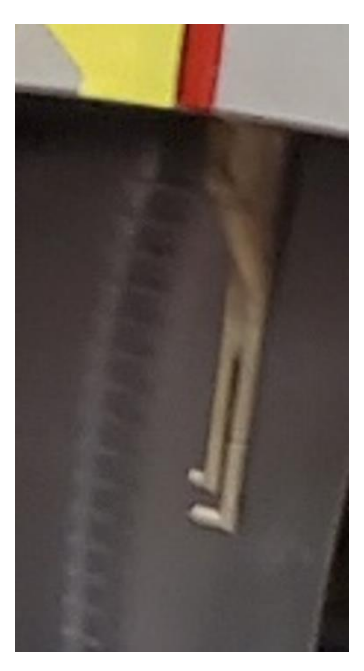


Figure 42: 5HP Installed on Aft Side of Rig

4.4.3 Test Plan

A series of test points as shown in Table 15 was defined to satisfy test objectives. For each test article, a main air pressure ratio sweep was conducted to characterize the flow characteristics of each test article. For this pressure sweep, the cooling level was set to the nominal value for all points. For these points, steady state data was taken to quantify flow capacity; no detailed downstream traverse data was acquired. Then, at the design pressure ratio, a cooling flow derivative was performed by varying the introduced cooling flow from 0 to 1.5x nominal mass flows.

Main Air Pressure Ratio	Cooling Mass Flow	Data Acquired
Non-ADP points	Nominal	Steady State (Flow)
ADP	0, Nominal, 1.5x Nominal	Steady State (Flow) and Downstream Traverse

Table 15: S2N Annular Test Matrix

At the design point, including the cooling flow derivatives, downstream traverses were taken over three wakes, with a total of three detailed traverses per test article. The traverse program used a continuous sweep methodology to minimize test time without compromising accuracy, following GEA best practices. Immersions were spaced with tighter radial spacing near the inner and outer bands to capture the expected differences in secondary flow regions of the two test articles.

4.4.4 Test Articles

The aerodynamic design of the airfoils is discussed in Section 3.4. The test articles were printed in segments due to size constraints of the available 3D printing machines. The baseline test article was printed in eight segments, while the reduced solidity required nine to avoid segmentation of features needed for clocking/mating with the rig. The test articles were assembled together using flat brackets and capscrews for positioning, and room-temperature-vulcanizing (RTV) sealant was applied on all mating faces for both structural capability and sealing of the test article.

Provisions for all pressure instrumentation on the test article were printed in, which allowed measurement locations to be clustered together on the flow path side of the article, while allowing additional space for installation of pressure tubing on the back side. Figure 43a and Figure 43b show the modeled and installed instrumentation, respectively.





- a) Modeled instrumentation (external faces hidden for clarity)
- b) Installed Instrumentation

Figure 43: Modeled and installed instrumentations

4.4.5 Summary of Completed Testing

The S2N Annular Cascade test campaign began on August 9th, 2023 and testing was completed on October 26th, 2023. The main objectives of the test were accomplished:

- Performance and flow function data collected for the baseline nozzle
- Performance and flow function data collected for the low solidity nozzle

Some repeated testing was required for the baseline nozzle as the 5HP used for the baseline the first time provided erratic readings. This was initially thought to be due to a faulty calibration, but post-test calibration did not correct the issue. It is likely that undetected physical damage or blockage existed in the original probe. Due to this, a new 5HP was selected for the remaining testing, and a Kiel probe traverse was added to provide a second witness to total pressure measurements for data validation. Table 16 below shows the final executed test plan.

Test Article	Probe Configuration	Test Date
Baseline	5HP (original)	8/9/2023
Low Solidity	Kiel	9/19/2023
Low Solidity	5HP (replacement)	9/26/2023
Baseline	Kiel	10/19/2023
Baseline	5HP (replacement)	10/26/2023

Table 16: S2N Annular Final Executed Test Plan

5. Test Results and Analysis

5.1 CW22 Stage 2 Nozzle

5.1.1 Data Summary

The objectives of the linear cascade were to quantify the effects of solidity and post throat cooling on high thickness to chord vanes. Both objectives of the CW22 S2N Linear Cascade test were completed and data quality was acceptable. At the aerodynamic design point, differences between low, medium, and baseline solidity performance were within measurement uncertainty. However, measurable differences between baseline, medium, and low solidity at off-design points demonstrated the robustness of low solidity at off-design conditions compared to higher solidity designs. Performance decreased as expected when post-throat cooling was added to medium and low solidity nozzles. Low solidity demonstrated a smaller performance debit than medium solidity with post-throat cooling. Background-oriented Schlieren imaging provided a physical understanding of the cooled nozzle test results. Pre-test and post-test CFD analyses were completed to match trends in the final data.

5.1.2 Data Acquisition and Reduction

Two non-dimensional coefficients were defined for post-processing to be used as figures of merit when assessing performance. The first non-dimensional coefficient is the coefficient of total pressure, defined in the equation below.

$$C_{p,t} = \frac{P_{t,1} - P_{t,2}}{P_{t,1} - P_{s,2}}$$

The coefficient of total pressure relates the difference in total inlet and exit pressure to the exit isentropic dynamic head. Exit static pressure stays constant during testing, and inlet total pressure does not change once set to the rig operating condition. However, the exit total pressure measured aft of the test section will change based on solidity and post-throat cooling configuration. Therefore, the total pressure coefficient was used as a measure of total pressure loss: a lower total pressure loss across the nozzle leads to better component efficiency and as such is an important measure of performance. The total pressure coefficient was computed with downstream total pressure measurements from the traverse probe and visually represented as wake profiles in data reduction. The second non-dimensional coefficient used was the coefficient of static pressure, defined in the equation below.

$$C_{p,s} = \frac{P_{s,local} - P_{s,2}}{P_{t,1} - P_{s,2}}$$

The coefficient of static pressure relates the difference in local static pressure on the exterior of the nozzle and rig exit static pressure to the exit isentropic dynamic head. Like the total pressure coefficient, the exit static pressure and inlet total pressure stays about the same during testing. Therefore, the static pressure coefficient demonstrates how the local static pressure varies on the surface of the nozzle during test. The static pressure coefficient also shows how local ideal velocity on the nozzle surface changes with surface length and chord, providing information about the distribution of loading on the nozzle. The static pressure coefficient was computed with measurements from nozzle surface static taps and visually represented as loadings in data reduction.

The main measure of performance used in data reduction was the total pressure coefficient. The two solidities and different cooling configurations were compared to one another in terms of total pressure coefficient, with the lowest total pressure coefficient demonstrating the best performance.

The test data was comprised of a set of traverse points distributed laterally across the downstream region at fixed distances from the nozzle trailing edge for a single survey, which made up the wake profiles shown in the results. To compare different configurations or solidities in terms of total pressure coefficient, an average was taken of the traverse test data across a single survey to produce a one-dimensional average total pressure coefficient. Since the test data included three test airfoils, averaging the data helped account for airfoil-to-airfoil variation with a single representative loss value. The one-dimensional averages were used to demonstrate general trends from testing and draw high-level conclusions.

The averaging technique used in this test was area-averaging. The test data was first fit with a spline curve in post-processing scripts. Next, the area under the fitted spline curve was integrated over each single wake period, corresponding to one of the three test airfoils. Finally, the three integrations were arithmetically averaged to get a single average value for the traverse survey.

Coolant injection adds more mass into the main rig air flow, albeit minimal, and had to be accounted for in post-processing. Due to the addition of mass flow from cooling both primary and coolant sources of total pressure need to be accounted for in the loss calculation. The additional mass flow impact on total pressure from coolant could be computed using a mass average of coolant and rig mass flows. The effect of this adjustment was small compared to the uncertainty of the rig measurements.

5.1.3 Rig Aerodynamic Validation

5.1.3.1 Inlet Characterization

In initial data, inlet angle variations were observed at the three facility inlet angle settings. Non-uniform variations in profile were observed for all three solidity configurations. The team decided to characterize the inlet at each facility angle setting and modify the cascade flow geometry at each end of the row to obtain a uniform inlet angle and pressure profile. A traverse probe located upstream of the test articles was used to collect inlet condition data, including pressures, angles, and Mach number.

Additional runs characterized the rig for inlet non-uniformity. The upper and lower gaps in the facility test vehicle were calibrated for each combination of solidity and rig angle configuration (Figure 44). By adding variable blockage to the rig in the upper and lower gaps of the rig, the inlet angle was controlled to match intent.



Figure 44: Variable Upper and Lower Gaps for Inlet Control

During characterization, variability with the turbulence grid blowing ratio was also observed. Blowing ratio was varied to minimize wake effects of the turbulence grid, with the optimal ratio varying for each configuration. For example, the baseline solidity obtained a uniform inlet profile with 0% blowing, while low solidity performed best with 1.0% blowing. Overall, the inlet characterization runs successfully created uniform inlet flow for the baseline, medium, and low solidity configurations at the three facility inlet angle settings. The same inlet characterization configurations found with the additional runs would be used for the cooled configuration runs as well.

As shown in Figure 45, adjusting the variable gaps in the rig for each solidity at all three inlet angles was successful at creating a uniform inlet profile. The variables tracked for the inlet stayed consistent around the intended value at all three pressure ratios, demonstrating the effectiveness of the inlet characterization efforts.

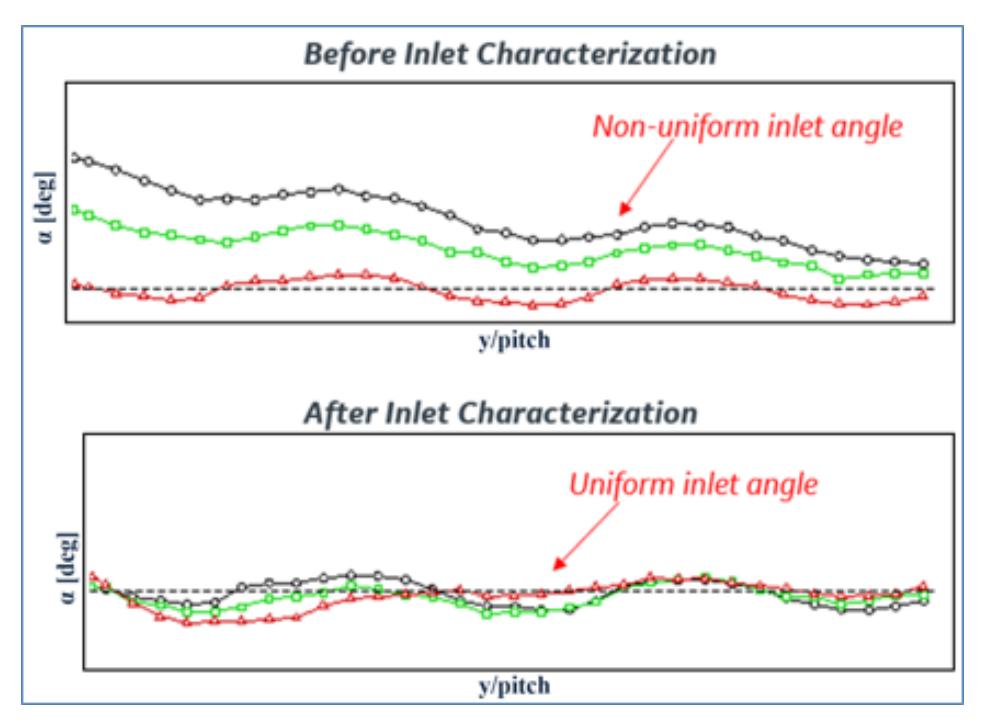


Figure 45: Before and After Inlet Characterization

The inlet characterization data provided inlet traverse pressures that were compared with singular Kiel probe inlet pressure. Examination of the inlet characterization data showed a nonzero inlet C_{p,total} (Figure 46), indicating a difference between the single inlet Kiel probe total inlet pressure and measured upstream traverse total pressure.

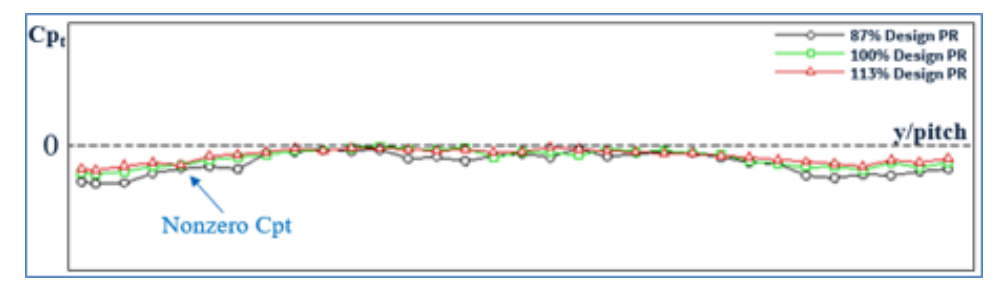


Figure 46: Nonzero Cp_T Highlighted in Inlet Profile

For the downstream traverse runs, the single Kiel probe value was used as a reference inlet total pressure. However, the inlet traverse measurement would better reflect the inlet conditions in front of the test section

(Figure 47). Therefore, a correction was introduced to adjust inlet total pressure in the downstream data to match the upstream traverse measurements of the inlet.

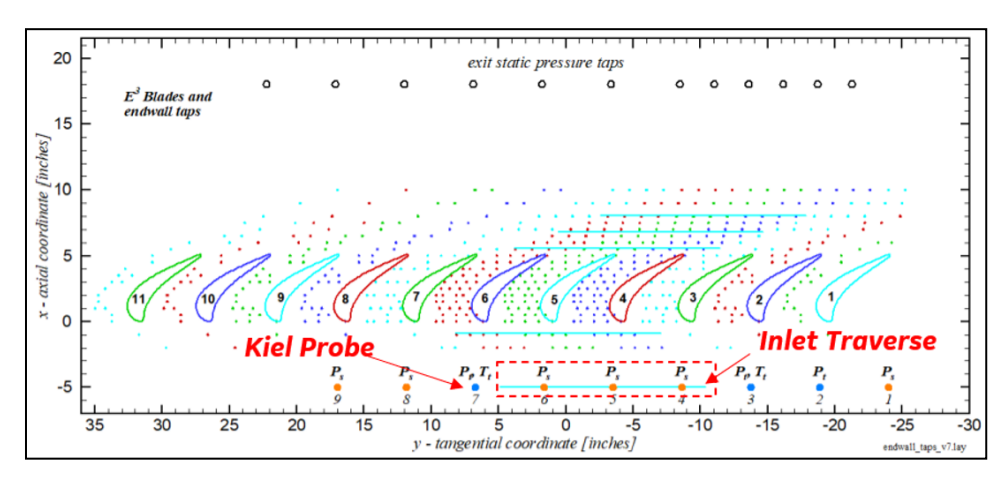


Figure 47: Kiel Probe and Inlet Traverse Location

The average $C_{p,total}$ from the upstream traverse data, inlet single Kiel probe, and upstream traverse static pressure was used to adjust inlet total pressure for the downstream traverse runs. Using this value, the downstream traverse total pressure, and the downstream traverse exit static pressure, the downstream traverse $C_{p,total}$ value was recalculated.

$$\begin{split} P_{t,in,Corrected} &= P_{t,in,Kiel} - C_{pt,in} * \left(P_{t,in,Kiel} - P_{s,in,Traverse} \right) \\ C_{pt,Corrected} &= \frac{P_{t,in,Corrected} - P_{t,ex,Traverse}}{P_{t,in,Corrected} - P_{s,ex,Traverse}} \end{split}$$

The correction was considered for each combination of solidity and inlet angle. Each configuration had a unique correction approach based on the available upstream data. Overall, small changes to the average loss trends were observed. On average, the inlet characterization correction changed the average $C_{p,total}$ results by less than 0.1%.

After adjusting for the cascade inlet profile, the variation between the wakes of the three test airfoils was assessed to ensure periodicity between the three airfoils. Standard deviation of the three average $C_{p,total}$ for each airfoil wake was calculated for each solidity configuration at each run condition for both uncooled and cooled nozzles. A measurement uncertainty analysis was performed for the cascade at its test matrix operating conditions. Each combination of pressure ratio, Reynolds number, and inlet angle had a corresponding uncertainty. All calculated standard deviations of the individual wakes were found to be within measurement uncertainty of the traverse probe (see Table 17). Therefore, the test data wake profiles were considered periodic.

5.1.3.2 Cascade Operating Conditions

The operating conditions of the cascade were assessed to determine if reported test conditions from the test runs would affect the final data results. A sensitivity study was performed to understand impact to $C_{p,total}$ from varying inlet total pressure, inlet total temperature, and exit static pressure. After preliminary studies with a cascade-matched 1D model, inlet total temperature was identified to have the largest potential impact to final $C_{p,total}$ results. Two operating points were chosen with the largest reported temperature difference between the three solidities during test: (with a $10^{\circ}F$ (5.6°C) temperature difference) and with a $20^{\circ}F$ (11.2°C) temperature difference). The cascade-matched 1D model was used to calculate losses with combinations of reported operating inlet total pressure, inlet total temperature, and exit static pressure. A Monte Carlo simulation was run using the ranges of inlet total pressure, inlet total temperature, and exit

static pressure as variable inputs. The standard deviation of $C_{p,total}$ output from the simulation (Table 17) demonstrate that the operating conditions would not appreciably impact final data results for $C_{p,total}$ beyond measurement uncertainty.

Table 17: Reported Operating Conditions Variation Assessment

Operating Condition	Case 1	Case 2
Measurement Uncertainty	$\sigma = 2.3E-3$	$\sigma = 1.9E-3$
Low Solidity	$\sigma = 8.0$ E-4	$\sigma = 7.6E-4$
Medium Solidity	$\sigma = 1.1E-3$	$\sigma = 1.0E-3$
Baseline Solidity	$\sigma = 8.0E-4$	$\sigma = 7.4E-4$

5.1.3.3 As-Tested Hardware vs. Design Intent

Upon each new configuration of the test section, the test team obtained multiple sets of throat measurements of the installed hardware. Throat measurements were obtained between all airfoils in the test section (airfoils numbered 1-11). Throat measurements were also taken by the test team prior to test article removal after a run. Measurements taken before and after summer shutdown showed variation after the long shutdown period. Additionally, the test team used two different measurement tools: inside mics and gage blocks/pin gages. In future testing, it is recommended to standardize the throat measurement process to obtain more consistent measurements.

The throat measurements were compiled and compared against the design intent throat to understand any deviations. Due to the measurement variation, the measurements closest to the downstream test traverse run were considered most test-representative. A timeline of all throat measurements taken was created to align test days and throat measurement days. An average of the test-representative instrumented blade throat measurements was taken for each of the three test articles. The impact of throat deviation to total pressure loss was assessed, and all calculated changes to $C_{p,total}$ from throat deviations were found to be within measurement uncertainty. Table 18 shows these results.

Table 18: Throat Measurements for Uncooled Test Articles

Measurement	Airfoil	% Diff	∆Cp,total
Gage block/pin	Baseline, Uncld	0.5%	1.6E-4
Gage block/pin	Medium, Uncld	0.1%	1.4E-5
Gage block/pin	Low, Uncld	0.0%	0

Trailing edge thickness measurements were obtained using a 3D scan of the trailing edge of the test articles. The measured trailing edge thicknesses were all within drawing tolerance. The drawing requirement was set to ensure a hydraulically smooth airfoil. Measurements verified that the roughness met the drawing requirements.

5.1.3.4 Probe Data Corrections

BOW WAVE DURING OPERATION

Initially, the airfoil loadings demonstrated non-periodicity: airfoil 4 had a different loading characteristic than airfoils 5 and 6. By examining sequential points from the traverse survey at all three operating pressure ratios, the cause for the discrepancy was determined. The aft loading anomaly for airfoil 4 was caused by a weak bow shock off the moving traverse probe during the survey, which impinged on the aft suction side of airfoil 4 during the first third of the survey. The bow shock off the probe was caused by the locally supersonic flow upstream of the traverse measurement head. Once the bow wave cleared Blade 4 after the

first 1/3rd of the traverse surveys, airfoil loadings were periodic as expected. Therefore, loading data was taken from the last point the traverse survey to avoid the bow wave effect. Figure 48 shows the direction of the traverse probe during operation, which aids to visualize the bow wave coming off the traverse probe and hitting airfoil 4.

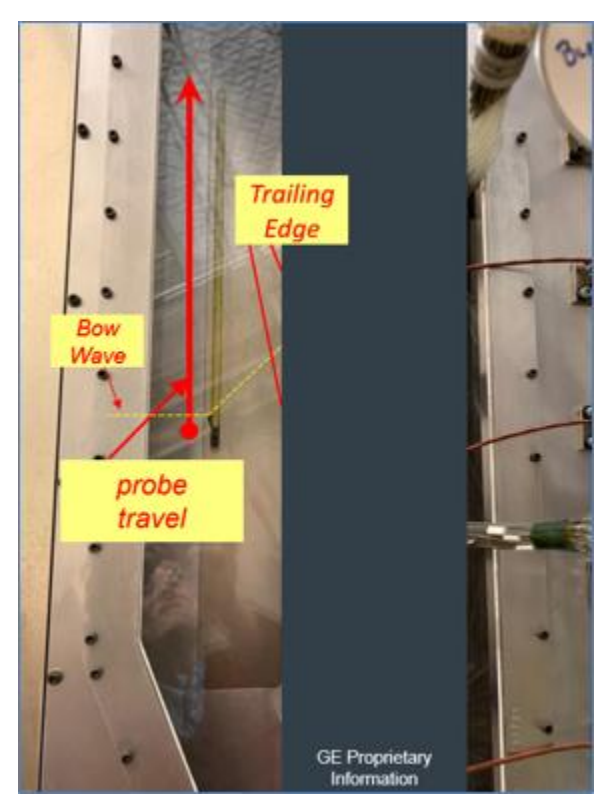


Figure 48: Direction of 5HP Travel to Visualize Bow Wave

Figure 49 demonstrates the difference observed in blade loading at different points in the traverse survey. In the tenth traverse point, the loading difference between the three test articles demonstrates the probe bow wave effect on non-periodicity (Figure 49, left). Conversely, the probe bow wave has passed the test section by the last traverse point. The last point in the traverse survey shows the expected periodic loading between the three test articles (Figure 49, right). As the probe moves behind the airfoils, the non-periodic region initially grows and then decreases in the airfoil loading. After the probe has passed the airfoils, the dashed box region in the loading settles without significant movement.

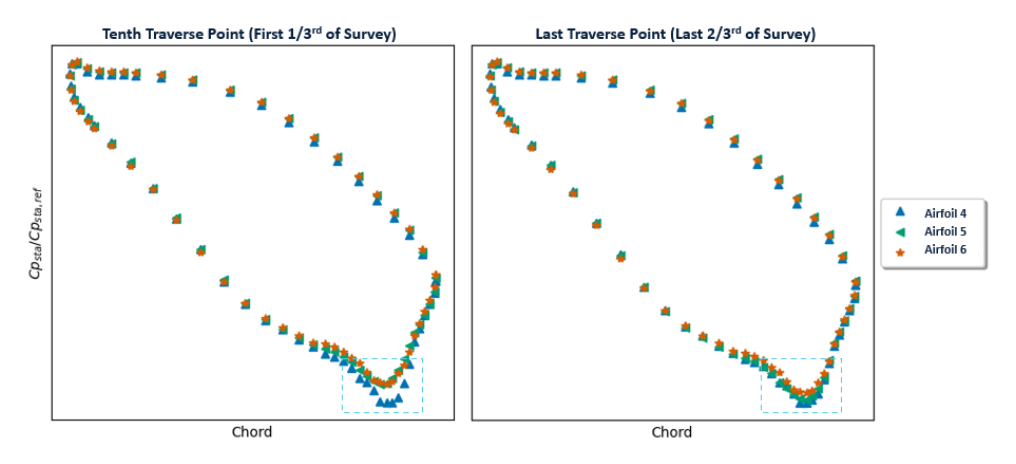


Figure 49: Loading Differences Caused by Traverse Bow Wave

MACH CORRECTION

When running at rig conditions where the Mach number is transonic, a discontinuity in the freestream region was observed in the downstream traverse wake data. Investigating the 5-hole probe data revealed that supersonic Mach numbers were reported out in the freestream region instead of the expected subsonic Mach numbers at the design pressure ratio condition. Similarly, certain sets of 5-hole probe data at the highest pressure ratio reported subsonic Mach numbers instead of expected supersonic Mach numbers in the freestream. The erroneous Mach number data was traced back to the 5-hole probe calibration. Exit isentropic Mach number is then calculated from static pressure and total pressure. A correction for Mach number is built into NASA's probe processing code. At these rig pressure ratios, regions of transonic flow exist in the traverse plane, causing the probe data correction to fluctuate between the calibration for supersonic and subsonic Mach numbers. In some cases, the incorrect calibration curve was used in initial postprocessing. Therefore, the Mach number in the freestream had to be corrected to match expected subsonic or supersonic exit flow conditions.

Isentropic relationships were used to calculate the expected exit isentropic Mach number and recalculate downstream $C_{p,total}$. The correction was only applied to the affected freestream region. At the design rig pressure ratio, outlier supersonic Mach numbers in the freestream were recalculated to subsonic to match an expected exit isentropic Mach number. At the highest rig pressure ratio, outlier subsonic Mach numbers in the freestream were recalculated to supersonic to match an expected exit isentropic Mach numbers. The correction resulted in a small addition or subtracted to the exit traverse total pressure, as determined by normal shock loss relations.

Figure 50 below shows the effect of the Mach number correction on the downstream wake profile. A discontinuity in the freestream region of the wake plot demonstrates a corresponding abrupt change in Mach number from the probe data. After correcting the Mach number, the freestream portion of the wake shows expected flat behavior. When correcting to a subsonic Mach number, the Mach number correction added to the average $C_{p,total}$ results. When correcting to a supersonic Mach number, the Mach number correction subtracted from the average $C_{p,total}$ results.

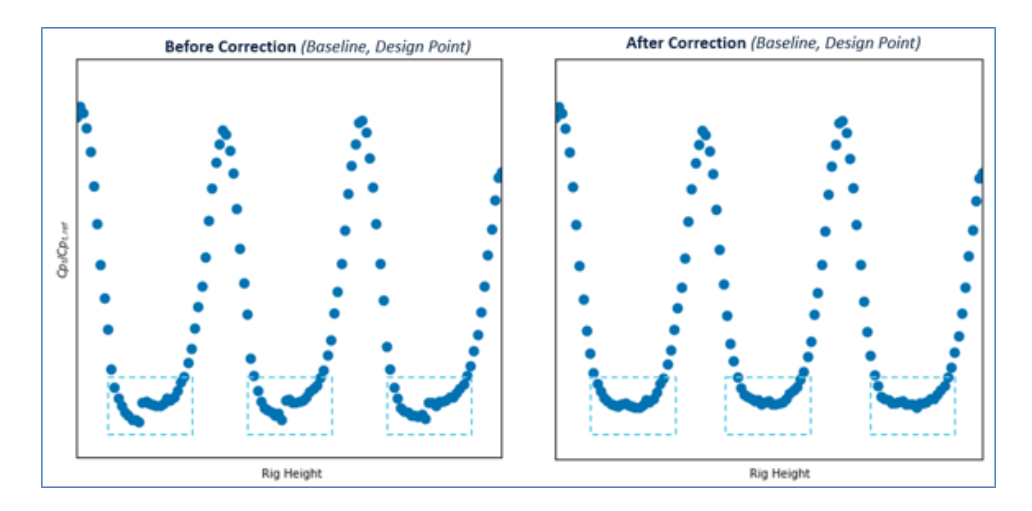


Figure 50: Traverse Data, with Freestream Region Highlighted

5.1.4 Uncooled Aerodynamic Data Summary

5.1.4.1 Design Point Performance

The downstream uncooled solidity data was assessed to understand differences in average loss, wake plots, and loading plots. Performance conclusions were formed at the aerodynamic design point. First, 1D average loss values were compared for the three solidities at the design point. Figure 51 demonstrates the performance of medium and low solidity measured as a change from the baseline solidity performance. Pre-test CFD predictions showed improved performance for both medium and low solidity from the baseline configuration. The test data showed a different trend. The test data demonstrated a small increase in loss for medium solidity and a small decrease in loss for low solidity. Post-test CFD, run at the as-tested conditions and geometry, demonstrates a similar trend to the test data. The post-test CFD setup will be described in more detail in Section 6.1. The difference in total pressure loss between the three solidities falls within measurement uncertainty. Statistically speaking, at the design point, there is no measurable difference between low, medium, and baseline solidity performance.

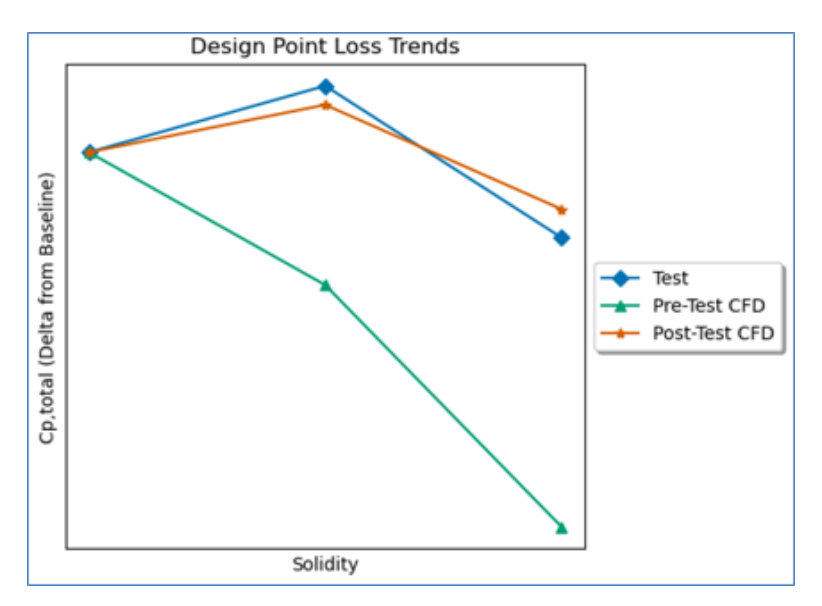


Figure 51: Design Point Trends, Uncooled Solidity Nozzles

The traverse data was examined at the design point to understand the trends seen in the average data. The wake data demonstrated periodicity. As shown in Figure 52, baseline solidity wakes showed the lowest peak magnitude of total pressure loss, while low solidity wakes showed the highest peak magnitude of total pressure loss. Medium solidity showed a peak magnitude comparable to low solidity and a wake width similar to the baseline solidity. The combination of a wider wake width and high peak magnitude of pressure loss corroborates the higher average loss for medium solidity at the design point. Pre-test and post-test CFD were both plotted against the test traverse data. As expected, the CFD overshot peak magnitude, and there were dips in the freestream that were nonphysical artifacts of the CFD modeling.

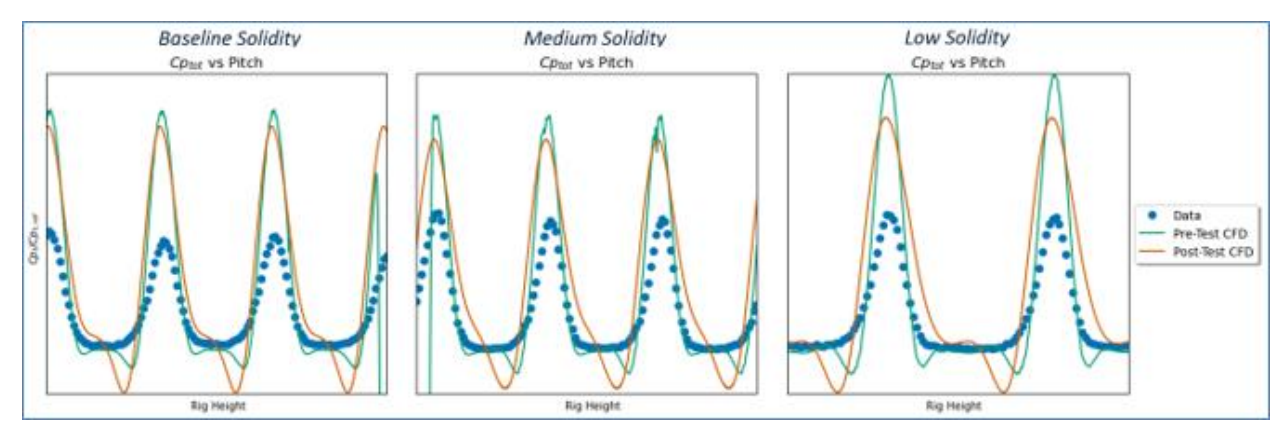


Figure 52: Design Point, Wake Plots

Airfoil loadings were also examined at the design point to understand the trends seen in the average data, as shown in Figure 53. Airfoil loadings of static pressure coefficient versus normalized axial chord were plotted for the three solidities. The three test articles (airfoils 4, 5, 6) were plotted, and the loadings were periodic for all three airfoils tested for each solidity. The leftmost point on the loading plot represents the surface static tap located at the nozzle leading edge, and the rightmost point represents the trailing edge static tap. Diffusion differences were noted between the three loadings: as solidity decreased, the minimum static pressure coefficient point occurred further upstream on the suction side. Post-test CFD accounting for as-tested conditions and as-produced hardware achieved a better match with the airfoil loadings than the pre-test CFD.

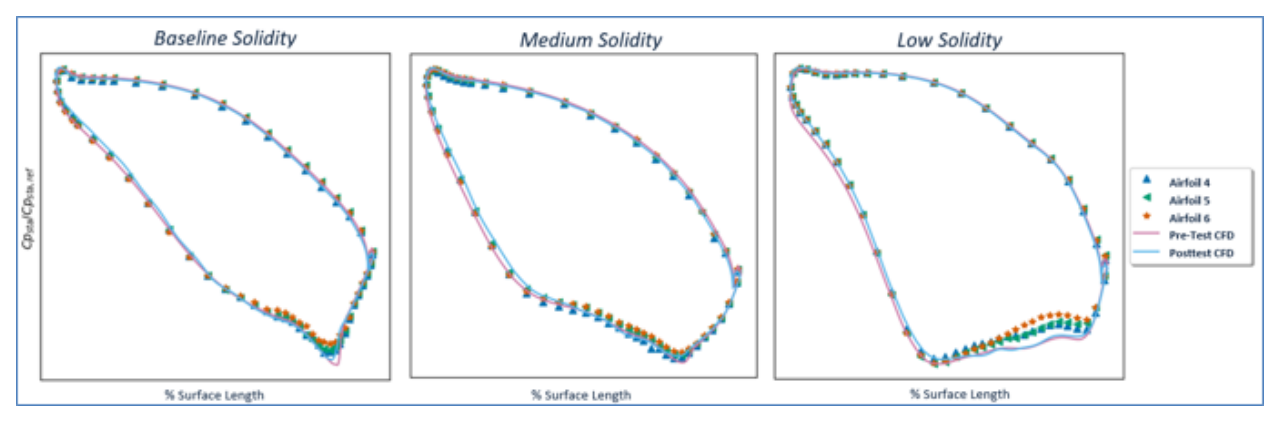


Figure 53: Design Point, Airfoil Loadings

Nozzle turning was assessed at the aerodynamic design point. The traverse probe uncertainty for exit swirl was given as $\pm 1.5^{\circ}$ [5]. Baseline and medium solidity showed nearly the same measured turning angle, as shown in Table 19. The exit swirl for low solidity was around 0.5° lower than baseline and medium solidity, which was within measurement uncertainty. Pre-test CFD and post-test CFD demonstrated similar magnitudes for turning for baseline and low solidity, although post-test CFD predicted a slightly higher turning angle for medium solidity. The difference between CFD and test measurements was within measurement uncertainty for all three solidity nozzles.

Table 19: Design Point Airfoil Turning, Delta from Pre-Test CFD

	Test Data	Pre-Test CFD	Post-Test CFD
Low Solidity	0	-1.5	0
Medium Solidity	0	-1	0.2
Baseline Solidity	0	-1	-0.1

5.1.4.2 Off-Design Performance & Derivatives

Average performance was also assessed at off-design points, examining the differences in average total pressure loss as incidence, pressure ratio, and Reynolds number changed.

REYNOLDS NUMBER DERIVATIVE

The average performance of the three solidities was assessed as Reynold's number increased and decreased from the design point Reynolds number as shown in Figure 54 and Figure 55. The impact of changing Reynold's number was assessed at three different rig pressure ratios at the lowest and design intent rig inlet angle.

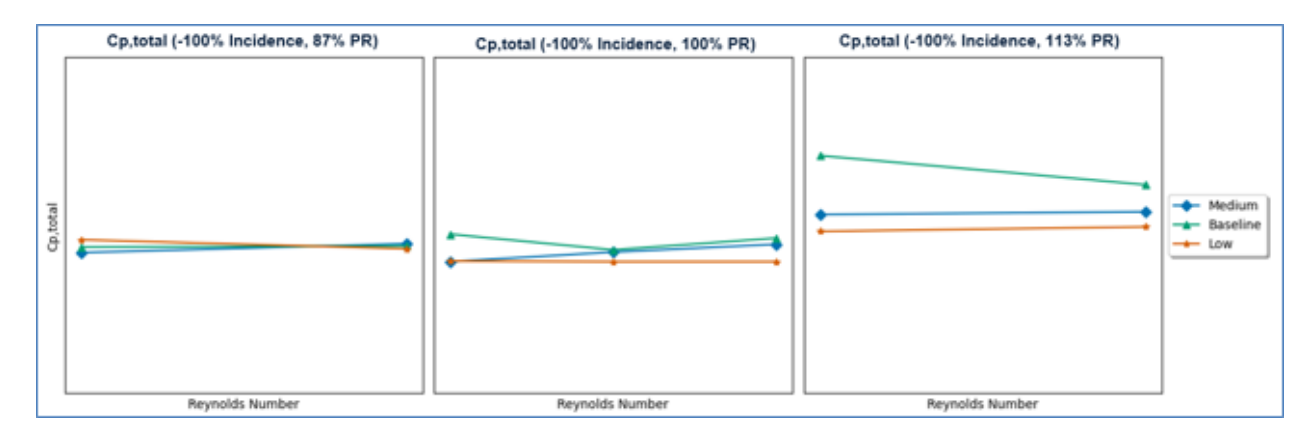


Figure 54: Reynolds Number Variation at Negative Incidence

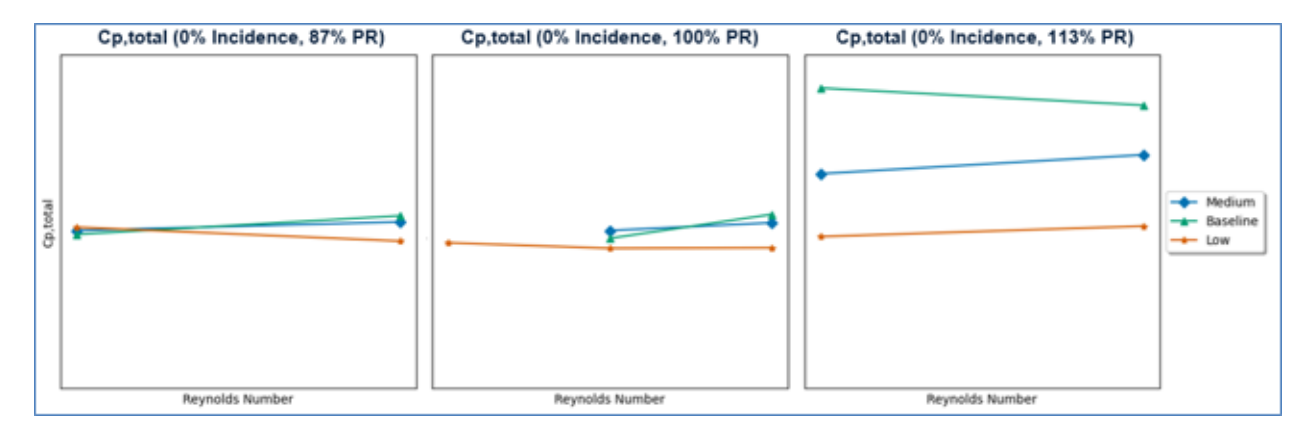


Figure 55: Reynolds Number Variation at Design Incidence

Generally, as Reynolds number increases there is only a small change in total pressure loss. At the lowest pressure ratio, baseline and medium solidity increase in loss and low solidity decreases in loss as Reynolds number increases. The same trend occurs at the design pressure ratio. At the highest pressure ratio, low and medium solidity increase in loss while baseline solidity decreases in loss as Reynolds number increases. The observed Reynolds number variation for each of the three solidities falls within measurement accuracy of exit total pressure. Generally, low solidity shows the lowest total pressure loss across Reynolds numbers at all three pressure ratios.

PRESSURE RATIO DERIVATIVE

The average performance of the three solidities was also assessed as rig pressure ratio increased and decreased from the design point. The impact of pressure ratio was assessed at the three rig Reynolds numbers at all three rig inlet angles, and the data is shown in Figure 56 through Figure 58.

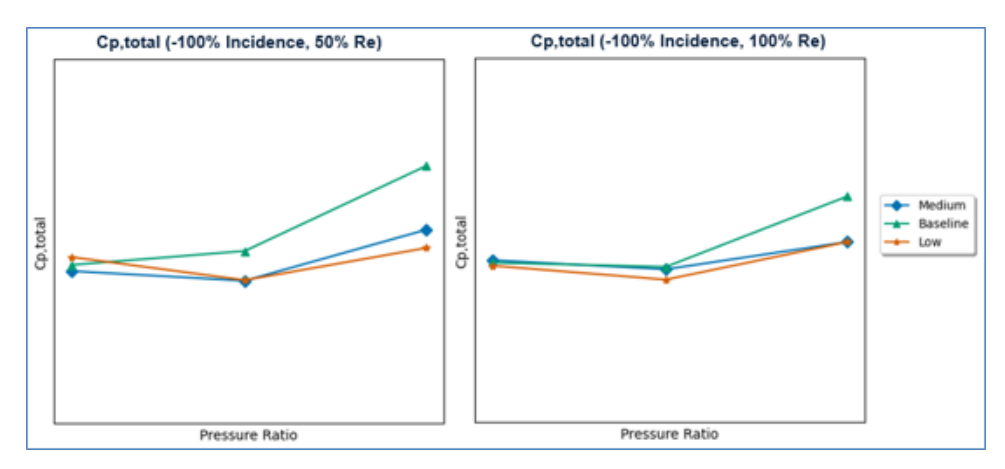


Figure 56: Pressure Ratio Variation at Negative Incidence

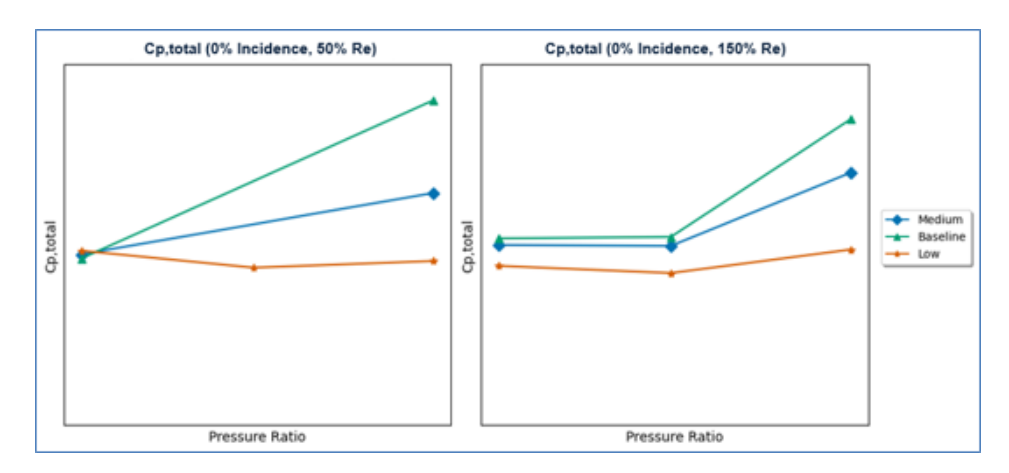


Figure 57: Pressure Ratio Variation at Design Incidence

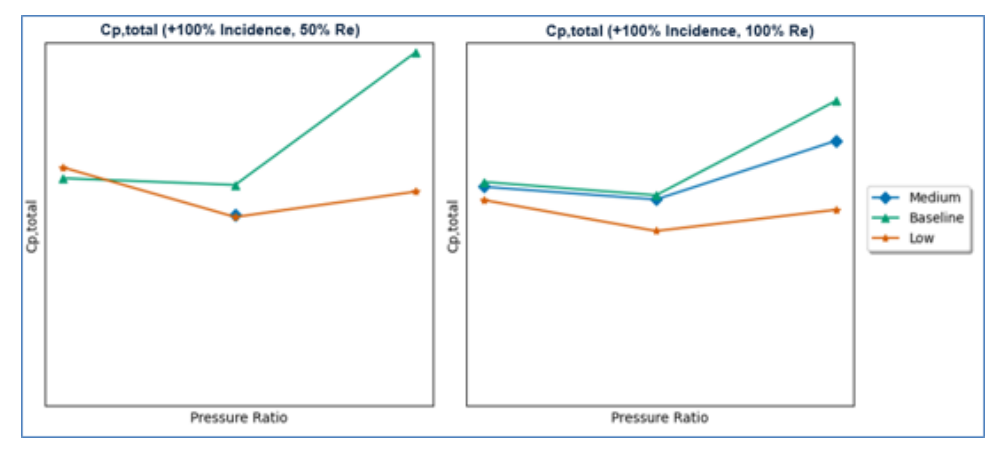


Figure 58: Pressure Ratio Variation at Positive Incidence

Generally, as overall rig pressure ratio increased, the average total pressure loss for the three solidities also increased. The increasing trend with pressure ratio matched expected behavior. The baseline solidity demonstrated a greater increase in total pressure loss as pressure ratio increases. Low solidity showed the

smallest total pressure loss increase as pressure ratio increased. The difference between baseline and low solidity were more obvious at the high pressure ratios and were greater than measurement uncertainty. Therefore, low solidity performed better across different pressure ratios than both baseline and medium solidity.

RIG INLET ANGLE DERIVATIVE

Lastly, the average performance of the three solidities was assessed as the rig inlet angle was varied in both positive and negative incidence directions from the design inlet angle. The impact of rig inlet angle was assessed at three Reynolds numbers at the design rig pressure ratio, with the results shown in Figure 59.

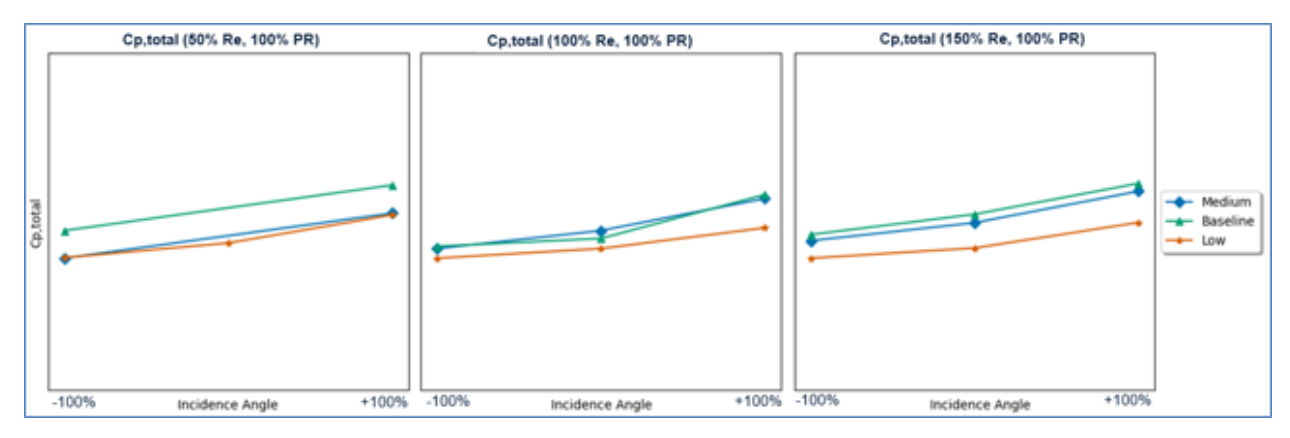


Figure 59: Inlet Angle Variation at Positive Incidence

Overall, total pressure loss increased as the rig inlet angle was increased. Low solidity showed the lowest overall total pressure loss at all three inlet angles. The three solidities performed closely at design Reynolds and pressure ratio at the three inlet angles, and loss differences became more pronounced at the highest Reynolds number. The difference between baseline and low solidities as inlet angle changed was greater than measurement uncertainty. Therefore, low solidity was more incidence tolerant at different operating conditions than baseline or medium solidity. Intuitively, the design angle would be expected to have the lowest loss. However, experience has shown that loss may continue to decrease as incidence becomes more negative until the boundary layer separates off the pressure side.

NO TURBULENCE

Traverse data for the low solidity blade at design point inlet angle was obtained using a clean inlet (no turbulence grid installed). A complete run was finished obtaining traverse data downstream of the linear cascade for this configuration, and the data was compared to data at 13% turbulence. Figure 60 shows the downstream wake with zero inlet turbulence. The wakes with no installed turbulence grid have sharper and cleaner peaks, while 13% turbulence wakes show lower magnitude peaks with a wider peak width. Adding freestream turbulence enhanced the wake mixing downstream, resulting in the observed wider, but shallower, wake profiles. Data with no turbulence was only taken at the design inlet angle with low solidity, so the data was not used in final performance calculations.

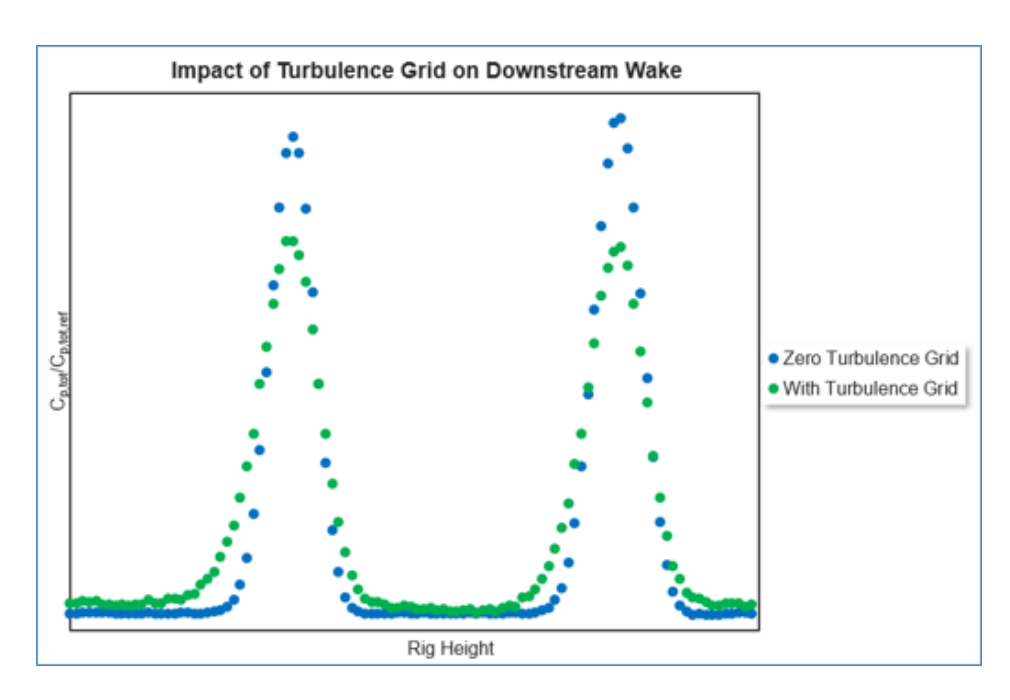


Figure 60: Traverse Wake Data for Zero Turbulence Run

5.1.5 Cooled Aerodynamic Data Summary

5.1.5.1 Design Point Performance

The cooled nozzle data was assessed to understand overall performance differences. Performance conclusions were formed at the aerodynamic design point. First, 1D average loss values were compared for the two cooled nozzles at the design point. Figure 61 shows the performance, measured as total pressure loss change from an all cooling holes closed configuration, of the cooled medium and low solidity nozzles. The greatest loss is induced when all the cooling holes are open on both solidities. As the cooling hole location moves more aft of the throat, average total pressure loss decreases: the forward cooling row shows the greatest total pressure loss, and the aft cooling row shows the least total pressure loss of the three cooling rows. The difference between the three individually open cooling holes was found to be within measurement uncertainty. Overall, the medium solidity cooled nozzle has greater average total pressure loss than the low solidity cooled nozzle.

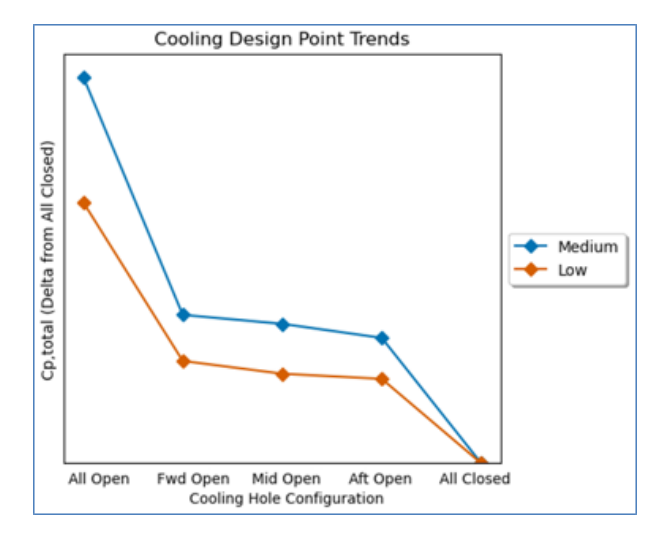


Figure 61: Design Point Trends, Cooled Solidity Nozzles

The traverse data (Figure 62) was examined at the design point to understand the trends seen in the average data. The wake data demonstrated periodicity, assessed by comparing the Cp_{Total} values calculated between individual wakes. Low solidity demonstrated both a narrower normalized wake width and smaller peak magnitude of total pressure loss than medium solidity when cooling was introduced. The difference in wake behavior supports the average data presented above. Post-test CFD matched the medium solidity cooled nozzle closely, aside from the freestream dip region which was a known nonphysical result of the CFD modeling. The post-test CFD matched the low solidity cooled nozzle less closely, overshooting the peak magnitude of total pressure loss with a wider wake width.

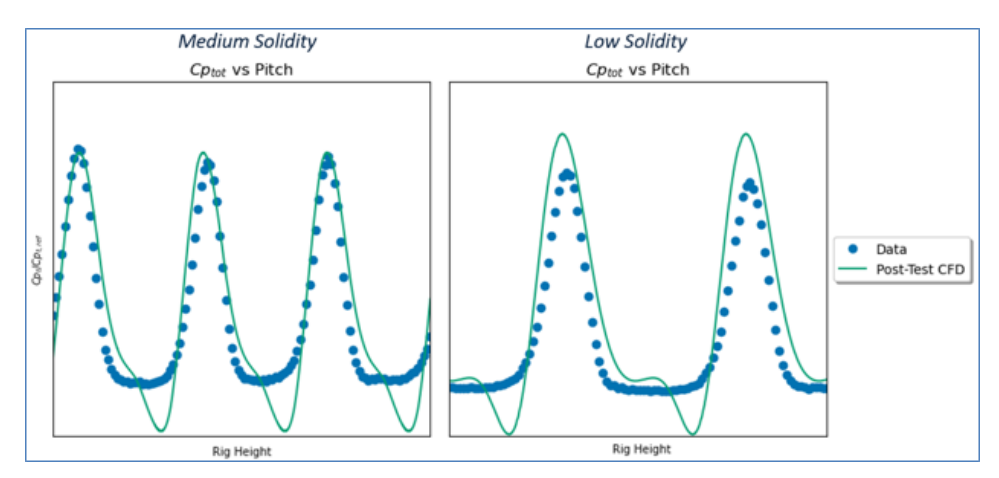


Figure 62: Design Point Wake Plots, All Holes Open

Airfoil loadings were also examined at the design point to understand the trends seen in the average data. Airfoil loadings of static pressure coefficient versus normalized axial chord were plotted for the two solidities. The three test articles (airfoils 4, 5, 6) were plotted, and the loadings were periodic for all three airfoils tested for each solidity. Refer to Figure 63 through Figure 66. The three coolant rows are visualized on the loading plot. The leftmost static tap of the three cooling taps is the forward row of cooling holes, the middle static tap is the middle row of cooling holes, and the rightmost static tap is the aft row of cooling holes on the loading plots. The post-test CFD deviated from the test data ahead of the coolant rows on the suction side for the medium solidity but matched the coolant row taps for the middle and aft rows. The post-test CFD for low solidity only matched the aft row cooling tap but matched the rest of the airfoil loading test data.

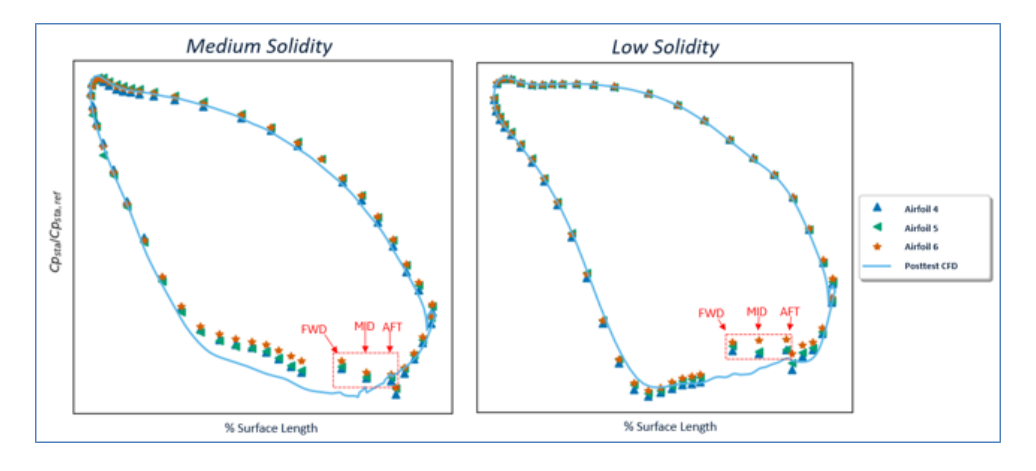


Figure 63: Design Point Airfoil Loadings, All Holes Open

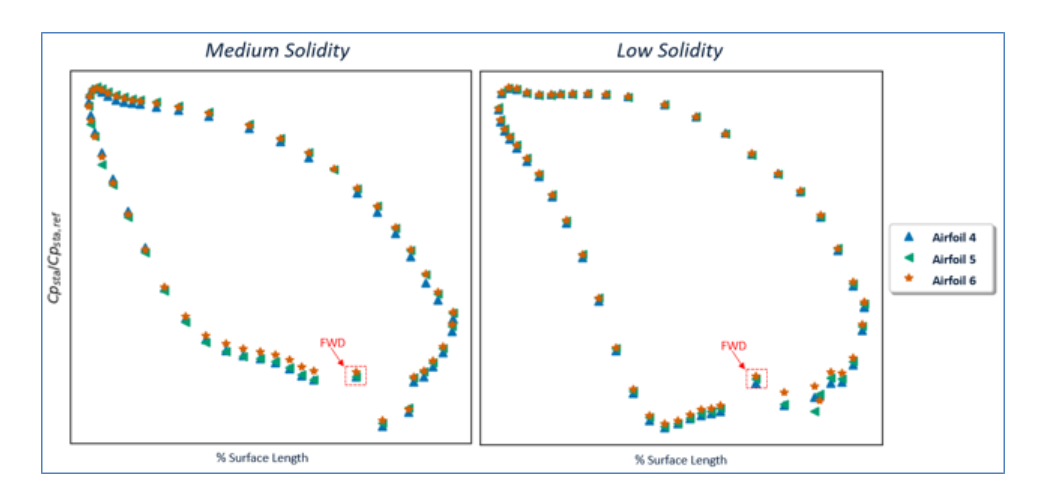


Figure 64: Design Point Airfoil Loadings, Forward Holes Open

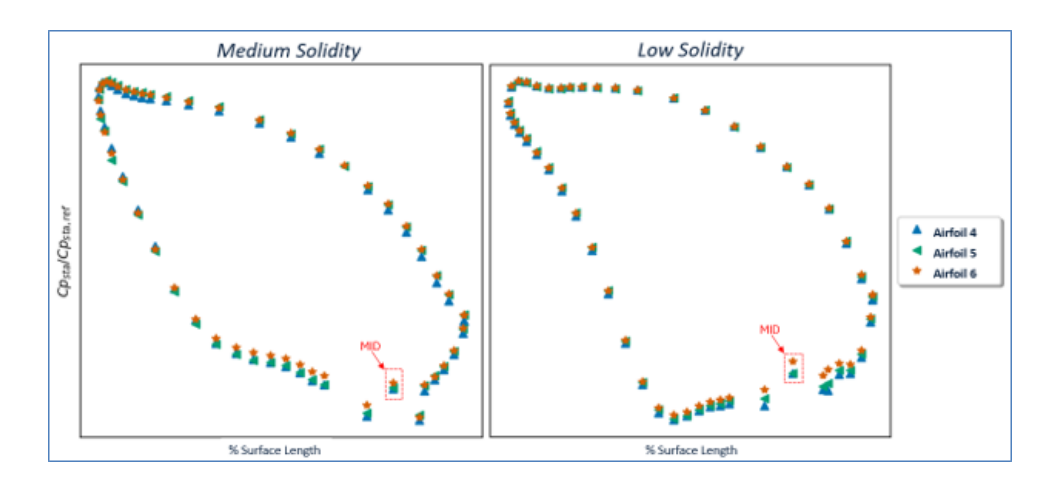


Figure 65: Design Point Airfoil Loadings, Middle Holes Open

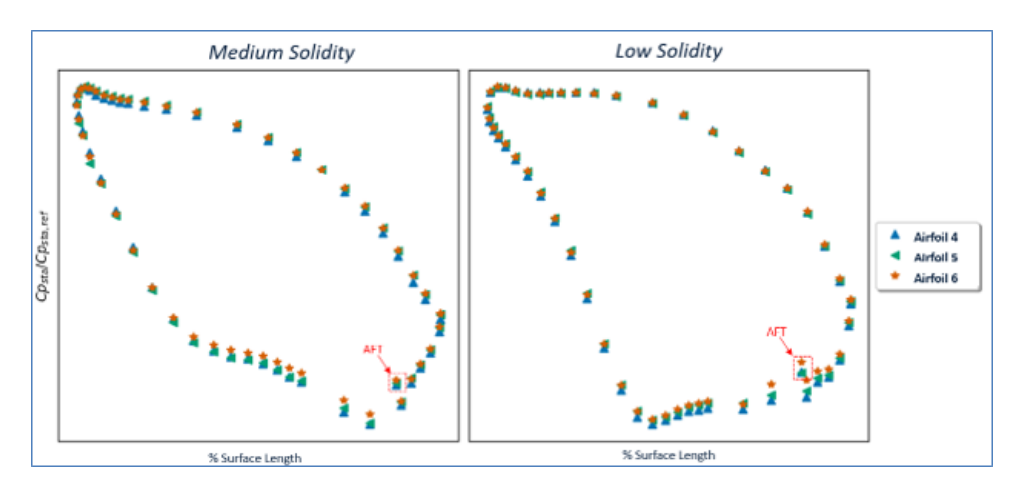


Figure 66: Design Point Airfoil Loadings, Aft Holes Open

When each individual row of coolant was open, the location on the loading plot showed a maximum in the coefficient of static pressure, or minimum in Mach number. The local maximum in $C_{p,static}$ (and minimum in Mach number) on the loading plots results from the slower-moving coolant flow meeting the exterior nozzle surface from the individual cooling rows. When only the forward row was open, the middle and aft

rows still showed increased static pressure due to the film traveling along the suction surface past those rows. Similarly, when only the middle row was open, the aft row showed an increased static pressure from the injected coolant traveling past the aft row. Only with the aft row loading was there a reduced effect on the upstream cooling rows since there was no film at those locations. Therefore, the coolant from the forward row impacted the static pressure to a greater extent on the suction surface than the impact of the aft row, incurring more loss. Introducing coolant will interrupt and slow the flow on the nozzle surface.

The low solidity nozzle showed the minimum static pressure coefficient forward of the first row of cooling holes. Low solidity coolant was injected aft of this high Mach peak, so the coolant was injected into a diffusing flow-field. On the other hand, the medium solidity nozzle showed minimum static pressure coefficient aft of the cooling holes on the suction side, corresponding to a higher peak Mach number towards the trailing edge. Medium solidity coolant was injected near the Mach number peak. Therefore, coolant on the medium solidity suction side entered in an accelerating flow-field. The difference in coolant injection location on the loading plot likely contributed to the differences in loss seen from cooling both solidities.

Nozzle turning was assessed at the aerodynamic design point as shown in Table 20. The traverse probe uncertainty for exit swirl was given as $\pm 1.5^{\circ}$ [5]. The turning measured for each hole configuration within both low and medium solidity was within measurement uncertainty. The turning difference between low and medium solidity was also within measurement uncertainty. Therefore, the same turning exit angle was measured for both solidity nozzles for all hole configurations.

Hole Configuration	All Holes Open	Fwd Open	Mid Open	Aft Open	All Closed
Low Solidity	-0.2	0	-0.1	-0.1	0
Medium Solidity	0.1	-0.1	-0.1	0.1	0

Table 20: Cooled Design Point Airfoil Turning, Delta from Uncooled

Repeat points were obtained for the two solidities at the cooling design point for all cooling configurations. All calculated standard deviations of the average total pressure coefficient for the repeat points were found to be within the pressure measurement uncertainty of the facility. The percent difference between the repeat points for each configuration was within uncertainty between repeat points. Figure 67 demonstrates the repeatability of the cooled nozzle data.

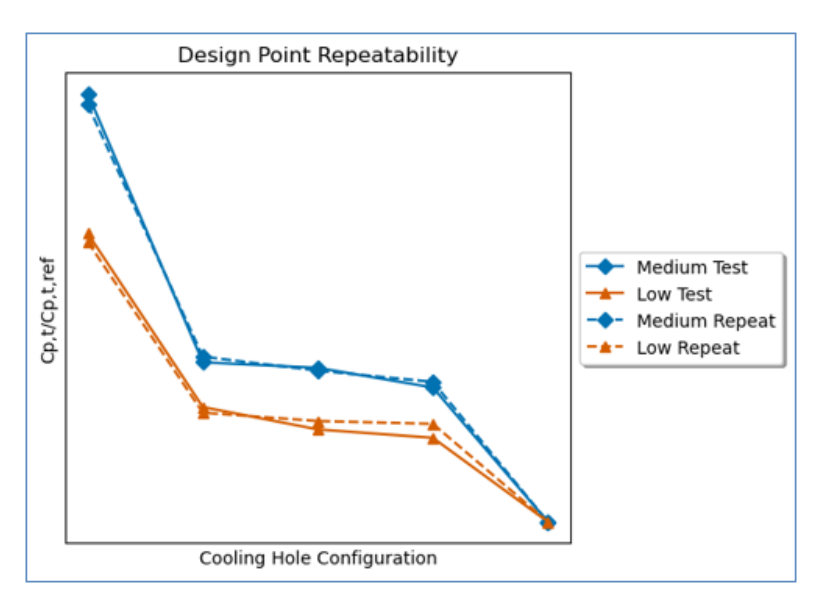


Figure 67: Cooling Design Point Repeatability

5.1.5.2 Off-Design Performance & Derivatives

The performance of the low solidity cooled nozzle was assessed as the coolant pressure ratio increased at the design point rig conditions. As seen in Figure 68, higher total pressure loss was measured when all coolant rows were open. The three individual coolant rows showed similar total pressure loss averages. The forward row induced the highest total pressure loss. The middle and aft rows showed similar average loss within measurement uncertainty. A check was performed to see if the superposition of individual cooling rows summed to the total pressure loss measured when all rows were open. It was observed that the average loss for each individual row did not add up to the total loss incurred when all rows are open. Instead, an initial loss debit occurred when inserting coolant from any row location, with another loss debit caused by all three rows being open. Overall, there was not a well-defined relationship between average loss and coolant pressure ratio; individual rows showed only a slight increase in average loss as pressure ratio increased, and when all the holes were open, the highest average loss occurred at the design pressure ratio of 1.6. Higher velocity coolant injection into the boundary layer at higher coolant pressure ratios than design energized the boundary layer, resulting in the lower overall loss observed.

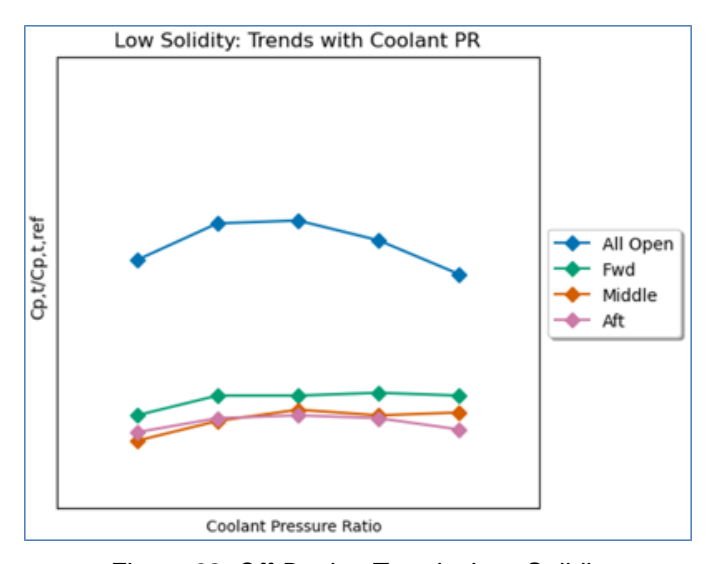


Figure 68: Off-Design Trends, Low Solidity

The wake plots for the lowest and highest coolant pressure ratios were examined to observe differences as coolant pressure ratio increased. As shown in Figure 69, the wake differences between the lowest and highest coolant pressure ratio were minimal, with only a slight peak magnitude increase within measurement uncertainty at higher coolant pressure ratios.

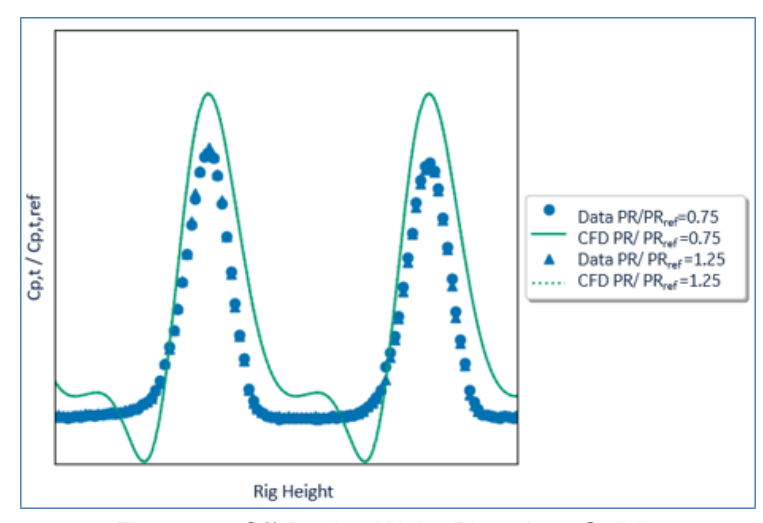


Figure 69: Off-Design Wake Plots, Low Solidity

Generally, as the coolant pressure increased, there was a slight increase in static pressure coefficient on the nozzle surface as shown in Figure 70. As more coolant flow was injected into the exterior boundary layer, there was greater interruption to the main flow and a slight increase in boundary layer thickness, leading to lower external Mach numbers.

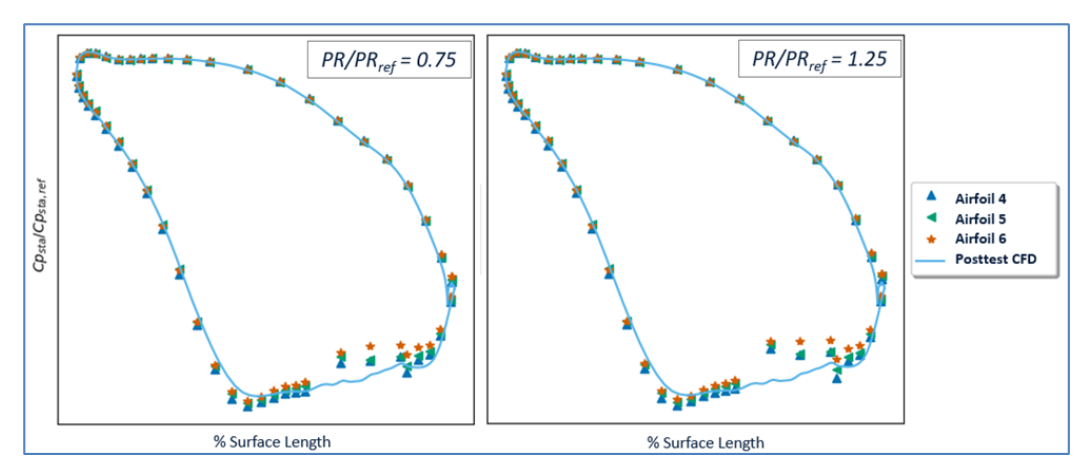


Figure 70: Off-Design Loadings, Low Solidity, All Holes Open

Compared with the low solidity trends and shown in Figure 71, the medium solidity configuration was observed to have higher loss on average. Medium solidity demonstrated a more defined relationship between coolant pressure ratio and total pressure loss: as pressure ratio increased, the loss incurred by individual cooling rows also increased. When all cooling rows were open, peak average loss was observed at the design pressure ratio. At lower pressure ratios, less coolant flow interrupts the main flow path, resulting in lower loss. At the high pressure ratios, the coolant flow velocity better matches the main flow velocity and will incur lower mixing losses. However, at the design pressure ratio, the cooling flow sufficiently interrupts the main rig flow while not quite matching rig flow velocities to induce the highest mixing loss. For medium solidity, the forward row of coolant caused the highest average mixing loss due to the higher mainstream velocity, while the aft row caused the least average loss.

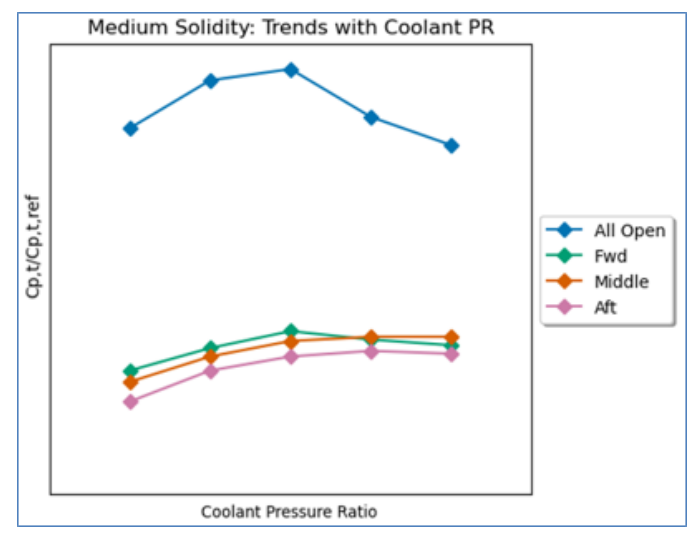


Figure 71: Off-Design Trends, Medium Solidity

Similar to the low solidity cooled nozzle, the wake plots for the lowest and highest coolant pressure ratios were examined. Shown in Figure 72, the wake differences between the lowest and highest coolant pressure ratio were minimal, with small changes within measurement uncertainty between coolant pressure ratios.

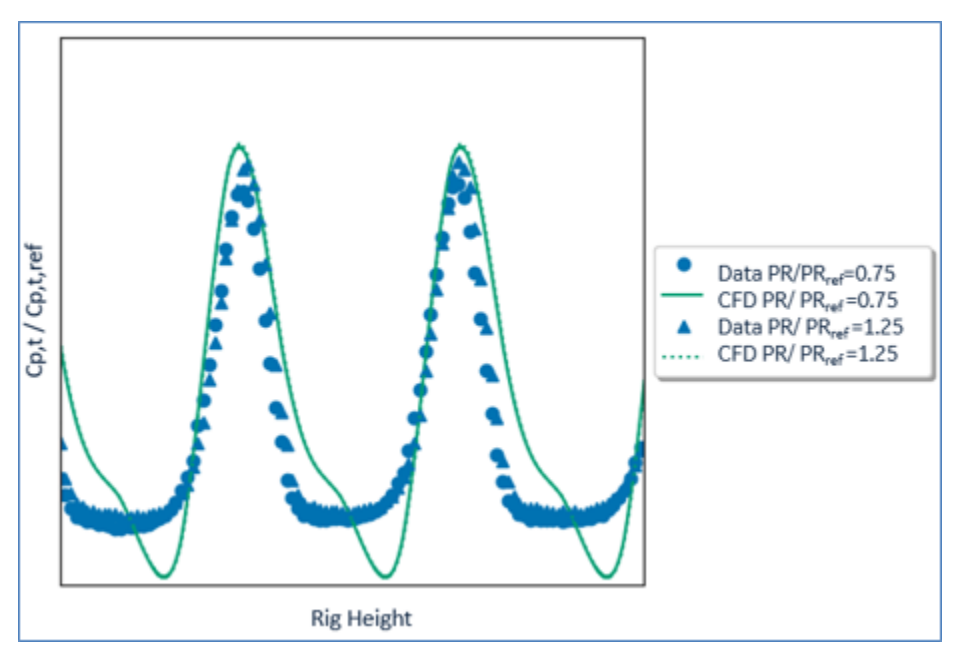


Figure 72: Off-Design Wake Plots, Medium Solidity

As coolant pressure ratio increased, the surface static pressure coefficient increased, signifying a decrease in external Mach number, as shown in Figure 73. Increasing coolant pressure ratio increased the amount of flow injected onto the suction surface, thereby decreasing the external Mach number. The magnitude of static pressure coefficient increases from low to high coolant pressure ratio was noted to be larger for medium solidity than low solidity.

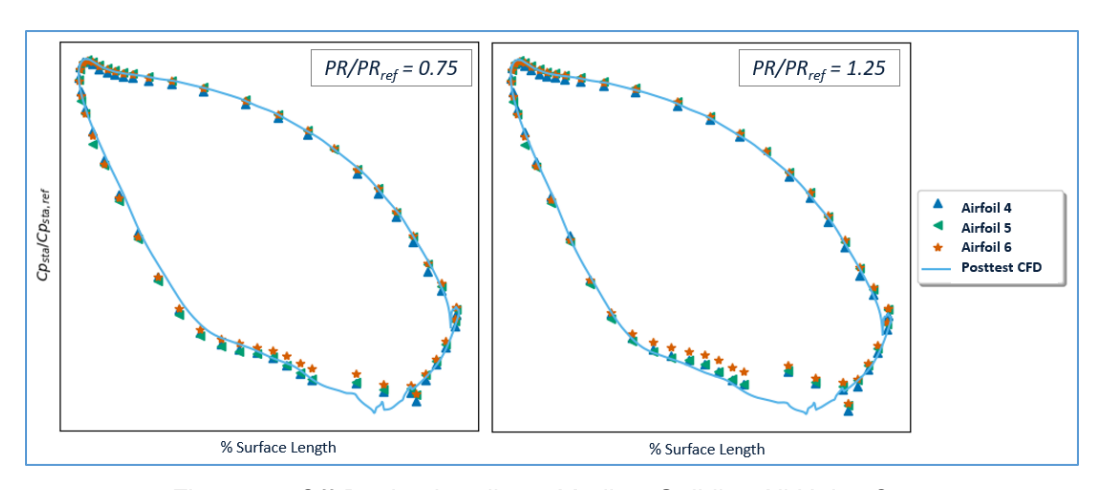


Figure 73: Off-Design Loadings, Medium Solidity, All Holes Open

5.1.5.3 Background Oriented Schlieren

The BOS technique captured multiple frames that were combined to a single average image in post-processing. The resulting average images display the average magnitude density gradient observed in the data over the image acquisition period. The density gradient scale reveals the magnitude of density gradient change measured from the reference image. The reference image was obtained when no coolant holes were flowing. The maximum side of the scale (colored red) indicates the largest magnitude of density gradient change from the reference. Since the BOS images display the absolute value of density gradient, the directions of density gradient are not represented. The center of the tailed streaks of density gradient

demonstrates the region of maximum density gradient (Figure 74). Both sides of the tailed streaks of density gradient represent changes to density gradient in different directions.

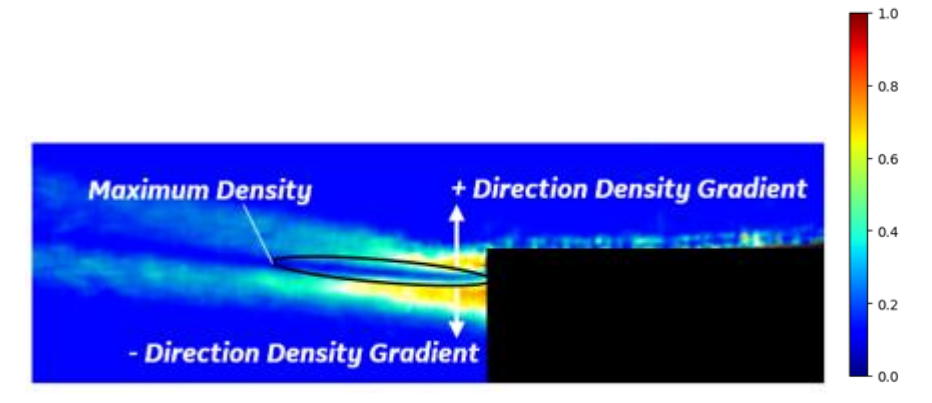


Figure 74: Magnitude of Density Gradient Diagram

Gradients were seen in the BOS images at the three cooling hole row injection locations. Carbon dioxide cooling flow introduces slower flow and cooler flow temperatures to the main flow when injected, causing an observed change in the density gradient.

In the processed BOS images, a strong density gradient region around the edge of the profile was evident. This strong region was attributed to noise in the post-processed image. In the reference image, some blurriness around the vane edge resulted from camera resolution of the background and vane. Additionally, deflection of the Plexiglass sidewall and the vane under vacuum during testing contributed to noise in the post-processed image at the edge of the vane.

DESIGN POINT IMAGES

Figure 75 shows the BOS results for low and medium solidity cooled nozzles at the aerodynamic design point when all cooling rows were open. On the suction side of the nozzle, the density gradient magnitude represents the buildup of film caused by post throat cooling. Compared to low solidity, the medium solidity nozzle shows a thicker film layer and a larger magnitude of density gradient in the film layer. The trailing edge wake behavior between the two solidities is similar. At the cooling hole injection sites, medium solidity shows a larger density gradient caused by the coolant. Overall, the larger density gradient magnitudes for medium solidity corroborate the greater total pressure losses of the cooled medium solidity nozzle.

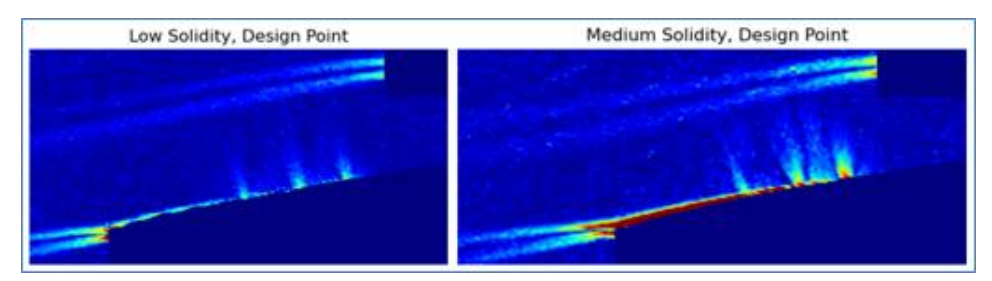


Figure 75: BOS Results at Aerodynamic Design Point

REYNOLDS NUMBER DERIVATIVE

Figure 76 shows the variation with cascade Reynolds number for the low solidity cooled nozzle. As Reynolds number increases, holding exit isentropic Mach number and coolant pressure ratio constant, the magnitude of density gradient increases. At higher Reynolds numbers, the density of the main flow is higher, which allows for capture of more details in the main flow induced by the presence of cooling due to the larger density differences in these features.

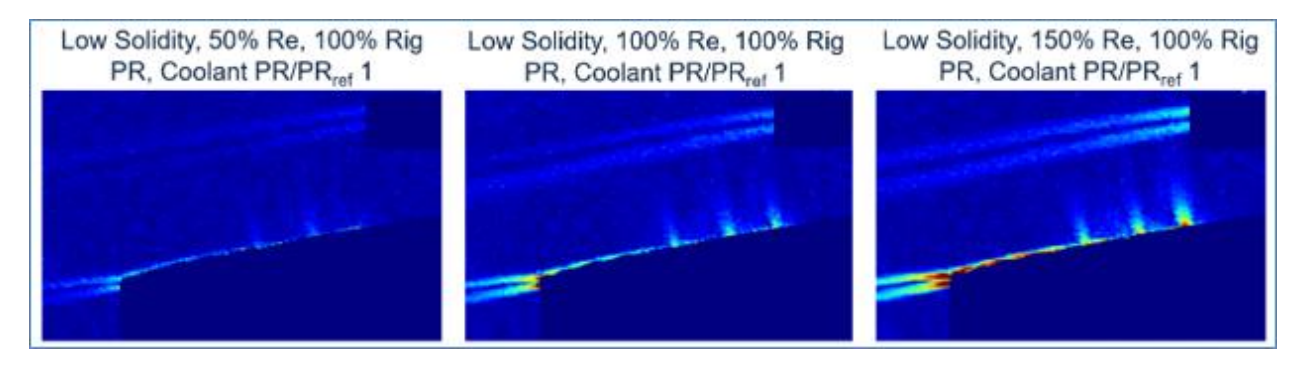


Figure 76: BOS Reynolds Variation for Low Solidity Cooled Nozzle

Similarly, Figure 77 shows the variation with Reynolds number for the medium solidity cooled nozzle. The medium solidity cooled nozzle follows the same trend as the low solidity cooled nozzle. As Reynolds number increases, magnitude of density gradient increases in the trailing edge wake, in the film cooling layer, and at the site of coolant injection.

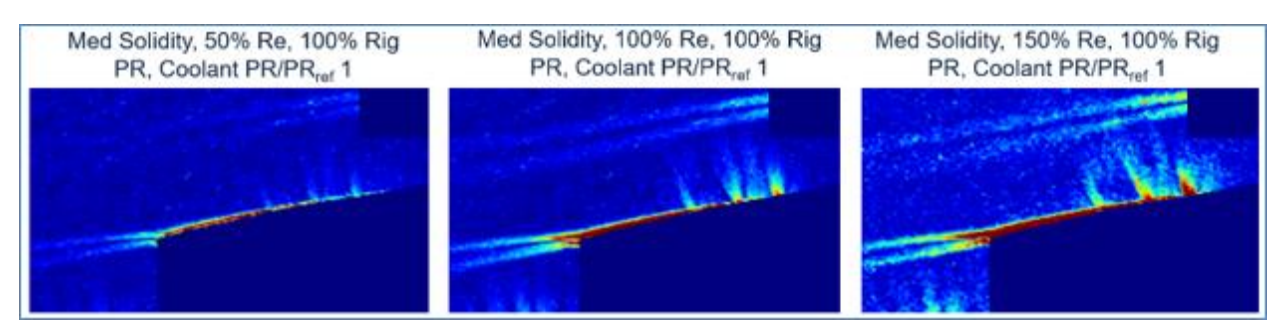


Figure 77: BOS Reynolds Variation for Medium Solidity Cooled Nozzle

CASCADE PRESSURE RATIO DERIVATIVE

Figure 78 shows the variation with cascade pressure ratio, or exit isentropic Mach number, for the low solidity cooled nozzle. As Mach number increases, keeping Reynolds number and coolant pressure ratio constant, the film layer thickness and film layer density gradient magnitude decreases. Higher velocity main rig flow reduces the extent to which the film layer can grow on the aft suction side of the nozzle. Additionally, higher Mach number causes greater magnitude of density gradients at the three coolant film rows. The slow velocity coolant interrupts the higher velocity main airflow at the injection sites, inducing a density change to the main airflow. A density gradient aft of the cooling holes indicates coolant-induced shock formation at the highest exit isentropic Mach number.

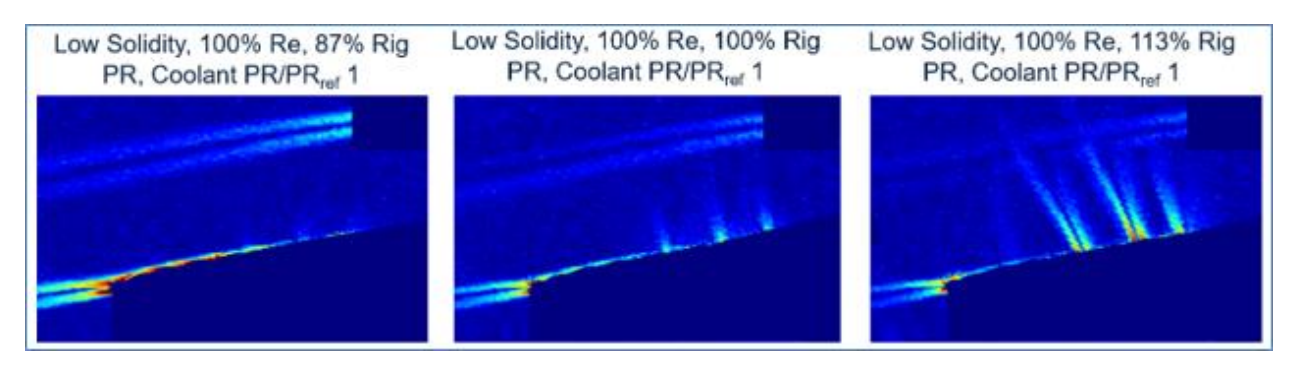


Figure 78: BOS Cascade Pressure Ratio Variation for Low Solidity Cooled Nozzle

Similarly, Figure 79 shows the variation with cascade Mach number for the medium solidity cooled nozzle. The medium solidity cooled nozzles follows the same trends as the low solidity cooled nozzle. As Mach number increases, the film layer thickness decreases aft of the coolant injection sites. The strength of the trailing edge wake caused by the film also decreases. The higher the Mach number, the stronger the density gradient in the main airflow at the three cooling row locations. Shock formation at the highest exit isentropic Mach number is also evident on the suction side of the medium solidity cooled nozzle.

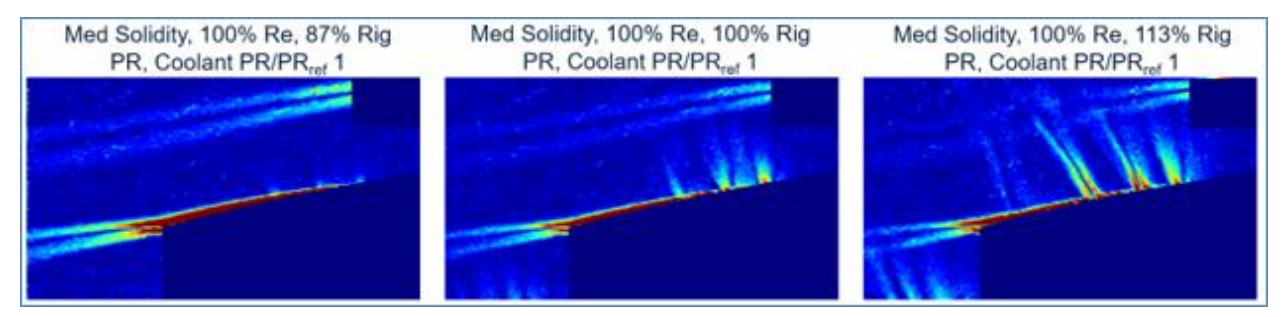


Figure 79: BOS Cascade Pressure Ratio Variation for Medium Solidity Cooled Nozzle

COOLANT PRESSURE RATIO DERIVATIVE

Figure 80 shows the variation with cooling hole pressure ratio for the low solidity cooled nozzle. The coolant pressure ratio is directly related to coolant blowing ratio, and as coolant pressure ratio increases the flow rate of injected coolant also increases. As coolant pressure ratio increases, keeping rig Reynolds number and rig pressure ratio constant, the magnitude of density gradient caused by cooling increases everywhere on the nozzle. The film layer thickness, the film layer density gradient magnitude, trailing edge wake density gradient magnitude, and density gradient at the cooling hole injection sites all increase as coolant pressure ratio increase. This trend follows expected behavior. No film lift-off was observed, even at the highest coolant pressure ratio.

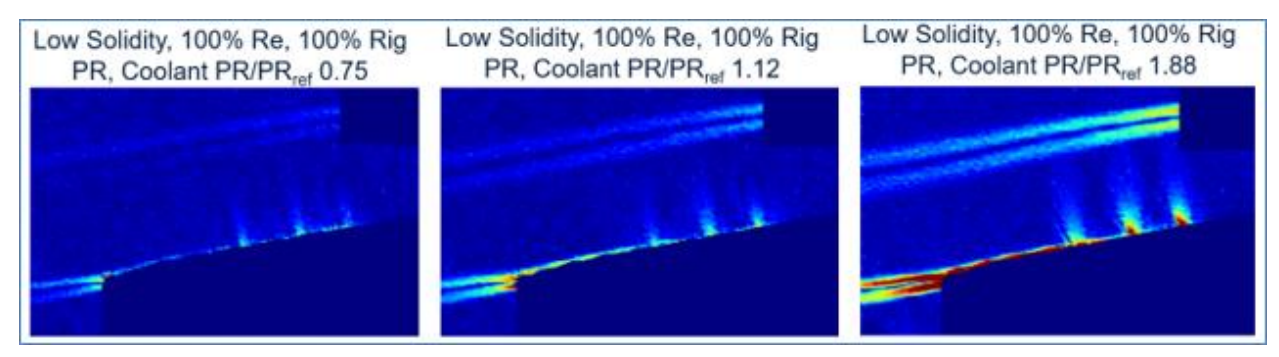


Figure 80: BOS Coolant Pressure Ratio Variation for Low Solidity Cooled Nozzle

Similarly, Figure 81 shows the variation with coolant pressure ratio for the medium solidity cooled nozzle. As coolant pressure ratio increases, the magnitude of density gradient increases for the coolant behavior on the nozzle. No film lift-off was observed for the medium solidity nozzle.

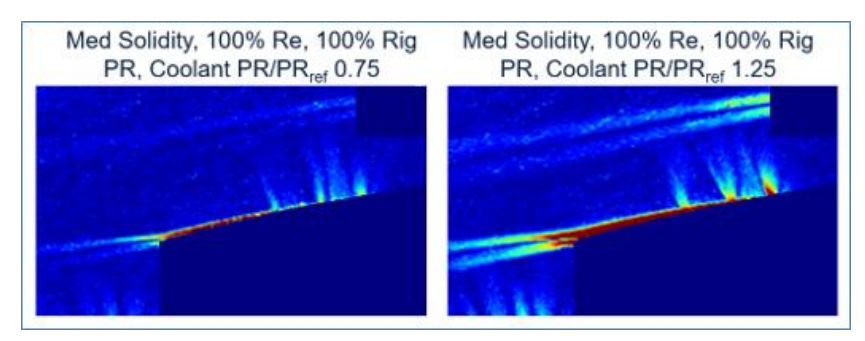


Figure 81: BOS Coolant Pressure Ratio Variation for Medium Solidity Cooled Nozzle

5.1.6 Aerodynamic Design Validation

5.1.6.1 Prediction Models, Uncooled

Pre-test RANS CFD was performed for the three solidities. This CFD was run using GEA best practices and anticipated flow boundary conditions in CW22. Geometries were run at their nominal condition. All runs were made using a k-omega turbulence model using documented inlet turbulence conditions for the rig.

After completing the test matrix, post-test CFD was run to achieve a better match with test data. The domain grid was structured with 13 million cells for all three solidities. The distance from the nozzle leading edge to the domain inlet was set to the same distance from the nozzle leading edge to the inlet traverse plane. Similarly, the distance from the nozzle trailing edge to the domain exit was set to the same distance from the nozzle trailing edge to the exit traverse plane.

The test conditions were utilized to run multiple RANS CFD cases for selected cases in the test matrix. Total inlet pressure, total inlet temperature, and exit static pressure from the test were used as average boundary conditions for the CFD.

The following figures show the comparison between test data, pre-test CFD, and post-test CFD for off-design conditions. The $C_{p,total}$ for low and medium solidity was measured as a delta from the baseline solidity performance.

Post-test CFD was compared with test data and pre-test CFD at the three rig inlet angles and design pressure ratio, shown in Figure 82. At the design angle, the post-test CFD matched overall trends between the three solidities seen in the test data. At medium and high Reynolds numbers, the post-test CFD matched the average loss comparison between the three solidities at those points. The pre-test CFD did not match the comparison of loss between the three solidities: at medium Reynolds number, low solidity shows the greatest average loss, while the test data shows the least average loss. As Reynolds number increased, the post-test CFD captured the decrease in loss seen with low solidity, but it did not capture the increase in loss measured by the test for baseline and medium solidity. Generally, the post-test CFD achieved a better match to test data trends than the pre-test CFD.

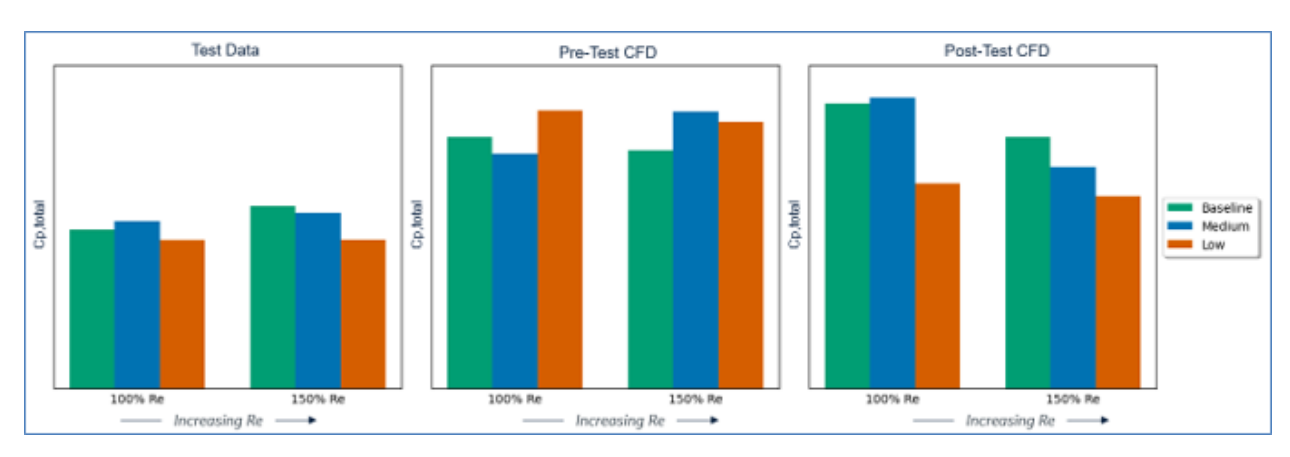


Figure 82: Comparison to CFD, Reynolds Number Variation

Post-test CFD was also compared with test data and pre-test CFD at two cascade Reynolds numbers and the design rig inlet angle to assess data variation with cascade pressure ratio, shown in Figure 83. Both pre-test CFD and post-test CFD captured the increase in loss as PR increased for all three solidities. However, the pre-test CFD better matched the comparative average loss between the three solidities at each individual cascade pressure ratio.

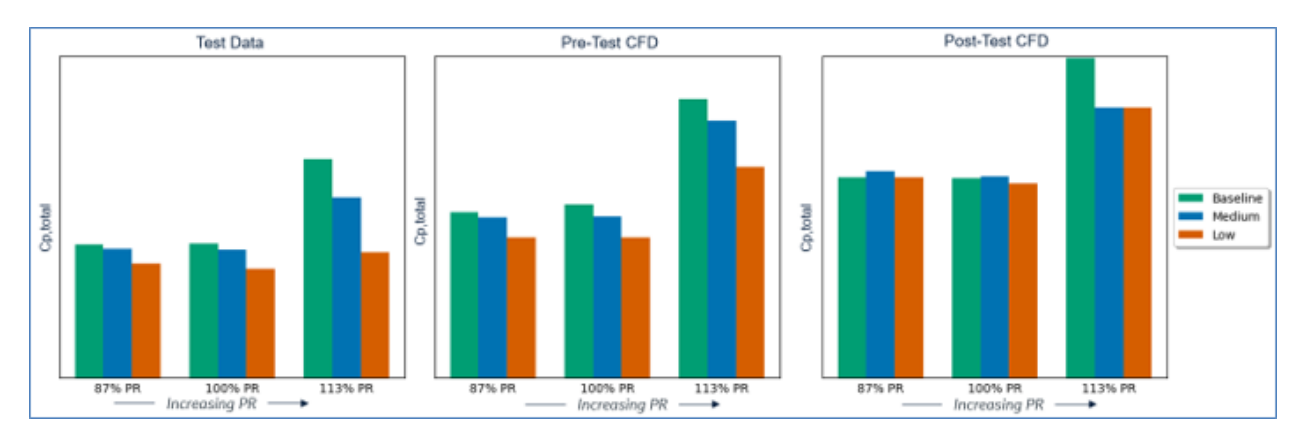


Figure 83: Comparison to CFD, Overall Pressure Ratio Variation

Lastly, post-test CFD was compared with test data and pre-test CFD at three cascade Reynolds numbers and the design rig pressure ratio to assess data variation with inlet angle, shown in Figure 84. As the inlet angle increased, the overall loss for all three solidities increased in the test data. While the pre-test CFD did not capture this trend with inlet angle, the post-test CFD better reflected the increase in average loss with increasing inlet angle. However, the pre-test CFD best matched the comparative average loss between the three solidities at each inlet angle point. Across inlet angle test points, low solidity demonstrated the lowest average loss.

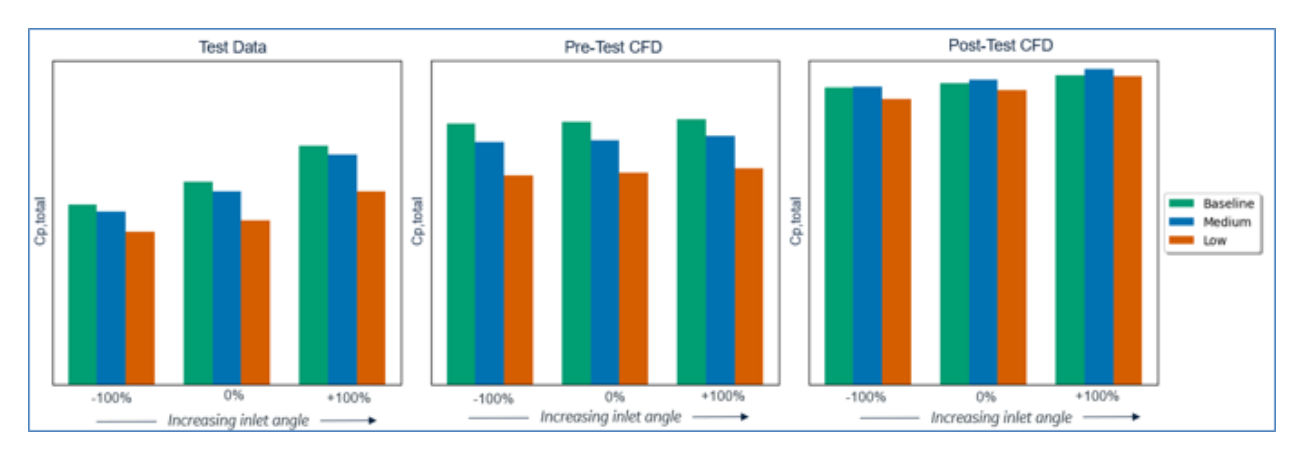


Figure 84: Comparison to CFD, Inlet Angle Variation

Overall, the post-test CFD achieved a closer match to most test data than the pre-test CFD. Inlet profiles for boundary conditions, improved accuracy of hardware geometric measurements for the domain, turbulence levels, and transition model assumptions could all be tuned to the test data to achieve an even closer match in future work.

5.1.6.2 Prediction Models, Cooled

Pre-test CFD was not run for the cooled nozzle test cases. Post-test RANS CFD with a k-omega turbulence model was run for select cooled nozzle cases. The domains were the same as the uncooled cases, but coolant was added to the CFD domain. The coolant footprints were mapped to the geometry surface using coordinate points at the four corners of each hole, and coolant conditions were applied as source terms. Boundary conditions for the coolant were set to match the reported test coolant conditions. Total inlet pressure, total inlet temperature, and exit static pressure from the test were used as average boundary conditions for the CFD.

Table 21 shows the results from running post-test CFD with medium and low solidity cooled nozzles. The post-test CFD was averaged in a similar manner to the test data, using area-averaging. The post-test CFD

matches overall trends at the cooling design point: medium solidity demonstrates a larger loss detriment from post-throat cooling than low solidity. While the post-test CFD best approximates the trends between solidities, the post-test CFD overestimates the total pressure loss associated with both solidities. Additionally, the test shows a larger difference between cooled solidities than the CFD. An improved turbulence model may address the low solidity behavior in the CFD in future work.

Table 21: Comparison to CFD with Post-Throat Cooling

Average Cpt (All Holes Open, Design PR)	% Difference (Low-Medium Solidity)
Test (Area-Average)	-28%
Test (Mass-Average)	-27%
Test (Mixed Average)	-27%
Post-Test CFD (Area-Average)	-5%

5.1.7 Cascade Test Results Conclusion

All test objectives were achieved for the CW22 S2N Linear Cascade test. Data was successfully acquired and assessed for the uncooled solidity and the post-throat cooling objectives of the test. Appropriate steps were taken to validate the cascade setup, data acquisition, and data results to give confidence to the final data. Key findings were noted throughout, along with lessons learned. Performance at the aerodynamic design point and off-design points was assessed and compared against CFD simulations.

5.1.7.1 Performance Conclusions

The performance results from the S2N Linear Cascade were used to determine overall progress towards technology maturation. Two components of the test were assessed to inform NASA TPMs:

- (1) Low Solidity Optimized Airfoil: optimize airfoil design for solidity
- (2) Compact Core Stage 2 Nozzle: reduced mixing losses downstream of throat

Each component of the test was assessed to anticipated technology maturation levels by comparing total pressure loss, measured as C_{p,total}. Table 22 below shows the total pressure loss measured for both components of the test with the improvement in profile loss from the technologies also shown. The change in total required cooling flow for low solidity vanes does not factor into the fuel burn estimate shown below.

Table 22: Performance Results for TPM Estimates

Technology	Tested	C _{p,total} [% improvement]
(1) Low Solidity Optimized Airfoil	Profile Loss Difference	7
(2) Commant Comp C2N	Low Sol Profile Loss Difference	34
(2) Compact Core S2N	Med Sol Profile Loss Difference	39

For this test, only differences in two-dimensional airfoil profile were considered to impact losses. Based on the results shown above, the profile losses tracked as expected for both components of the test. At the design point, there was no measurable difference between low, medium, and baseline solidity performance. Additionally, eliminating post-throat cooling showed an added benefit with decreased profile loss.

Despite changes to schedule, testing was successfully completed. The test team performed significant characterization work on the cascade inlet to achieve expected uniform inlet conditions. Instrumentation performed as expected, and probe effects were accounted for in the data. The test determined nozzle performance at a range of solidities, including performance derivatives of pressure ratio, Reynolds Number, incidence, and turbulence. The test also quantified performance impacts of post-throat cooling injection at

various locations on low solidity airfoils, along with performance derivatives of coolant blowing ratio. Critical total pressure loss performance data for the two objectives of the S2N Linear Cascade test was successfully obtained. Background-oriented Schlieren images were used to visualize the flow field with the addition of post-throat cooling, highlighting boundary layer formation differences between solidities. Overall performance conclusions for the two objectives of the test were made.

5.2 CW22 Stage 1 Blade

The objectives of the CW22 S1B Linear Cascade test were completed and data quality was satisfactory. At the aerodynamic design point, the medium solidity demonstrated the best performance over the baseline and low solidity blades. As incidence became more negative, this performance trend stayed the same. At positive incidences, the low and medium solidity blades showed increased loss, and medium solidity was more incidence tolerant. Data at off-design conditions demonstrated similar performance trends between the three solidity blades. Stagnation region differences between the three solidities and as incidence changed were measured and observed. Preliminary PSP data resulted in learnings to inform further development of the technique.

5.2.1 Data Acquisition and Reduction

The CW22 S1B Linear Cascade followed identical data acquisition and data reduction process as the S2N Linear Cascade test. The same two non-dimensional coefficients were defined for post-processing to be used as figures of merit when assessing performance. The coefficient of total pressure ($C_{p,t}$) was used as a measure of total pressure loss and average performance. The coefficient of static pressure ($C_{p,s}$) was used to post-process, plot, and analyze surface blade loading data.

$$C_{p,t} = \frac{P_{t,1} - P_{t,2}}{P_{t,1} - P_{s,2}}$$

$$C_{p,s} = \frac{P_{s,local} - P_{s,2}}{P_{t,1} - P_{s,2}}$$

The test data was comprised of a set of traverse points distributed laterally across the downstream region at fixed distances from the blade trailing edge for a single survey, which made up wake profiles shown in the results. The same averaging process employed in the S2N Linear Cascade post-processing was utilized for this test to process the data. Similar one-dimensional averages were used to demonstrate trends from testing and draw high-level conclusions.

5.2.2 Rig Aerodynamic Validation

5.2.2.1 Inlet Characterization

Learnings from the S2N Linear Cascade test were leveraged to complete cascade balancing of the S1B Linear Cascade test. For each combination of solidity and incidence angle, the test team implemented unique combinations of upper and lower blockages, which controlled upper and lower cascade throat areas. The goal of optimizing the upper and lower blockage in the cascade was to obtain a uniform inlet total pressure profile into the test section and uniform exit swirl angle out of the test section. The team optimized each configuration by obtaining upstream traverse data at the range of test matrix conditions, tuning the cascade geometry as needed (opening or closing upper/lower blockage). Real-time monitoring of the traverse data (Cp_T, inlet angle, and Mach number) assisted in balancing the cascade. The team performed turbulence grid blowing ratio sweeps for each configuration to determine the optimal blowing ratio for

uniform inlet conditions and periodic blade loadings. In S1B testing, the team observed that the two tested Reynold's numbers occasionally necessitated different turbulence grid blowing ratios.

After completing inlet characterization and downstream data acquisition for the baseline solidity blade, a large amount of variation in the exit swirl angle was observed in the downstream data. The skewed exit angle was attributed to the blockage plate used in inlet characterization protruding aft of the exit metal angle of the test section. Inlet characterization was repeated for the cases with large exit swirl variation using different blockage plate configurations (Blade 1 was inserted instead of an upper variable plate), and a more uniform exit swirl angle was achieved. This process is shown in Figure 85 below.

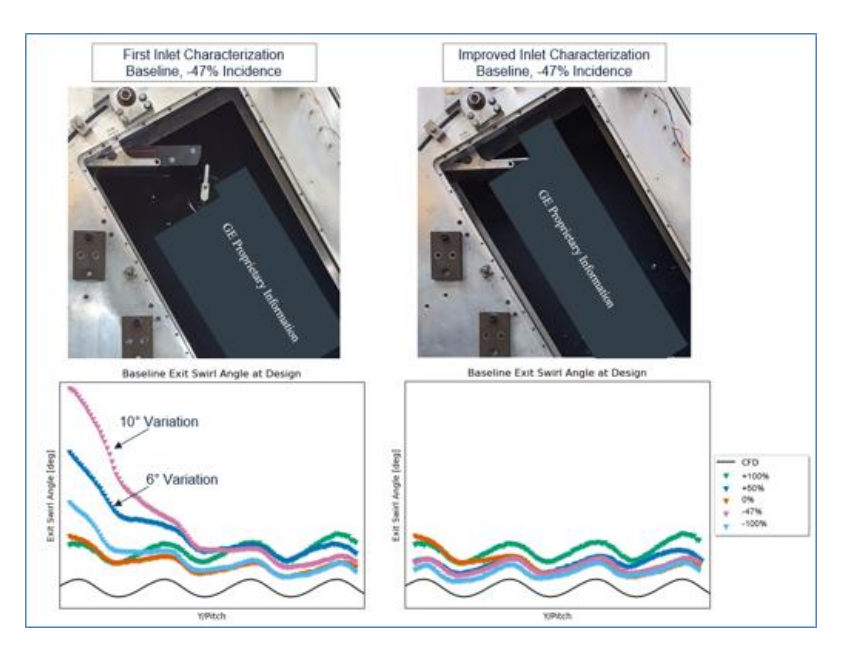


Figure 85: Improvement of Exit Swirl Angle from Adjust Inlet Characterization on Baseline Blade

Figure 86 below shows the different blockage configurations used during inlet characterization for the low solidity blade.

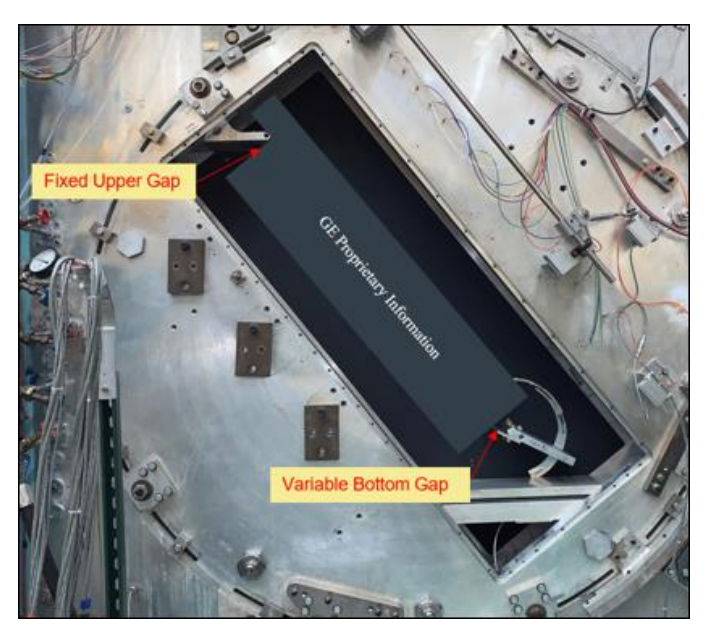


Figure 86: Cascade Blockage Plate Configurations for Low Solidity Blade

The correction employed in S2N Linear Cascade testing to account for the differences between inlet Kiel probe and upstream traverse data observed during inlet characterization was also utilized in post-processing for the S1B Linear Cascade test. The correction was 0.001 pts CP_T or below for all cases. The magnitude of the correction for the lowest solidity test was notably lower since the test team optimized the inlet characterization process by that point in testing. All corrections were within uncertainty, but the process was completed for consistency with the S2N Linear Cascade test.

Variation between the wakes of the instrumented airfoils were assessed to ensure periodicity. Based on the variation between wakes for the three solidities, one blade wake was chosen per solidity to compare overall loss averages. The appropriate wake was chosen based on the centrality of the blade in the test section and the exit swirl angle profile of the solidities. Blade 6 was used for the baseline, Blade 5 was used for the medium solidity, and Blade 5 was used for the low solidity blade. To help assess wake variation, a measurement uncertainty analysis was performed for the cascade at its test matrix operating conditions. Each combination of pressure ratio, Reynolds number, and inlet angle had a corresponding uncertainty.

5.2.2.2 As Tested Hardware vs. Design Intent

As tested hardware compared to design intent was also an area of in-depth discussion between the design and test team. The procurement of metal airfoils helped to achieve consistent throat measurements across the cascade. However, the manufactured airfoils were improperly machined to a different axial chord. The baseline and medium count airfoils were manufactured to slightly smaller axial chord than intent. The issue affected the solidity at which each airfoil was run, but the geometry miss did not affect the overall objective of the test to compare solidities. Trailing edge thickness measurements were obtained using a 3D scan of the trailing edge of the test articles. The measured trailing edge thicknesses were all within drawing tolerances.

5.2.2.3 Probe Mach Number Correction

Mach number probe data corrections like the S2N Linear Cascade test were needed for the 103% design PR cases on the low, medium, and baseline solidity data. At this operating cascade pressure ratio, erroneous Mach number readings in the post-processed traverse probe data necessitated correction to the expected exit flow Mach number.

5.2.3 Design Point Performance

The downstream traverse data was assessed to understand differences in average loss, wake plots, and loading plots. Performance conclusions were formed at the aerodynamic design point of 100% design PR and 100% design Re for varying incidence. First, 1D average loss values were compared between solidities at the design point. Figure 87 demonstrates the performance measured as a change from the baseline solidity performance.

The aero design point at 0% incidence showed that lower solidity had lower loss than the baseline. Lower solidity continues to show improved performance at negative incidence. However, at positive incidence, the low solidity blade shows a sharp increase in loss. The medium solidity blade also shows increased loss at positive incidence, but it is less sensitive to incidence than the low solidity blade. An optimum loss bucket for the medium solidity blade was seen at the -47% incidence. Comparing the CFD with test data demonstrates similar trends, although loss magnitudes are not matched.

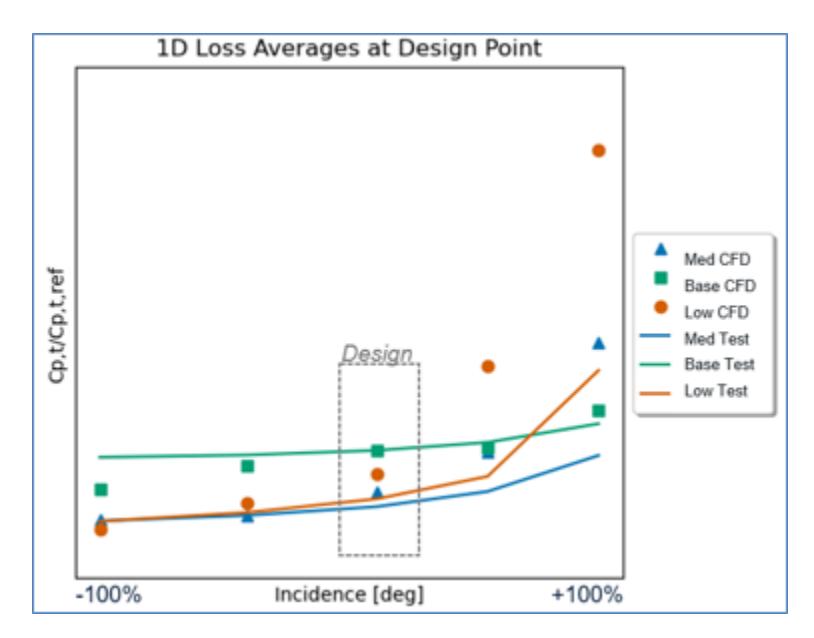


Figure 87: Design Point Trends

5.2.3.1 Probe Mach Number Correction

The traverse data was examined at the design point to understand the trends seen in the average data. As shown in Figure 88, the wake data demonstrated periodicity. Baseline and medium solidity blades showed comparable peak magnitudes of total pressure loss, while the low solidity blade showed the highest peak magnitude of total pressure loss. As expected, the CFD overshot peak magnitude, and there were dips in the freestream that were nonphysical artifacts of the CFD modeling. However, the CFD did not capture the comparable wake behavior between the baseline and medium solidity blades.

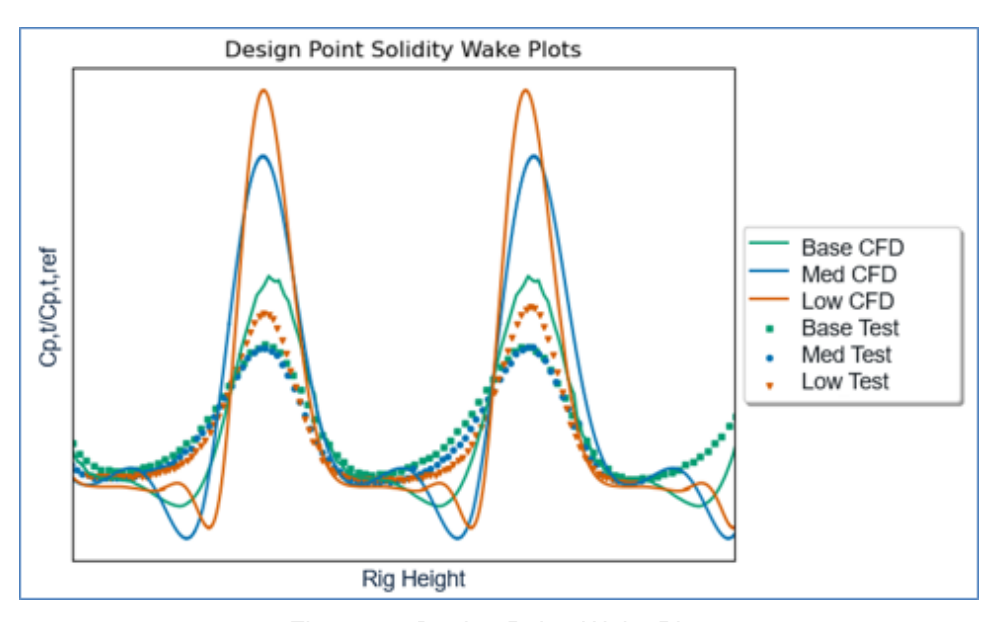


Figure 88: Design Point, Wake Plots

Airfoil loadings (Figure 89) were also examined at the design point to understand the trends seen in the average data. Airfoil loadings of static pressure coefficient versus normalized fraction of axial width were plotted for the three solidities. The airfoil corresponding to the one used for 1D averaging was used to compare blade loadings: Blade 6 was used for baseline solidity, and Blade 5 was used for medium and low solidity. Loadings were confirmed periodic for the tested airfoils for each solidity.

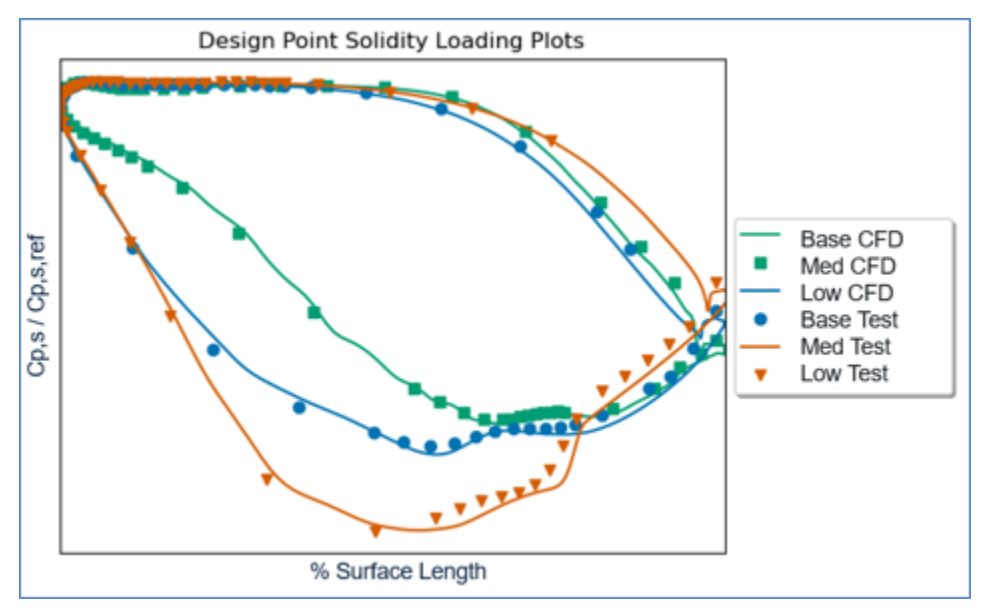


Figure 89: Design Point, Airfoil Loadings

Blade exit swirl angle was assessed at the aerodynamic design point. The traverse probe uncertainty for exit swirl was given as $\pm 1.5^{\circ}$ [5] by the test team. The exit swirl results were considered equivalent since deltas between the results were within stated uncertainty. Results are shown in Table 23.

Table 23: Design Point Airfoil Turning

	Test Data (∆ from Design)
Low Solidity	+1.1°
Medium Solidity	+0.4°
Baseline Solidity	+1.1°

5.2.3.2 Variation with Incidence

Blade behavior was assessed for each solidity as incidence was varied. Results are shown in Figure 90. Generally, as incidence became more positive on the blade, the leading-edge region of the loadings became larger. Minimal changes were observed towards the trailing edge of the blade on both pressure and suction sides as incidence changed. The blade loading behavior closely matched CFD predictions.

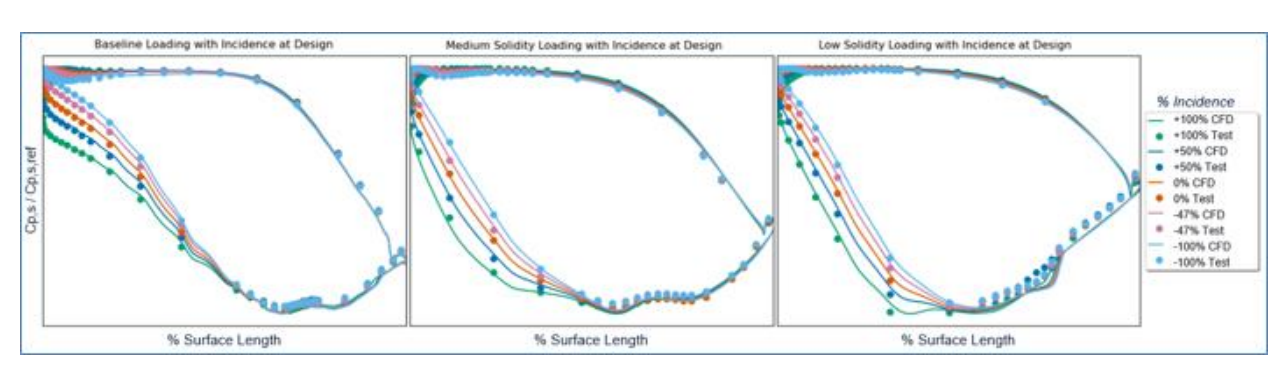


Figure 90: Blade Loading Variance with Incidence at Design PR/Re

For each solidity, traverse wake profiles and exit swirl angle profile was compared with incidence changes and to CFD predictions, shown in Figure 91. The CFD wake profile for each solidity showed peakier

behavior with a freestream dip residual from CFD modeling, and this behavior was expected. The baseline solidity wake plots generally matched trends observed in the CFD. Slight deviation was observed in the exit swirl angle plots because of the optimized inlet characterization process, but all exit swirl angle profiles fell within the reported traverse probe angle uncertainty. Plots are shown in Figure 92.

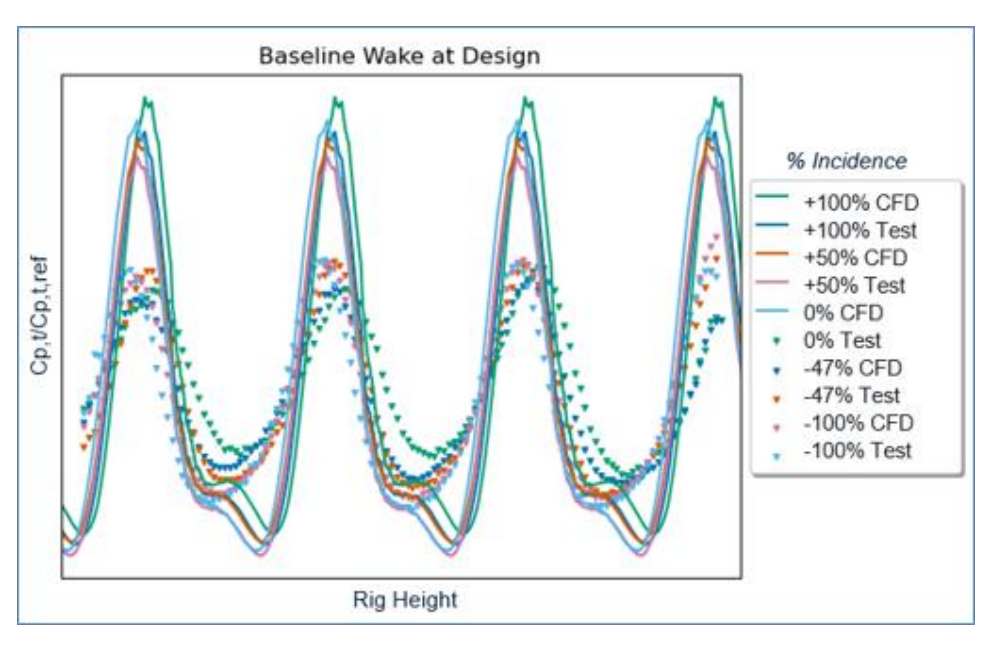


Figure 91: Baseline Wake Variance with Incidence

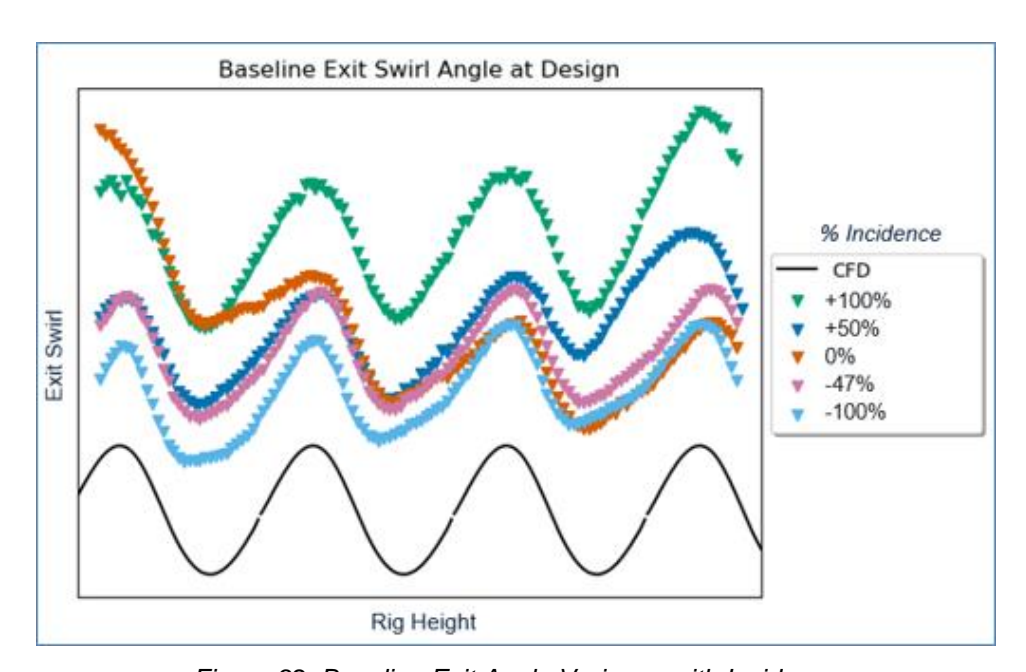


Figure 92: Baseline Exit Angle Variance with Incidence

The medium solidity wake plots matched trends with incidence from the CFD closely, as shown in Figure 93. Figure 94 shows, exit swirl angle was only slightly higher than the predicted CFD angle and within uncertainty. The +100% incidence exit swirl angle deviated farther from the other cases due to the optimized inlet characterization process.

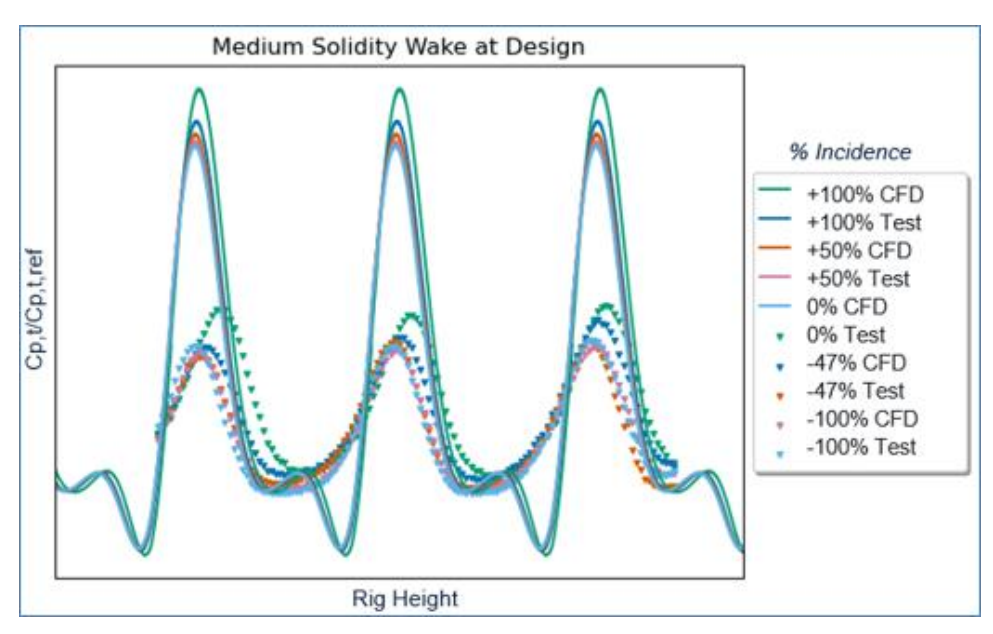


Figure 93: Medium Solidity Wake Variance with Incidence

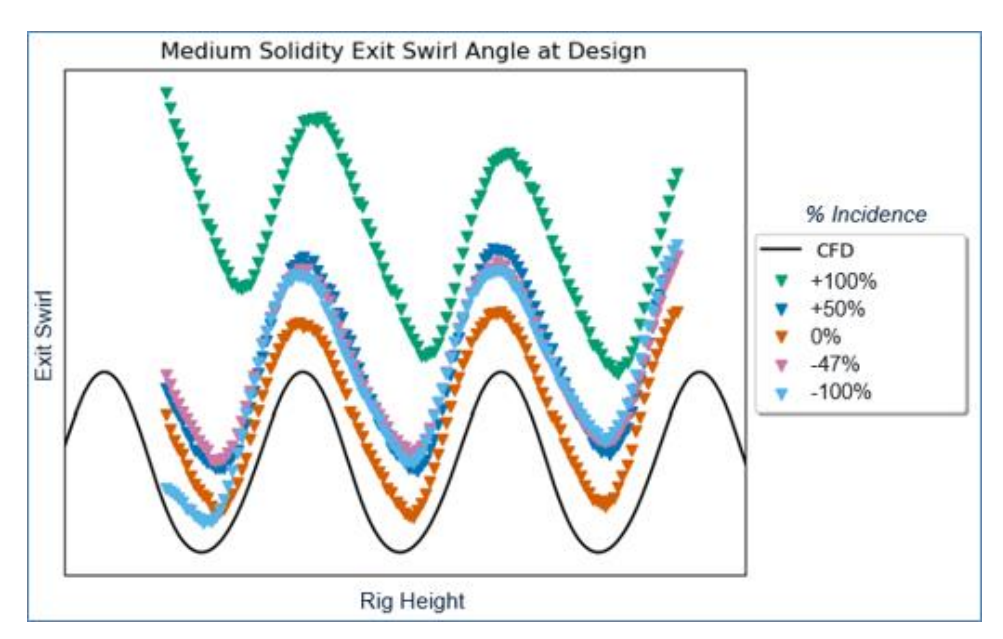


Figure 94: Medium Solidity Exit Angle Variance with Incidence

The low solidity wake plots matched trends with incidence from the CFD closely, shown in Figure 95. Figure 96 shows, exit swirl angle was only slightly higher than the predicted CFD angle and within uncertainty. The +100% incidence exit swirl angle does show evidence of under-turning relative to the other cases, but there is also deviation near the left side of the plot caused by the downstream flow field being disturbed due to the geometry used to achieve a balanced inlet, as discussed in section 5.2.2.1.

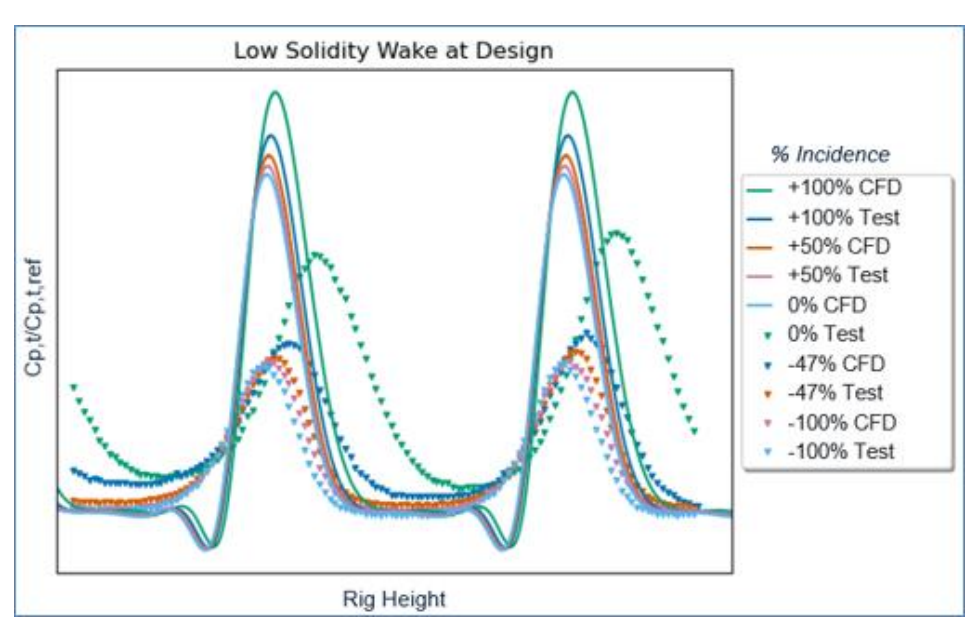


Figure 95: Low Solidity Wake Variance with Incidence

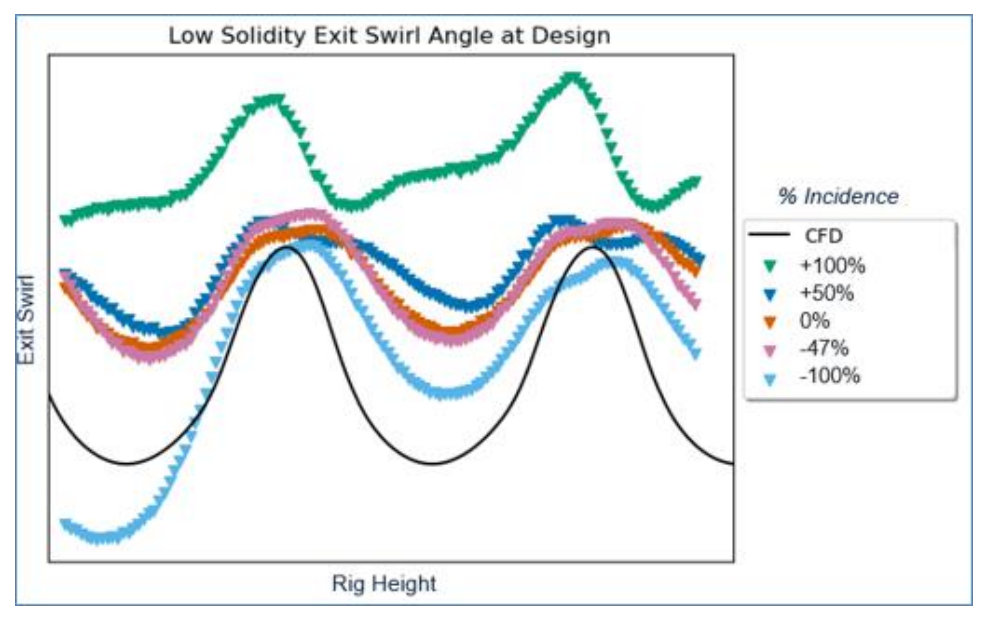


Figure 96: Low Solidity Exit Angle Variance with Incidence

5.2.3.3 Stagnation Region Assessment

A main objective of the test was to characterize the stagnation region behavior for each tested solidity at design and off-design incidence levels. Close-up views of the blade loading plots assisted in understanding and comparing the stagnation region between solidities and to CFD modeling.

Figure 97 shows a side-by-side comparison of the stagnation region of the three tested blade solidities. Direct comparisons could be made between the three plots to understand low solidity blade performance. Overall, the stagnation region was larger for the lower solidity blades than for the baseline blade, which was an expected result. As the blade incidence increased from most negative to most positive, the

stagnation region width also increased per solidity. The comparison between CFD and test data in the stagnation region will continue to be investigated moving forward.

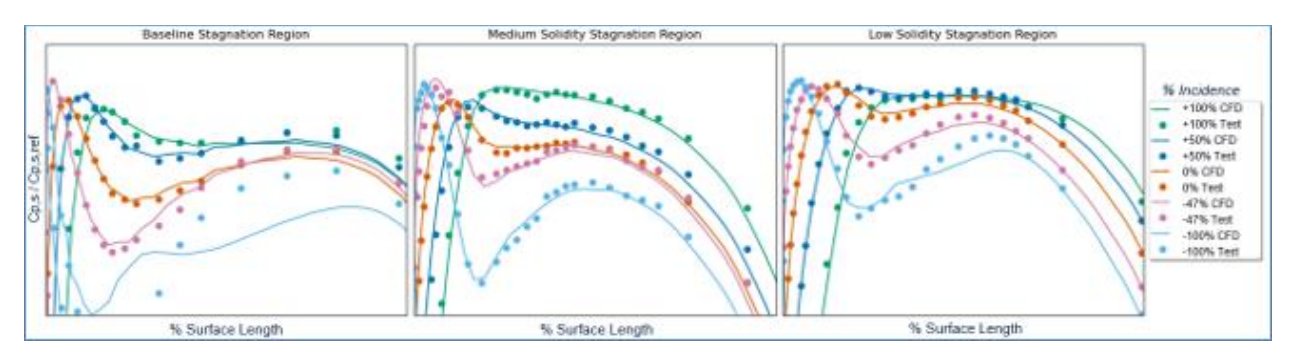


Figure 97: Close-up of Stagnation Region in Blade Loading

5.2.4 Off-Design Performance and Derivatives

Average performance was also assessed at off-design points, examining the differences in average total pressure loss as incidence, pressure ratio, and Reynolds number changed.

5.2.4.1 Reynolds Number Derivative

The average performance of the three blade solidities was assessed as Reynolds number changed, as shown in Figure 98. The impact of changing Reynold's number was assessed at the design cascade pressure ratio.

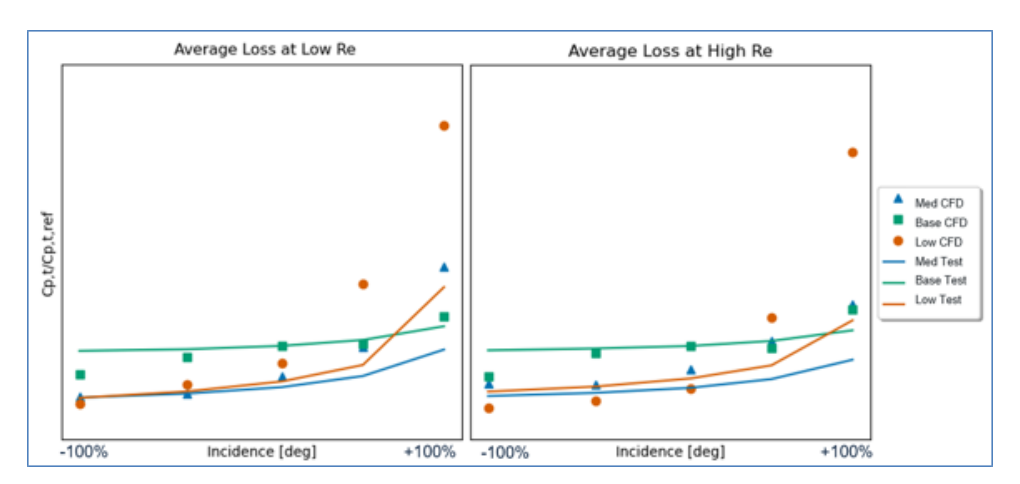


Figure 98: Reynolds Number Variation at Design PR

As Reynolds number increased, the baseline blade maintained the same overall trend, with more total pressure loss at design and negative incidence than the medium and low solidity blades. The medium solidity blade shows similar loss magnitudes at both high and low Reynolds number, with an optimum minimized loss bucket at -47% incidence. However, the low solidity blade demonstrated decreased loss at the higher Reynolds number and the lowest loss at the design incidence. The low solidity blade showed a sharp decrease in performance at positive incidence at both Reynolds number conditions. Overall, the test trends match the CFD modeling trends, except with the low solidity at highest Reynolds number.

5.2.4.2 Pressure Ratio Derivative

The average performance of the three blade solidities was assessed as cascade pressure ratio increased and decreased from the design point, as shown in Figure 99. The high and low cascade pressure ratios were assessed at the design Reynolds number.

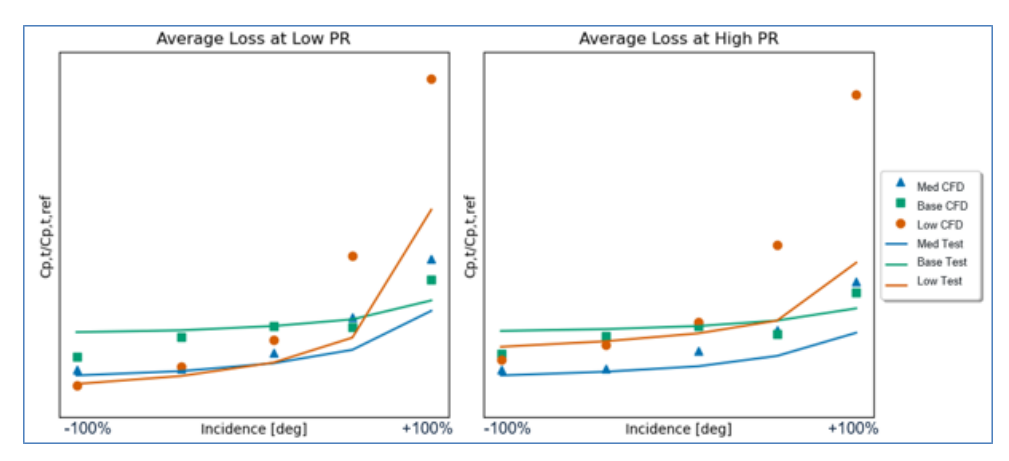


Figure 99: Pressure Ratio Variation at Design Reynolds Number

At both high and low cascade pressure ratio, the overall test trends between the baseline and medium solidity blades stay the same. However, the low solidity blade performance becomes worse at the higher pressure ratio. At both pressure ratios, the medium solidity shows the lowest loss at the design incidence, the low solidity shows a sharp fall-off in performance at positive incidence, and the baseline has highest loss at design and negative incidences. The trends at both high- and low-pressure ratio for the low solidity blade indicate that the minimum loss could be at a more negative incidence than what was tested. Overall, the test trends match the CFD modeling trends.

5.2.5 Pressure Sensitive Paint Data

PSP data was only acquired for the medium solidity blade. Difficulties in data acquisition, quality, and processing inhibited further PSP data acquisition on the other solidity blades.

The PSP data was plotted visually using a contour of static pressure representing the imaged region. Subsequently, a lateral average of the PSP static pressure contour data was taken at the location of the static pressure taps. The lateral average was plotted on a line plot with the corresponding static pressure taps to directly compare the static pressure levels between both data acquisition methods. Ideally, there would be an overall match between PSP data and static pressure tap data. Figure 100 below shows the contour data and line plot comparison for the design point and reduced pressure ratio conditions. There is a general match between the PSP and static pressure taps on the pressure side of the blade, but near the stagnation region of interest, the PSP data does not match the taps. The large red region at the stagnation region was attributed to the high curvature of the blade accompanied by reflections and uneven lighting conditions internal to the cascade. The main conclusion from the PSP data results is that more development is needed on the technique to obtain meaningful PSP results for the types of airfoils tested in this campaign (high stagger airfoils with high leading edge curvatures).

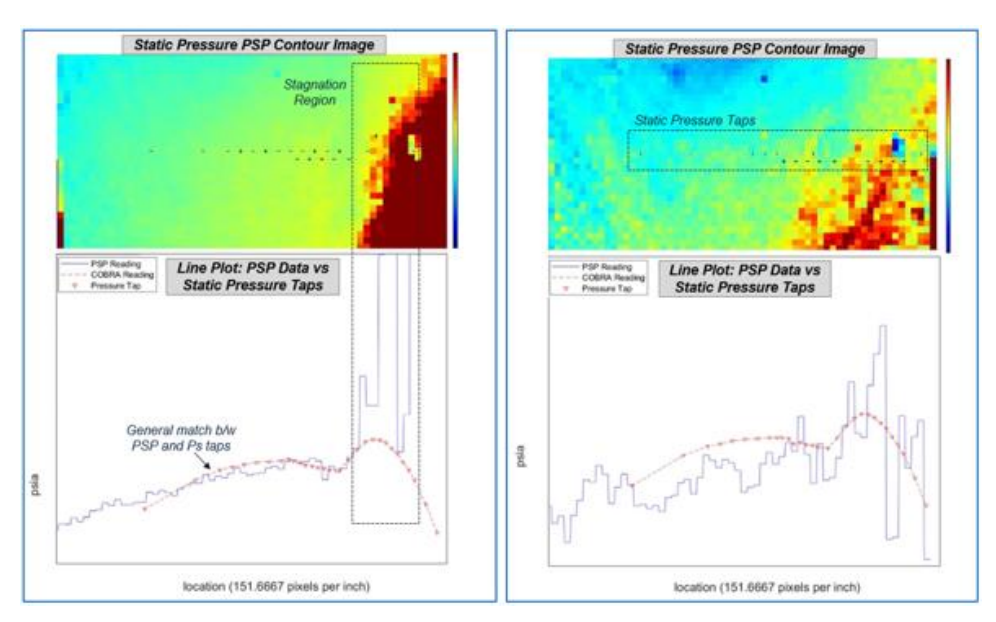


Figure 100: PSP Data for selected conditions

Discussions with the NASA PSP test team identified several key areas of improvement for further development of the PSP Data acquisition and reduction method. Work in these areas of improvement will be key for future implementation of PSP in the CW22 cascade to acquire meaningful results. The lessons learned were consolidated and discussed further in the Appendix.

- 1) Non-Uniform Lighting
- 2) Fiducial Size and Location
- 3) Fiducial Proximity to Pressure Taps
- 4) Image Distortion Created by Vibration and Frame Rate
- 5) Non-Stereo Parallax Removal
- 6) Insufficient Agreement between PSP Ratios and Absolute Pressures
- 7) Improvement to Data Reduction Methods

5.2.6 Test Results Conclusion

All test objectives were achieved for the CW22 S1B Linear Cascade test. Data was successfully acquired and assessed for the solidity comparison, incidence sensitivity, and stagnation region assessment objectives of the test. Appropriate steps were taken to validate the cascade setup, data acquisition, and data results to provide confidence in the results. All lessons learned were carefully noted to inform future testing. Design and off-design performance was also assessed and compared to CFD simulations.

The performance results from the S1B Linear Cascade were used to determine overall progress towards technology development. The test informed one of the NASA TPMs:

(1) Low Solidity Optimized Airfoil: optimize airfoil design for solidity for a 0.10-0.23 pt fuel burn improvement.

The test was assessed to anticipated technology development levels by comparing total pressure loss, measured as $C_{p,total}$.

Table 24 below shows the total pressure loss measured for the two lower solidity blades in the test, with the corresponding improvement in aerodynamic loss from the baseline blade shown.

Table 24: Performance Results for TPM Estimates

Solidity	Tested	C _{p,total} [% improvement]
Medium Solidity	Loss Difference from Baseline	14
Low Solidity	Loss Difference from Baseline	8

For this test, only differences in two-dimensional airfoil profile were considered to impact losses. Based on the results above, the aerodynamic losses tracked as expected for both lower solidity airfoils in the test. Based on the test results, both the lower solidity blades showed an improvement to 2-D aerodynamic loss over the baseline solidity at the design incidence, though the lowest solidity tested showed large losses at off design incidence. Low solidity blade performance will be further informed by TRT testing, which includes 3D blade effects.

Testing was successfully completed. The test team performed significant characterization work on the cascade inlet to achieve expected uniform inlet conditions. Instrumentation performed as expected except for PSP instrumentation, and probe effects were accounted for in the data. The test determined blade performance at a range of solidities, including performance derivatives of pressure ratio, Reynolds number, and incidence. The test quantified the impact of incidence at the aerodynamic design point and provided a comparison of stagnation regions between solidities. Critical total pressure loss performance data for the S1B Linear Cascade test was successfully obtained. Overall performance conclusions for the test were made. All test objectives were achieved.

5.3 Transonic Research Turbine

5.3.1 Data Summary

The TRT rig tested 4 configurations with the objective of advancing the following technologies to TRL4: low solidity, advanced tip, and blade hub platform contouring. The 4 builds ran at the intended operating conditions allowing for all planned test data to be recorded. Further post-processing showed tip clearance had degraded stability across all builds and issue with purge mass flow measurement was identified. Due to these findings, the reported uncertainty for TRT testing is larger than historical experience.

FRAP area traverse measurements were taken at ADP for all builds. Relevant flow physics are identifiable in post-processed results. Quantitatively, for low solidity technology, the trends measured agree with those from CFD, albeit with a larger loss than expected. For the tip treatment technology, data shows agreement with CFD trends, but integration of the data is not consistent with the observed physics improvements. Finally, there was no statistically appreciable difference measured for the inclusion of hub platform contouring in this test set-up. Differences in the flow field could not be detected using FRAP measurements.

5.3.2 Data Acquisition and Reduction

5.3.2.1 Data Acquisition Systems

Data is acquired through 3 main acquisition systems: Cyres (low-speed aerodynamic data), Apex (high-speed rig monitoring), and the GEA traverse system (FRAP, 5-hole probe, and hot wire traverses). Table 25 shows an overview of the capability of each system.

DAQ Capacity Comments Records Steady State Aerodynamic Data 256 Pressures **Analog Readings Cyres** 144 Temperatures GUI's for live monitoring 64 Analog Communicates with MATLAB processing Records Dynamic Rig Data **Digital Readings Apex** 64 Dynamic **Kulite Pressure Readings** Digital Tip Clearance Measurement GUI's for live monitoring Records Unsteady Aerodynamic Data 5 Traverse **FRAP Area Traverse GEA Traverse** Actuators/Probes **System** 5-hole Probe Radial Traverse (4 Radial/1 Area) **Hotwire Radial Traverse**

Table 25: Overview of TRT DAQ Systems and Capabilities

Cyres is mainly used for aerodynamic steady state data collection and rig aerodynamic monitoring. This system measures all pressure, temperature, torque, wheelspeed, and mass flow readings. It is used as the main indicator for live monitoring rig operating condition. The system records 30 seconds of data for every steady state reading and saves the data in separate reading files. Data that is recorded is then processed through GEA Phase 1 code, the main steady state raw data post-processing code. This post processor will filter erroneous readings, average recorded data, and calculate relevant aerodynamic quantities.

Apex is mainly used for dynamic rig monitoring. This would include rig/facility vibration data, accelerometer data, tip clearance measurements, and Kulite pressure readings relevant to the safe operation of the rig. These data are displayed live and monitored continuously during testing. The system also records 30 seconds of data when steady state readings are taken and saved.

Lastly, the GEA traverse system records all unsteady aerodynamic data. It controls, records, and post-processes all five traverse probes positioned in the test section.

5.3.2.2 Data Acquisition Strategy

Once the rig was operating and stable at the desired ADP condition, the data acquisition period commenced. A steady state data recording was taken first. Once completed, inlet radial traverse data collection was completed. The radial traverses recorded data at 25 span locations starting from the case and moving inboard towards the hub. The inlet radial traverse survey took approximately 20 minutes. Next, the team moved to operating the exit traverse probes.

When operating the FRAP area traverse, the survey window was composed of 13 radial plunges, capturing one nozzle passage. This ensured complete coverage of the nozzle wake. Each radial plunge was composed of 22 span locations. At each span location the probe settled, yawed into the flow, and recorded a

continuous stream of total pressure and total temperature for 3 seconds. Once the traverse finishes the radial plunge, the probe was retracted, and the circumferential position was moved. On average a FRAP probe plunge took 15 minutes. As the FRAP traverse was completing a radial plunge, the 5-hole probe and hot wire traverses were completing radial plunges simultaneously.

In between every FRAP traverse radial plunge, the rig operating condition was assessed for stability and operating condition was adjusted as needed. Once rig stability was confirmed, a 30 second steady state reading was taken, and the next radial plunge was commenced. During the FRAP traversing operation, 13 steady state readings were taken. In total, the FRAP area traverse data collection period for a complete nozzle passage took approximately 4 hours.

5.3.2.3 Data Reduction

STEADY STATE DATA

After completion of testing, all steady state data files were processed through GEA Phase 1 code. This post-processing code took each steady state reading and performed various calculations. First, the raw data was filtered for erroneous readings which were removed from the data. Second, the filtered data was reduced to a time-averaged 1D value. Third, turbine aerodynamic quantities were calculated. These quantities included pressure ratio, turbine efficiency, corrected speed, flow function, purge percentage, etc.

During ADP testing, there were at least 13 steady state readings during an ADP data collection period. Outputs for each of the data sets were then time averaged to produce a 1D steady state reading. The data shown for each test article in the following sections are the reduced steady state averages recorded during the ADP data collection period.

FRAP AREA TRAVERSE DATA

FRAP area traverse data was immediately processed after each radial plunge to assess the health of the probe and data quality during testing. The time-average "Preview" dataset provided a quick view of the data to ensure the data was of acceptable quality before proceeding with subsequent plunges. Radial plunges that did not pass the health-check assessment were immediately repeated. The health-check parameters that were analyzed after each radial plunge were:

- Quality of 1/rev signal used for phase-locking data
- Quality of the in-situ sensor calibration used to correct factory calibration of transducers
- Relative alignment of probe to average flow vector
- Comparison of time-average radial profiles (PT, PS, Mach, TT, swirl/yaw, pitch) to pretest, 5-hole probe, and hot firm probe data.

At the conclusion of the data collection and previewing the data while on test, the complete, unsteady post-processing was completed. The basic steps outlined below:

- 1. Phase-lock data to rotor 1/rev
- 2. Apply sensor calibration (pressure and temperature)
- 3. Apply in-situ sensor calibration correction (gain and offset)
- 4. Apply aero calibration to determine PT, PS, swirl/yaw, and pitch angles
- 5. Compute additional aero quantities and statistics (Mach number, tangential velocity, relative swirl, relative total pressure, standard deviation, etc.)
- 6. Compute individual phase-locked ensemble averages
- 7. Resample and phase-shift individual plunge ensemble averages
- 8. Compute average of all phase-shifted individual radial plunges (3D contour)
- 9. Reduce 3D contour to a 2D profile using circumferentially mixed averaging
- 10. Reduce 2D profile to a 1D value by radial mass averaging

Figure 101 shows a visual representation of the reduction process.

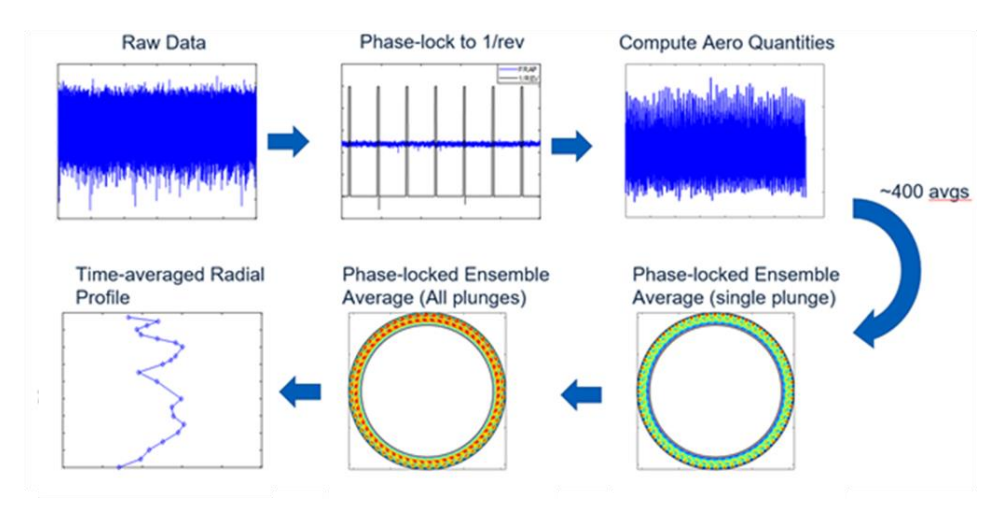


Figure 101: FRAP data reduction process

COEFFICIENT OF TOTAL PRESSURE (CPT) CALCULATION

Once all data was converted and reduced as described above, a further post-processing step was taken to evaluate Cp_T . Cp_T is defined per the equation below. All blade exit conditions were directly from FRAP measurement reduced data. The blade inlet conditions were predicted through boundary condition matched 1D analysis using GEA's proprietary turbine meanline code. Since the calculation is in relation to the blade, all total pressure quantities are in the relative reference frame. Comparisons between builds will be made by calculating the difference between each build's respective Cp_T , providing a delta coefficient of total pressure (ΔCp_T).

$$Cp_{T} = \frac{PTR_{Exit\ Frap} - PTR_{Inlet\ 1D\ Model}}{PTR_{Inlet\ 1D\ Model} - PS_{Exit\ FRAP}}$$

FRAP UNCERTAINTY ANALYSIS

An analysis was performed to determine the uncertainty in ΔCp_T , as measured by the FRAP probe, between tip treatment and baseline sectors on the Rainbow B4 blisk. The 2-sigma uncertainty values used for the uncertainty analysis are summarized in Table 26 (absolute uncertainties referenced from *Porreca et al.* [6] and relative uncertainties referenced from the 2014 FRAP user manual). The absolute uncertainty corresponds to the accuracy of the measurement, whereas the relative uncertainty corresponds to the precision. Since different sectors on a single blisk are being compared within the same air/test period, the relative uncertainties are more appropriate. A comparison of the uncertainty in ΔCp_T using both the absolute and relative uncertainties are summarized in Table 27. As expected, the uncertainty in delta ΔCp_T is greatly reduced, by an order-of-magnitude, when comparing the relative to the absolute uncertainties.

Table 26: Monte-Carlo Simulation 2-sigma Uncertainty Values

Parameter	Absolute	Relative	Comments
Total Pressure, Pt	0.0145	0.1%	psi, % dynamic head
Static Pressure, Ps	0.020	0.12%	psi, % dynamic head
Yaw Angle, alpha	0.3	0.05	Degrees
Pitch Angle, phi	0.3	0.07	Degrees
Temperature, T	0.3	0.1	Kelvin
RPM	1	N/A	rpm

Table 27: Uncertainty in ΔCp_T Comparison

Parameter	Absolute	Relative
ΔCp_{T}	0.025	0.0015

5.3.3 **Rig Aerodynamic Validation**

5.3.3.1 **Aerodynamic Quantities**

Various aerodynamic measurements are acquired during testing, but to assess operating condition of the rig, three turbine operating parameters are taken into consideration: inlet flow function, corrected speed, and total-to-total pressure ratio. These quantities will set aerodynamic similarity between builds. These are defined as below:

Inlet Flow Function:
$$FF_{inlet} = \frac{W_{in}\sqrt{TT_{in}}}{PT_{in}}$$

Corrected Speed:
$$NRT = \frac{RPM}{\sqrt{TT_{in}}}$$

Corrected Speed:
$$NRT = \frac{RPM}{\sqrt{TT_{in}}}$$

 Total to Total Pressure Ratio: $PR = \frac{PT_{in}}{PT_{out}}$

In addition to monitoring these operating parameters, various dimensional measurements are monitored to ensure the rig is operating within the intended targets: RPM, purge mass flows, horsepower, inlet temperature, inlet mass flow, and tip clearance. The rig's operating condition was assessed live to ensure these quantities were within expectation before data acquisition commenced. Inlet total pressure and humidity are not controlled in this rig but monitored during test operations. As atmospheric conditions changed during the day, the rig was adjusted to match the desired operating parameters. This ensured that operating condition was stable and within expectations.

Table 28: Baseline Blisk ADP Operating Condition

Baseline Blisk ADP	Quantity	Diff
Uncontrolled Atmospheric Conditions	Inlet PT	0.0%
	Inlet TT	0.0%
Rig-controlled Input	Corrected Speed	-0.2%
	PR Total	0.5%
Rig Output	Inlet Mass Flow	-0.1%
	Inlet Flow Function	0.0%
	Tip Clearance	36%
	Horsepower	0.1%
	Exit PT	-0.2%
	Exit TT	-0.2%

Table 28 shows the expectation of the rig operating conditions compared to test day conditions for the baseline blisk at ADP for the data collection period. At a macro level, the rig operated within expectations with the exception of the measured tip clearance. Measured tip clearances showed large variation compared to previous rig experience. More details on the impact of tip clearance measurement will follow in Section 5.3.2.2. Issues were also discovered regarding the purge flow measurements with additional details to follow in Section 5.3.3.3.

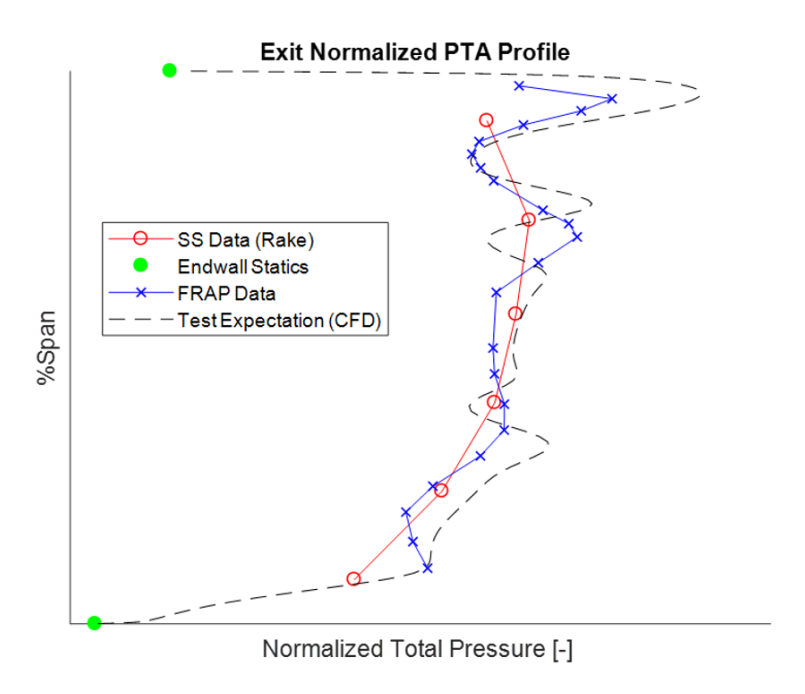


Figure 102: Baseline Blisk ADP Exit Total Pressure Profile from Rake and FRAP Measurements compared to CFD Expectations

Figure 102 shows a comparison of the exit total pressure profile predicted from CFD and measured from rakes and the FRAP probe. Good agreement is exhibited between the data and analysis. In addition, recorded FRAP and rake data show good agreement.

Table 29 shows the comparison of the Low Solidity blisk ADP operating condition to the baseline blisk ADP conditions. All controlled quantities are within 1% of expectation. Similar to the baseline blisk, the low solidity blisk measured tip clearance larger than expected but agree with baseline blisk testing measured TCL.

Table 29: Low Solidity Blisk ADP Operating Condition Compared to Baseline Blisk

ADP Operating Condition	Quantity	%Diff
Uncontrolled Atmospheric Conditions	Inlet PT	0.3%
Dia controlled	Inlet TT	0.0%
Rig-controlled Input	Corrected Speed	0.0%
input	PR Total	0.0%
	Inlet Mass Flow	-0.8%
	Inlet Flow Function	0.0%
Rig Output	Tip Clearance	0.0%
Mg Output	Horsepower	-0.5%
	Exit PT	-0.0%
	Exit TT	-0.1%

Table 30 shows comparisons for the Rainbow B5 blisk. As described in the Section 3.3, the Rainbow B5 rotor's ADP condition is tested at a reduced speed compared to the other blisks due to aeromechanics limitations. Therefore, the operating condition for this blisk is compared to the baseline blisk off-design condition at the same corrected speed. Even when considering this operating condition change, the Rainbow B5 blisk operates within expectation. The only exception is the measured tip clearance which has increased variation similar to other builds.

Table 30: Rainbow B5 Blisk ADP Operating Condition Compared to Baseline Blisk

96% NRT Operating Condition	Quantity	%Diff
Uncontrolled Atmospheric Conditions	Inlet PT	0.1%
	Inlet TT	0.0%
Rig-controlled Input	Corrected Speed	0.9%
	PR Total	0.0%
	Inlet Mass Flow	-0.2%
Rig Output	Inlet Flow Function	0.1%
	Tip Clearance	46%
	Horsepower	-0.1%
	Exit PT	0.2%
	Exit TT	-0.1%

Lastly, Table 31 shows comparisons to the Rainbow B4 build. Again, this blisk features four sectors of different technologies. The rig-controlled inputs are as expected when compared to the baseline blisk. Rig output quantities do show a shift in percent difference when compared to baseline. This difference can be explained by the uncontrolled atmospheric conditions, where a 1.5% reduction in inlet pressure is measured. While maintaining the same pressure ratio, the expected output total pressure will be lower. In addition, the lower inlet pressure results in lower mass flow when maintaining constant inlet flow function, which will manifest in lower output horsepower due to reduced available flow.

Table 31: Rainbow B4 Blisk ADP Operating Condition Compared to Baseline Blisk

ADP Operating Condition	Quantity	%Diff
Uncontrolled Atmospheric Conditions	Inlet PT	-1.5%
	Inlet TT	0.0%
Rig-controlled Input	Corrected Speed	0.1%
	PR Total	0.0%
Rig Output	Inlet Mass Flow	-1.2%
	Inlet Flow Function	-0.2%
	Tip Clearance	46%
	Horsepower	-1.3%
	Exit PT	-1.9%
	Exit TT	-0.0%

5.3.3.2 Tip Clearance Variation

As described in the previous section, the measured tip clearance showed larger variation when compared to previous testing experience. The measured tip clearances in the 2012-2013 test campaign were tightly controlled. This results in a build-to-build uncertainty of ± 0.12 pts in efficiency.

As described in the aero design section, the baseline blisk and test section hardware (inlet nozzles, tip shroud, exit case, etc) were reused from previous testing. For the current campaign's measured tip clearance, the first issue encountered is the faulty function of the 0° aft looking forward (ALF) probe. It reports an unstable tip clearance reading, increasing steadily during the test period. The behavior is contrary to the other probes and test experience. Reported tip clearance values that show this behavior are not considered in the reported average tip clearance. Secondly, data suggests a shift in average tip clearance of 38% and a variation around the annulus of 26%. This shift is present throughout the entirety of the 2021-2023 test campaign and increases efficiency uncertainty to +/-0.5 pts.

Various attempts were made during and after testing to address these issues. These included swapping probes, replacing tip clearance sensing equipment, and advanced post-processing methods. Results from these attempts did not show appreciable improvement but two discoveries were made. First, a previously undiscovered rotor whirl was found. Second, tip clearance acquisition speed was not appropriately set for blade rotor passing frequency.

Rotor whirl is calculated by using the reported drive-end and non-drive-end magnetic bearing position sensors. These report a radial displacement from centerline in the magnetic bearing W/V axis. The W/V axis is the magnetic bearing local coordinate system from where radial displacement is measured. It is defined by rotating an X/Y axis, positioned with its origin at bearing centerline, 45 degrees counterclockwise. Bearing displacements are measured relative to this coordinate system. Figure 103 shows the relationship between V/W and X/Y coordinate systems. W/V axis displacements are converted to X/Y coordinate system by a 45 degree rotation. With the known z-position and X/Y displacements of the magnetic bearings, the radial displacement is projected linearly to the rotor plane z-position (Figure 104). By assuming this linear relationship, the below equation is used to calculate the radial displacement of the rotor using reported radial displacements from both magnetic bearings at the same instant in time.

Rotor Radial Displacement:
$$P_{Rotor} = \frac{Z_2(P_{24} - P_{13})}{Z_1} + P_{13}$$

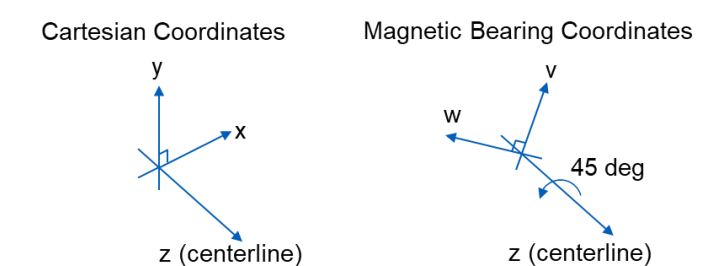


Figure 103: Magnetic Bearing W/V Axis Transformation to Cartesian X/Y Axis

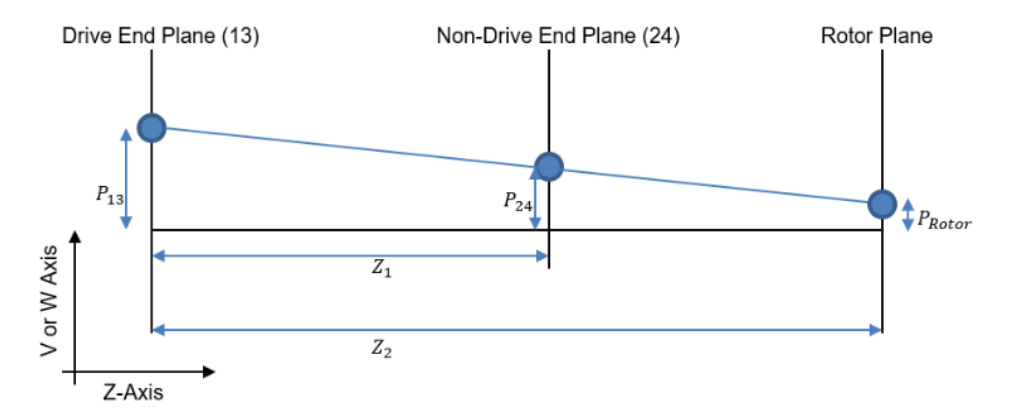


Figure 104: Rotor Whirl Linear Relationship to Magnetic Bearing Radial Displacement and Z-Position

The resultant calculation for the baseline blisk at ADP condition is a whirl affected tip clearance of +/-9.6%. This analysis shows rotor whirl can account 0.25 pts in efficiency. Figure 105 shows an example of ADP rotor whirl for the baseline blisk.

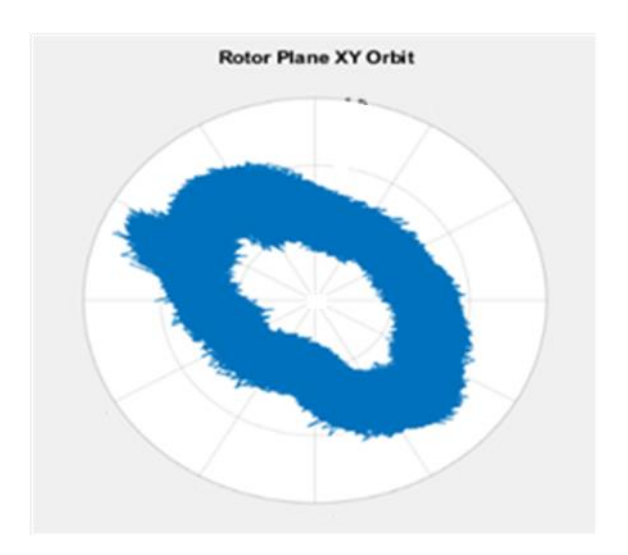


Figure 105: Calculated Rotor Whirl Pattern for Baseline Blisk at ADP.

Consultation with GEA Tip Clearance experts revealed the data acquisition speed for the tip clearance measurement system was not appropriately set. During mechanical checkout, the team was investigating large variations in the torquemeter measurement output. The torquemeter reported large fluctuations due to high acquisition speed of the DAQ. The large fluctuations reported were due to the instrumentation design, a phase displacement torquemeter that reads two 100-tooth features on the shaft for angle differences. When signal acquisition is set high enough, the device is sensitive enough to detect the minute differences in tooth dimensional variation. This in response reports large variations in torque. The team concluded that by lowering the acquisition speed to past experience, the reported torque variations would be physical. The downside that was not taken into account, is that lowering this speed in the DAQ system would also affect tip clearance acquisition speed. The error was only detected post-test.

5.3.3.3 Purge Mass Flow Issues

Two issues of note that occurred with the purge flows will be discussed in this section. First, a post-test audit of TRT facility processing codes revealed an equation error in the calculation of purge orifice plate mass flow. Second, a purge line leakage was discovered late in the testing campaign.

PURGE MASS FLOW MEASUREMENT ERROR

During a post-test TRT facility processing code audit, a mathematical error was identified in the calculation of mass flows for all purge lines. This error resulted in the measured mass flows monitored during testing to display higher flows than actual. This resulted in the actual purge mass flows being set lower than the intended targets. Due to the design of the TRT test facility this error affects various fundamental quantities reported by post-processed data. As shown in the test design section, the TRT facility's main air venturi is positioned downstream of the test section. Thus, it measures total exit mass flow. Inlet mass flow is calculated as per the equation below. Additionally shown are 2 turbine parameters affected directly by inlet mass flow.

$$Inlet \ Mass \ Flow: \ \ W_{in} = W_{exit} - \sum W_{purge}$$

$$Inlet \ Flow \ Function: \ \ FF_{inlet} = \frac{W_{in} \sqrt{TT_{in}}}{PT_{in}}$$

$$Torque \ Based \ Stage \ Effcieincy: \ \ \eta_{TT} = \frac{Torque Power Output}{W_{in}(Available Energy)}$$

With this calculation error corrected, Table 32 shows the average adjustment to affected quantities. In total, measured efficiency for all builds is reduced by 0.2 pts. This correction is not included in results shown in Section 4. To account for the discrepancy in the results, a downside adder of -0.2pts will be added to the rig uncertainty. When considering increased tip clearance variation and applying the purge flow measurement error, rig uncertainty will be reported as -0.7 pts to 0.5 pts on efficiency.

Table 32: Reprocessed Purge Mass Flow Impact

Reprocessed Purge Mass Flows	Diff
Tip Purge Flow	+0.3%
FWD Hub Purge Flow	-9%
AFT Hub Purge Flow	-19%
Inlet Mass Flow	-2.3%
Flow Function	+0.2%
Efficiency	-0.2 pts

PURGE LINE LEAK

Another issue encountered with the purge supplies was a leakage discovered on the final build. During ramp-up to ADP, a shift in the temperature-to-torque ratio (TMP2TRQ) was noticed. This quantity is a measure of the temperature-calculated power compared to the torque-measured power. TMP2TRQ is calculated as shown below. W is mass flow in pounds per second, H is enthalpy in British Thermal Unit (BTU)/lbm, T is torque lbf-ft, ω is RPM, and J is the conversion factor for lbf-ft/BTU. Typically, this quantity is targeted to be 1.00 + 0.005. Without corrections to account for shaft windage, post-test rake pressure and temperature measurements, or any known leakages, average TRT TMP2TRQ was recorded at 1.01. On this particular build, TMP2TRQ shifted to 0.994.

Temperature to Torque Ratio:
$$TMP2TRQ = \frac{(W \cdot H)_{inlet} + \sum (W \cdot H)_{purge} - (W \cdot H)_{exit}}{\frac{2\pi T\omega}{60I}}$$

After test completion, leak checks were performed on all purge lines. Figure 106 shows the forward (FWD) tip purge and aft hub purge lines leakages found.

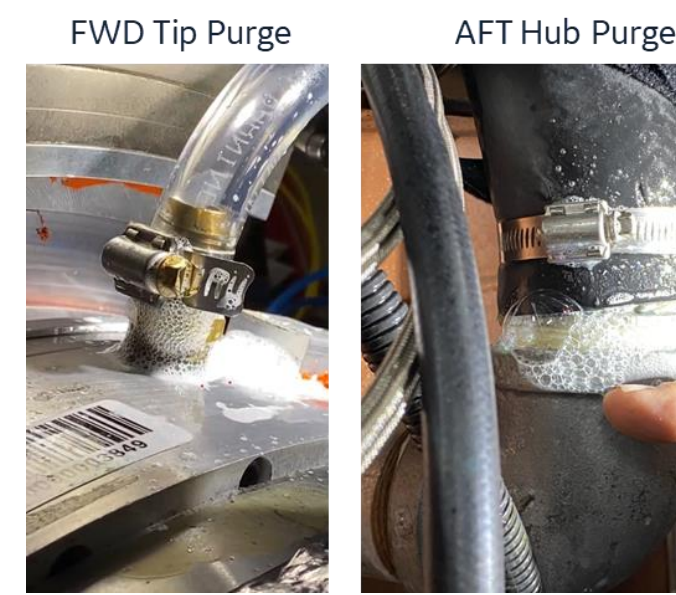


Figure 106: Post-test purge leakage checks – FWD tip purge and AFT hub purge leakages

To identify affected builds, static pressure readings within the purge cavities were compared to identify non-uniform circumferential readings in static pressure. Each cavity is fitted with 3 pressure taps spaced 120 degrees circumferentially, capturing the uniformity of the static pressure field. Table 33 displays tip purge pressure tap readings for all blisk builds at nominal clearance. The expected outcome if the rig is not leaking appreciably is a uniform static pressure field. From this exercise, it was determined that two nominal clearance blisk builds experienced higher than expected variation in tip purge pressure: non-aero tech 1 and non-aero tech 2 builds. It is evident these two builds showed a higher-than-expected variation in tip purge pressures. For the purposes of this report, the two builds affected are not presented and this leakage has been determined to not affect results.

Table 33: Tip Purge Pressure Tap Measurement for All Nominal Builds

Tip Purge PS	%STD DEV
Baseline	0.1%
Low Sol	0.3%
Non-Aero Tech 2	12%
Rainbow B5	0.2%
Non-Aero Tech 1	12%
Rainbow B4	0.2%

The same exercise was performed for the hub FWD purge and hub AFT purge. Table 34 and Table 35 show the static pressure tap distribution for FWD purge and AFT purge respectively. FWD hub purge does not show any immediate differences around the annulus. As for AFT hub purge, the standard deviation around the annulus is roughly an order of magnitude larger than the hub FWD purge pressures. In total, presented data in this report will not reflect additional uncertainty due to the leakage found. All builds show hub AFT purge pressure with higher non-uniformity, but equal magnitude, i.e., it is assumed to be the leakage.

Table 34: Hub FWD Purge Pressure Tap Measurement for All Nominal Builds

Hub FWD Purge PS	%STD DEV
Baseline	0.1%
Low Sol	0.3%
Non-Aero Tech 2	0.2%
Rainbow B5	0.1%
Non-Aero Tech 1	0.2%
Rainbow B4	0.1%

Table 35: Hub AFT Purge Pressure Tap Measurement for All Nominal Builds

Hub AFT Purge PS	%STD DEV
Baseline	1.4%
Low Sol	1.2%
Non-Aero Tech 2	1.2%
Rainbow B5	1.5%
Non-Aero Tech 1	1.4%
Rainbow B4	1.2%

5.3.4 Aerodynamic Data Discussion

5.3.4.1 Low Solidity

The low solidity technology will be compared to the nominal blisk. Figure 107 shows the contour plots for Cp_T measured at the FRAP area traverse plane. The contour displays the wake of 4 blade passages for both configurations. Regions of blue correspond to a larger Cp_T value, indicating a greater reduction in the relative total pressure across the blades. Regions of red imply the opposite, i.e. lower Cp_T indicating a smaller relative pressure drop in the region.

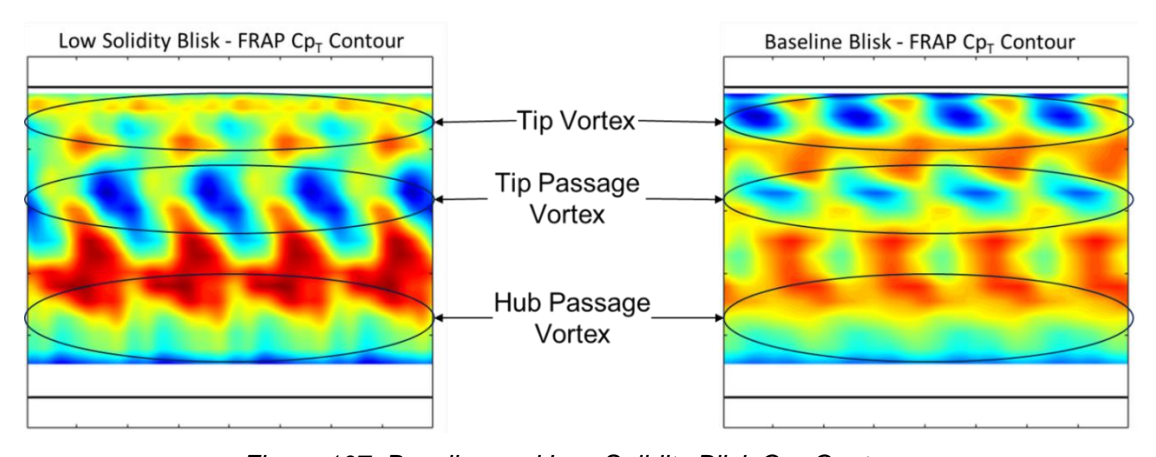


Figure 107: Baseline and Low Solidity Blisk Cp[⊤] Contours

When comparing the two, it is evident the tip region for the low solidity blisk shows a more controlled tip vortex, which would result in improved loses in the region. Moving down the span, the tip passage vortex region for the low solidity blisk shows higher loses as compared to baseline. The hub passage vortex shows

to be improved compared to the baseline blade. As the flow goes into the region below the hub passage vortex, the contours are similar, with slightly higher Cp_T for the low solidity blisk.

Figure 108 shows the ΔCp_T profiles from CFD and FRAP compared. These are generated by reducing the contour plots above into 2D profiles using circumferentially mixed averaging, then calculating the difference from low solidity blisk to baseline blisk. ΔCp_T values in the positive indicate low solidity outperforms baseline, while negative values indicate low solidity underperforms when compared to baseline. The two vertical red dashed lines show the FRAPs capability to detect a statistically significant difference (outside the measurement uncertainty) between the two profiles. In general, the FRAP can detect significant changes in ΔCp_T greater than the FRAP uncertainty.

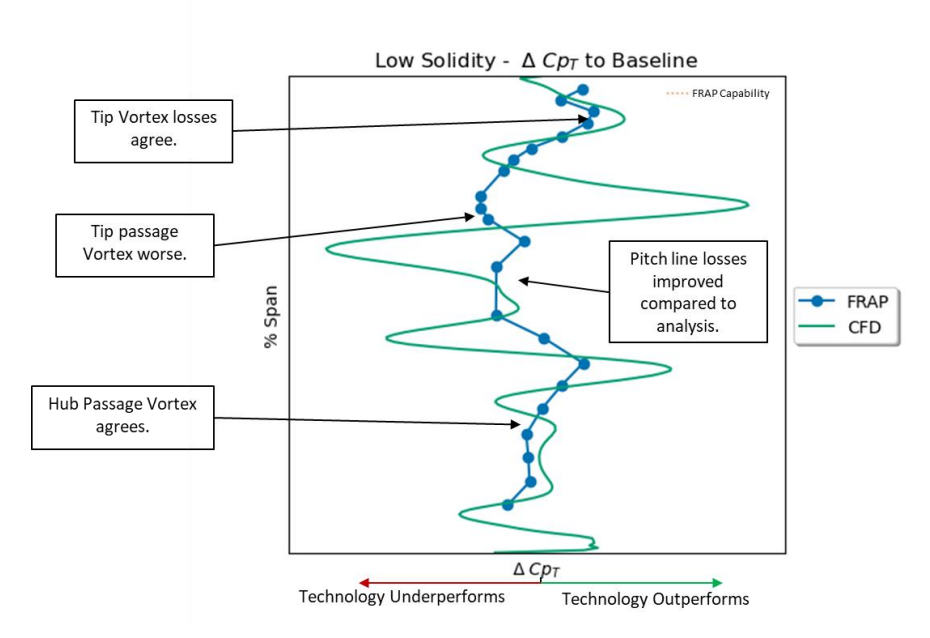


Figure 108: CFD and FRAP \(\Delta \text{Cp}_T \) Profiles - Low Solidity Blisk Compared to Baseline Blisk

The CFD analysis shows two main characteristics between low solidity and baseline. First, there are five locations along the span where it is predicted that FRAP will have the capability to detect a statistical change in the ΔCp_T profile. First, the tip vortex region shows an improvement for low solidity. As the profile moves down the span of the airfoil, the tip passage vortex is predicted to have a large improvement, while increased losses are expected in the pitch line flow. Transitioning to the lower spans, the hub passage vortex is predicted to improve, while a slight increase in hub end wall losses is predicted. These 5 regions are predicted to show differences above the capability of the FRAP probe.

The FRAP profile shows similar characteristics, with the exception of the tip passage vortex region. The tip vortex shows a positive ΔCp_T , indicating improved losses verses the baseline. The tip passage vortex shows a larger than expected increase in loses as compared to CFD expectations. The pitch line region then maintains this lower ΔCp_T as it moves to the hub passage vortex. At the hub passage vortex, the data shows an improvement in the profile as it transitions to neutral to lower losses as it reaches the hub region.

In general, the data shows the FRAP detects lower amplitude changes in the ΔCp_T as predicted in the CFD. This is due to the RANS CFD, where there is reduced mixing as compared to test. This is a known shortcoming of RANS CFD predictions. The regions from CFD that do show large magnitudes in ΔCp_T are detectable in the FRAP data, albeit at lower magnitudes. In addition, the data does not show the separation of the tip passage vortex and pitch line flow. These two regions merged creating a general region of reduced ΔCp_T as opposed to the suggestions from analysis, showing two distinct regions of flow.

Table 36: Low Solidity to Baseline 1D ∆Cp_T

Low Solidity Compared to Baseline Blisk	
	$\%\Delta$ Ср $_{ extsf{T}}$
Analysis (CFD)	-3%
Data (FRAP)	-4%

Table 36 shows the 1D average $\%\Delta Cp_T$ for the low solidity blisk compared to baseline.

5.3.4.2 Hub Platform Contouring

Hub platform contouring technology will be compared to no hub platform contouring technology from the Rainbow B5 blisk. As mentioned in the aerodynamic design section, both airfoils are the same shape with the only difference coming from the hub geometry. Figure 109 shows contour plots for Cp_T measured at the FRAP area traverse plane. The contour displays the wake of 4 blade passages within the middle of the sector. Regions of blue correspond to a larger Cp_T value, indicating a greater reduction in the relative total pressure across the blades. Regions of red imply the opposite, i.e. lower Cp_T indicating a smaller relative pressure drop in the region.

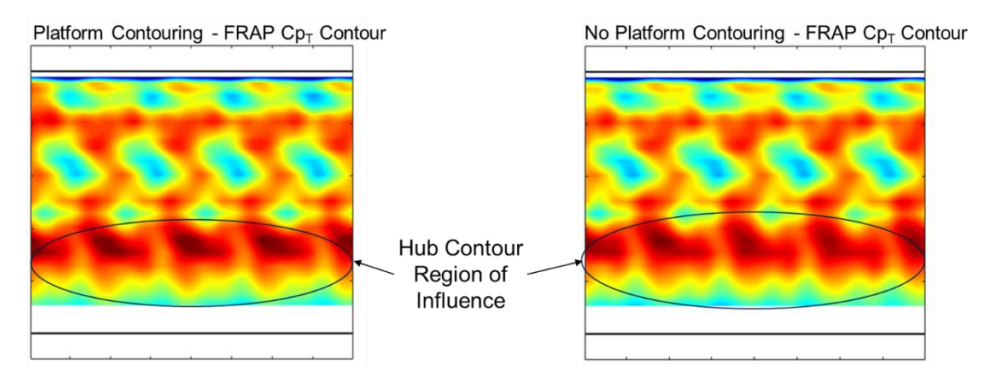


Figure 109: No Platform Contouring and Platform Contouring Blisk CpT Contours

In general, it is expected that the upper spans of the contour should have small differences in Cp_T as the region of influence for the hub platform contouring is expected in the lower spans. There are small differences in the upper spans that are due to slight changes in the local tip clearance measured as the sector passes in front of the FRAP measurement plane. Focusing on the spans where the expected influence is experienced, data shows little difference in the flow field.

When converting the contours into circumferentially mixed averaged profiles and calculating a ΔCp_T profile, as in Figure 110, it is evident that differences measured for the two technologies is small and remain within the limits of the FRAP probe's capability. As opposed to the FRAP data, the CFD analysis predicts appreciable changes in ΔCp_T . Analysis predicts an expected improvement in the hub passage vortex relative to no platform contouring and is predicted to be detectable by FRAP measurement.

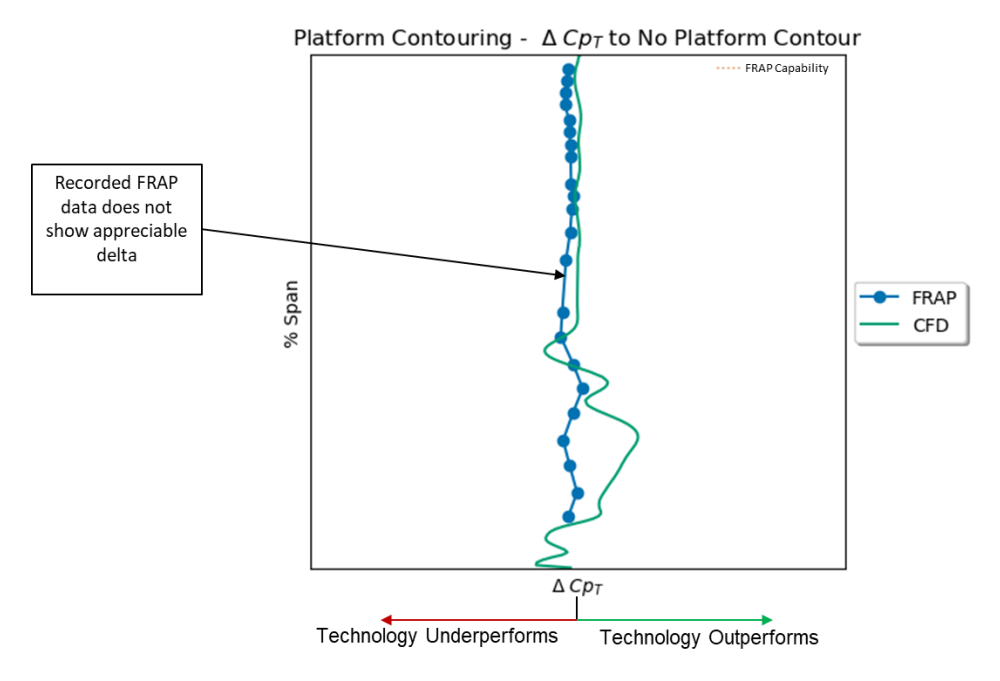


Figure 110: CFD and FRAP ∆Cp_T Profiles – Hub Platform Contouring Compared to No Hub Platform Contouring

In general, the FRAP measured profile shows neutral losses across the entire span and did not detect an appreciable difference between the two technologies. The measured difference from FRAP is smaller than the measurement capability, counter to the analytical prediction. In addition, results appear to be offset from zero across the span. Differences in manufactured hardware may account for this offset due to suspected differences in airfoil throats, though higher fidelity throat measurements would be required to confirm. This results in the test data indicating no appreciable change in ΔCp_T and therefore negligible measurable change to turbine efficiency from this technology. Table 37 summarizes this conclusion.

Table 37: Low Solidity to Baseline 1D Δ Cp $_{T}$ and Cp $_{T}$ -Based Δ η $_{TT}$

Platform Contouring Compared to no Platform Contouring	
	$\%\Delta$ Cp $_{T}$
Analysis (CFD)	3.0 %
Data (FRAP)	0.0%

5.3.4.3 Tip Treatment

The tip treatment technology will be compared to the baseline airfoil design sector on the Rainbow B4 blisk. Figure 111 shows contour plots for Cp_T measured at the FRAP area traverse plane. The contour displays the wake of 4 blade passages within in the middle of the sector. Regions of blue correspond to a larger Cp_T value indicating a greater reduction in the relative total pressure across the blades. Regions of red imply the opposite, i.e. lower Cp_T indicating a smaller relative pressure drop in the region.

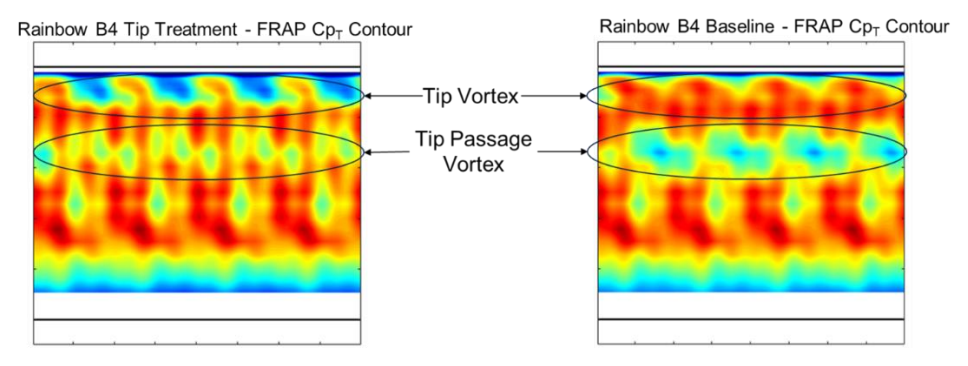


Figure 111: Baseline and Tip Treatment Rainbow B4 Blisk Cp_T Contours

The comparisons of the contour plots show appreciable flow physics differences in the upper spans of the airfoil. The design of these blades features no geometrical differences in the lower spans of the airfoil and contours confirm no appreciable difference in the flow physics in these regions. Considering the upper spans where differences are apparent, the tip passage vortex region, shows a decrease in the Cp_T for the tip treatment technology as compared to baseline. This would indicate a decreased loss region. Moving further up the span to the tip vortex region, the tip treatment technology sees an increase in Cp_T indicated by more areas in blue, indicating an increase in losses in the region.

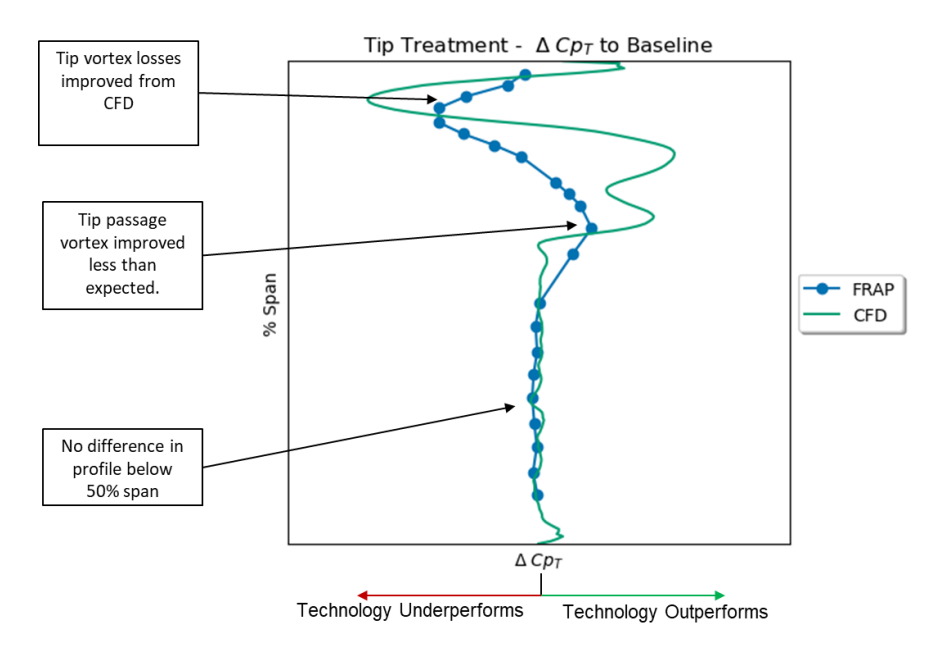


Figure 112: CFD and FRAP ΔCp_T Profiles – Tip Treatment Compared to Baseline.

Figure 112 shows the profile of the contour ΔCp_T of the tip treatment technology compared to the baseline airfoil. The CFD profile shows a large decrease in ΔCp_T in the tip vortex region which is consistent with the test data. FRAP suggests that this region of increased loss is less severe than predicted. Focusing on the tip passage vortex region, the same trends are echoed between analysis and data. CFD suggests improvement in losses in the region along with the FRAP, but measured improvement is lower than predicted by analysis. Moving below 60% span, no appreciable difference is measured or predicted from data or CFD, which is expected.

Table 38: Tip Feature Compared to Baseline 1D ΔCp_T and Cp_T-Based Δη_{TT}

Tip Treatment Compared to Baseline			
$\%\Delta$ Ср $_{ extsf{T}}$			
Analysis (CFD)	7%		
Data (FRAP)	Indeterminate		
	(-4% to 7%)		

Converting the profile into a 1D radial mass average, the integrated data produces an unexpected result. CFD predictions suggest an improvement in ΔCp_T of 7%. Despite the FRAP data showing qualitatively that the technology is creating the desired changes in flow physics, the integration of the measured profile does not match expectations, showing increased losses in ΔCp_T of -4%. As discussed in Section 5.3.3, several issues may be confounding this result, including whirl mode induced variation in tip clearance. Use of a rainbow rotor to evaluate this feature introduces additional sensitivity to these geometric variations. Specifically, there are indications that the whirl TCL was more open in the tip treatment sector than the baseline sector, which will introduce higher tip leakage and increased tip losses, and uncertainty in the outcome. Differences in TCL are difficult to detect from the FRAP when the technology is also deliberately affecting the tip region. The suspected TCL variations would be sufficient to explain a significant portion of the discrepancy between expectations and the integrated result. A summary of reported quantities is shown in Table 38. Due to the high uncertainty, GEA is considering the result as indeterminate based on the data available at the time of this report.

5.3.5 Test Results Conclusion

All test objectives were achieved for the TRT rig. Data was successfully acquired for low solidity, hub platform contouring, and tip treatment. Post-test processing determined a higher-than-expected uncertainty in the result due to issues with tip clearances and purge flow measurements. Low solidity losses were quantified for use in system level trades, as the pure aerodynamic effect is a net debit. Effects of endwall contouring were too small to quantify on the rainbow blisk using FRAP, however no evidence of detrimental effects from the technology were observed. Lastly, expected flow physics were measured for the tip treatment technologies, however additional work is required to understand the integration result that is inconsistent with qualitative trends.

5.4 Stage 2 Nozzle Annular

5.4.1 Data Summary

Data was successfully acquired to address both solidity and cooling testing objectives. Data quality was reviewed and found to be acceptable. Data corrections were documented and performed to adjust for issues encountered in test, but the effect of these corrections was minor. Low solidity was found to perform measurably better than the baseline at the design point, though its flow function was found to be low compared to pre-test predictions. The addition of post-throat cooling resulted in a measurable increase in loss, though the magnitude was lower than observed in linear cascade testing discussed in Section 5.1.

5.4.2 Data Acquisition and Reduction

5.4.2.1 Data Acquisition Approach

All data was acquired using standard GEA data systems. All data was uploaded to the GEA data repository in real time during testing. For steady state data points, two readings were taken, each 30 seconds long, with a 30 second interval between the end of the first point and the start of the second. These two readings were compared to ensure they were within measurement uncertainty of the rig to ensure operational stability

during the data acquisition process. For traverse data points, a standardized traverse program was developed which controlled the movement of the probe and initiated the correct data readings. A separate transient reading number was used for each radial immersion. Each reading contained data taken at 20 Hz of all available channels. A total of 27 immersions were used in testing, as defined in Table 39. This was a change from pre-test plans where a 28th immersion was planned at 102.5% span – this position is inside the traverse assembly and was planned for use as verification of radial position; however, due to limitations with the traverse motor controller, positions greater than 100% were not possible.

Table 39: S2N Annular Test Traverse Program

Traverse radial positions (% span)							
2.5 12.5 22.5 40 55 75 92.5							
5 15 25 45 60 80* 95							
7.5 17.5* 30 50* 65 85 97.5							
10 20 35 50# 70 90 100*							

^{* 2} steady state readings taken after traverse

Prior to data acquisition, a traverse speed study was performed to ensure the continuous traverse methodology accurately characterized the downstream wake of the vane. This was performed by varying circumferential traverse speed to determine the maximum speed at which the shape of the downstream wake was stable, as moving the traverse too quickly tends to reduce the measured variation. This measurement error is caused by the pressure response time constant of the probe, as the pressure tubing volume may not fill completely when traversing through a pressure gradient in a wake if the traverse speed is too high. Even for appropriate traverse speeds, this approach of data acquisition leads to some hysteresis effects when constructing contour plots, as measurements are offset tangentially from their true location due to the time constant of the probe. This can be adjusted in postprocessing to create smoother contour plots, however the average values reported by the processing routines are unaffected by this hysteresis.

A phase one data reduction code was developed to provide basic calculated parameters in real time for the test team. This phase one code incorporates calibration curves for the choked flow venturis used during the test and outputs calculated mass flows. Additionally, the 5HP calibration curve for the probe used in test is included in the phase one code, allowing real time visualization of total pressure, static pressure, and flow angles during test. The phase one code also calculates other parameters relevant to real-time monitoring of testing, including flow functions, nozzle and coolant pressure ratios, and mass flows at different stations, accounting for the addition of cooling.

A measurement uncertainty assessment for the instrumentation used in data acquisition was performed using GEA best practices.

5.4.2.2 Data Reduction Approach

Following initial acquisition of the data, the full traverse data was processed through a GEA proprietary traverse data processing workflow. This workflow truncates the traverse data to an integer value of passages, handles extrapolation to the endwalls based on user specified options, and conducts averaging of the data to 1D and 2D quantities. Many averaging techniques are available within this tool – for the present work area averaging, mixed out, and mass averages were the primary techniques used. Area averaging was used for all Kiel probe traverses, as well as for processing the 5HP data to compare to the Kiel probe. Mass averages were used in evaluating radial profiles and comparing to analysis. Mixed out averages were used in developing the quantitative 1-D loss values discussed in this report.

Processing was conducted in two steps. First, on the test day, the recently acquired data was processed through the workflow and evaluated for data quality by assessing rig stability during the traverse, and by

[#] Repeat traverse in opposite direction to determine circumferential hysteresis

comparison to pre-test predictions and previously acquired data. Data that was determined to be questionable would be re-taken to ensure accuracy.

Additionally, non-dimensional figures of merit were defined for assessing performance and comparison to the testing at the CW22 facility discussed in Section 4.1. The coefficient of total pressure, defined identically to the definition given in Section 5.1.2, is used to compare performance across configurations and test vehicles. These assessments assume properly functioning instrumentation in all channels. Effects of damaged or inoperable instrumentation discovered during or after testing are discussed in Section 5.4.3.

5.4.3 Rig Aero Validation

5.4.3.1 Inlet Characterization

The conditions at the inlet to the rig are measured by an array of 8 total pressures and 8 total temperatures arrayed around the annulus. As shown in Figure 113 and Figure 114, there is generally good agreement between the channels. In these plots, Channel 0 is at top dead center and the remaining channels are equally spaced, clockwise aft looking forward. This data is not corrected for standard day, illustrating the slight differences in absolute values between cases due to variations in ambient temperature and pressure on the test days. One area of note is that for plenum pressures, Channel 3 shows slightly suppressed pressures for all data points. After completion of the test, a crack was found on the pressure probe. For all data, the upstream average PT was recalculated, discarding the channel with a crack, then the potential performance variation was added to the uncertainty in the measurements. The variation in the inlet temperatures for each test case is within the variation accounted for in the uncertainty assessment.

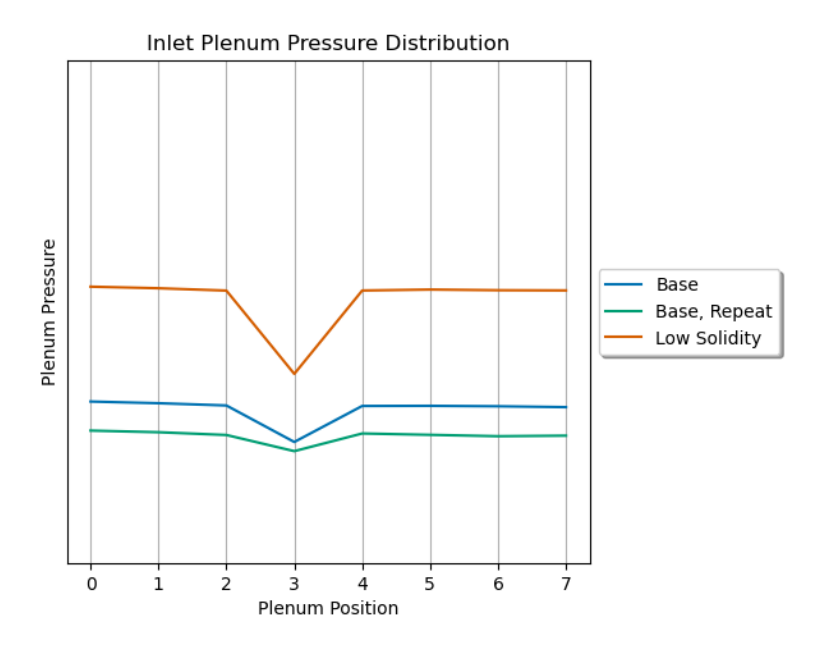


Figure 113: Inlet Plenum Pressures, Design Point

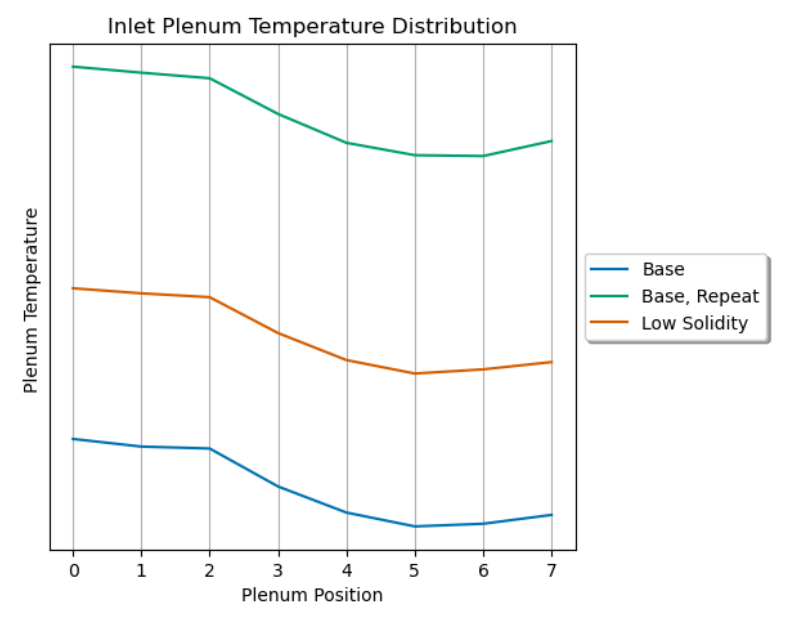


Figure 114: Inlet Plenum Temperature Distribution

5.4.3.2 Cascade Operating Conditions

As discussed in Section 5.4.2.2, ambient temperature and pressure affected the absolute pressures and temperatures of each test. This variation affects the Reynolds number of the test, with approximately a 6% worst case variation in Reynolds number. The impact on test results due to this variation is considered negligible.

During test execution, it was observed that the operating point of the rig was sensitive to the position of the traverse probe, as shown in Figure 115. This is due to several of the downstream static taps being in the traverse arc of the probe. When the probe is near a static tap hole, the value is affected by the pressure field around the probe and affects the reported downstream pressure. When controlling to the pressure ratio across the nozzle, the control system then attempts to compensate. As the time response of the system is significantly higher than the transit time of the probe across the pressure tap, this drives instability in the control system. To mitigate this, the rig pressure ratio was always set with the probe fully retracted. During the traverse, to avoid control system oscillations, the rig was controlled to the upstream plenum pressure, and ambient pressure was monitored to ensure significant variations (>0.05psia) did not occur during the traverse time period.

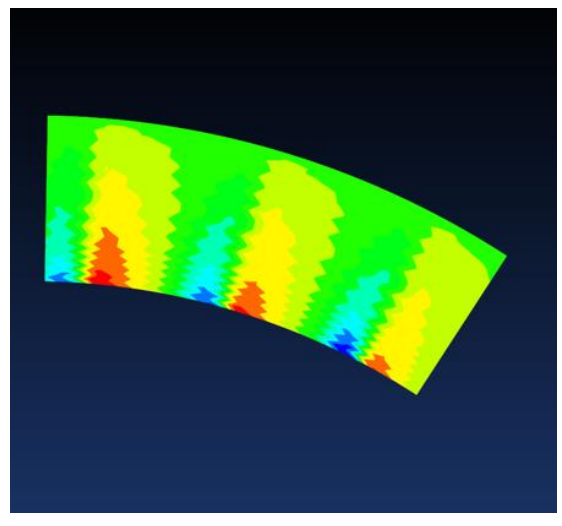


Figure 115: Reported Downstream Pressure as a function of Traverse Probe Position

5.4.3.3 As Tested Hardware vs Design Intent

Prior to testing, all throats were measured with taper gauges to quantify the as-built throat areas as compared to design intent. These measurements were repeated after testing to ensure that no permanent deformation occurred during testing. Throats were generally consistent, except where a seam between segments was present. This is due to the thickness of the RTV used in the seam. To prevent this, a larger nominal gap between segments should have been used to meet design intent.

Good agreement was seen pre-test to post-test in the throat measurements, indicating that no plastic deformation occurred during testing. Taper gauge measurements are sensitive to operator variation and slight mispositioning of the taper gauge can result in a reading that differs from the expected nominal. To better quantify the absolute area, an optical scan was completed of both parts to provide a quantitative comparison of throats. Both parts were found to have throats slightly large to nominal, though similar to each other, which was driven by the throats at the seams of the test article. This analysis was performed by fitting a minimum area surface into the optical scanned throat passages for each test article. As this is a manual process, only a subset of throats was directly measured – all throats on a seam were measured due to the variation caused by assembly, and half the remaining throats A Monte-Carlo analysis was performed based on the statistical variation of the measured throats to quantify the expected full annulus throat areas.

In addition to the physical throat measurements, a structural analysis was performed to determine the effect of pressure loads on the throat areas at operating conditions. Results from the deformed analysis were compared to the undeformed nominal. The resulting change in flow due to deformation at the throat for each test article was well within measurement uncertainty. The trailing edge deflected under load, tending to open the throat passage, however this effect was balanced by a slight bulging of the suction side of the airfoil under the internal pressure load from the cooling flow. The net effect of these deformations was to hold the deformed throat area nearly constant during testing.

5.4.3.4 Data Corrections

Following completion of all testing, additional corrections to the data were performed. The rig discharges to ambient conditions, and as the data was acquired over the course of several months, changes in temperature and pressure prevented direct comparison of measured values between test points. To facilitate these comparisons, all data was corrected to standard day conditions of 101.325kPa (14.696 psia) and 15°C (59°F).

Corrections to the recorded angle were required for the baseline nozzle repeat testing performed in October. During testing, the probe was removed and reinstalled while troubleshooting the readings. The probe was re-installed by a different operator than had originally installed the probe for the low solidity testing and the beginning of the baseline testing. Upon resuming testing, an offset in the angle was immediately noted. Following completion of the testing, the original operator was asked to re-zero the probe to determine the difference due to operators. This offset was found to be \sim 4°, matching well with the offset noted on the day of test. The adjusted data resulted in the measured exit angle comparing well with pre-test predictions and the low solidity data that had already been acquired.

5.4.3.5 Sources of Additional Uncertainty

No corrections were directly applied for the cracked inlet probe discussed in Section 5.4.3.1. Instead, this issue increases uncertainty of the true upstream pressure, and is added to the uncertainty stack for this test. This results in an additional one-sided uncertainty for each case. As a leaking probe would result in lower pressure readings than the true value, resulting in reduced calculated losses, this additional uncertainty is applied in a one-sided manner, to the downside of performance only.

This uncertainty also propagates to flow function, as the upstream pressure is used to calculate this parameter. The additional uncertainty in flow function due to this leakage is simply the difference between the average calculated during test, and the average of the seven probes without leaks. Similar to the performance uncertainty, this uncertainty is one-sided. Since a higher inlet pressure results in a lower flow function, the additional uncertainty is added to the negative side of the error band only.

5.4.4 Data Discussion and Comparison to Analytical Models

5.4.4.1 Flow Function Results

Flow function results are shown in Figure 116 and Figure 117. Figure 116 shows the full pressure ratio sweep taken during testing. The low solidity test article shows lower flow function throughout the pressure ratio sweep, though the variance from the baseline decreases as pressure ratio increases. Note that the 1D model predictions for the low solidity are omitted in Figure 116 for clarity but are included in Figure 117.

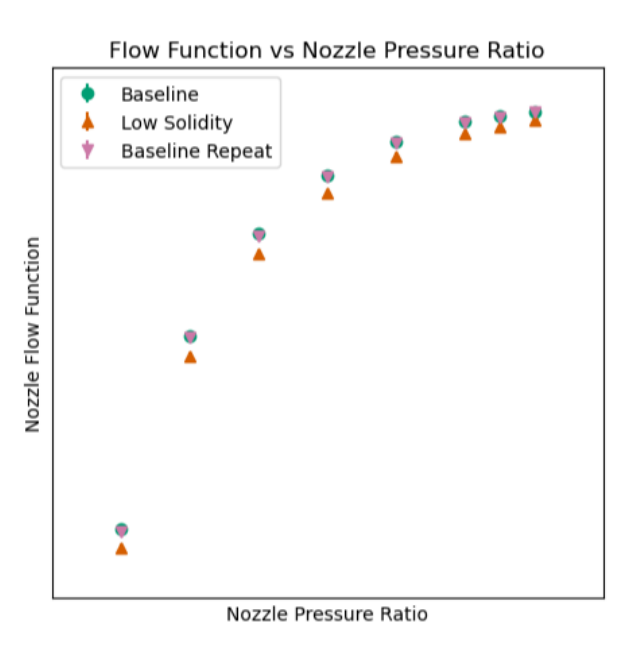


Figure 116: S2N Flow Function, Full Pressure Sweep

Figure 117 shows the same data with the addition of 1D model predictions for the low solidity, zoomed in to be able to resolve the error bars of the measurement and differences between the test articles near the design point. At the design point, the baseline flows as predicted by the 1D turbine meanline model. The low solidity test article flows approximately 1% low compared to the baseline test article. Pre-test predictions indicated the low solidity was expected to flow slightly low as discussed in Section 3.4. The 1D model predictions for low solidity account for this expected difference. Quantifying the difference in flow function from the expected flow for each solidity was a desired outcome of the test and is summarized in Table 40. This result will be incorporated into future design iterations for the compact core and vision product.

Table 40: Flow Function Results

	Flow Difference from 1-D Expectation		
Baseline	0.1%		
Low Solidity	-0.6%		

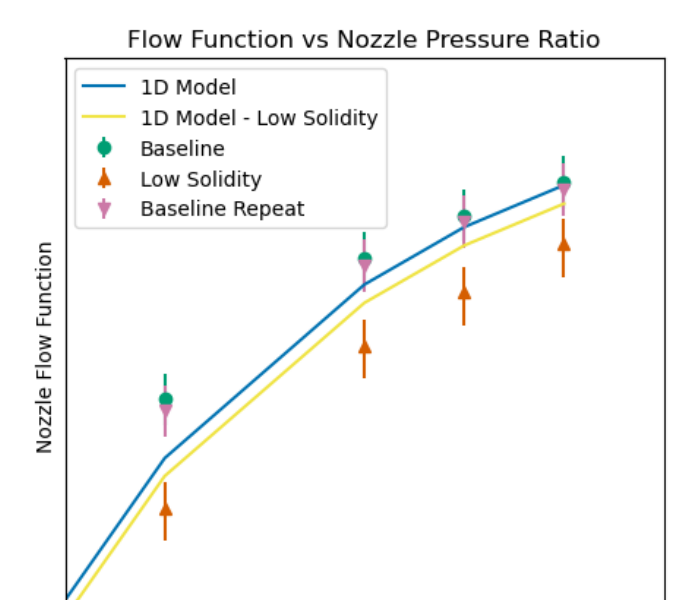


Figure 117: S2N Flow Function, Near Design Point

Nozzle Pressure Ratio

As the coolant is added post throat, little to no effect on flow function is expected. Definitionally, post throat cooling is not accounted for in the flow function for the blade row it is introduced in – the mass flow addition and the effect on flow function is accounted for in the downstream row. Any difference in flow function measured by this definition would be due to blockage from the introduced cooling propagating upstream of the throat and affecting the flow coefficient of the nozzle. No significant differences were noted in the flow function for each cooling case for each test article, as shown in Figure 118.

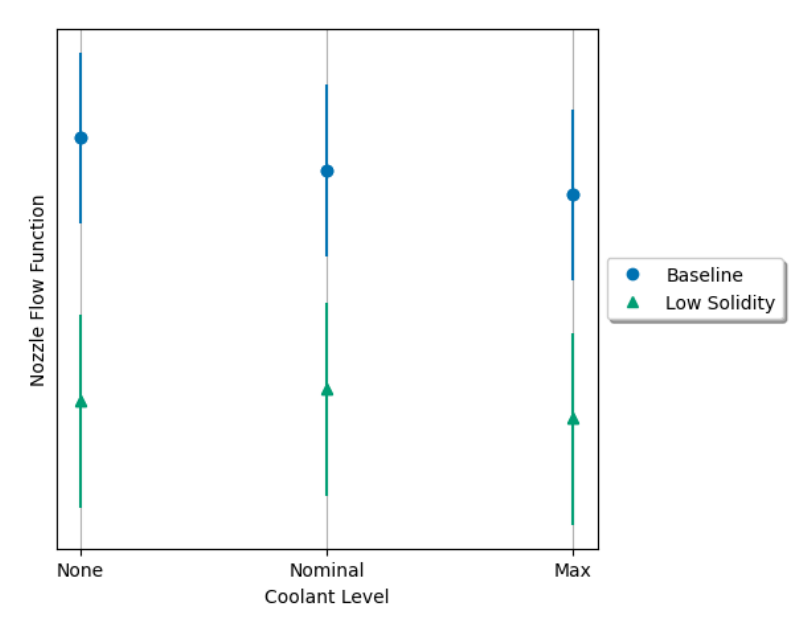


Figure 118: Effect of Cooling on S2N Flow Function

5.4.4.2 Nozzle Performance Results

Nozzle performance data is obtained from the downstream traverse data. The flow fields for each test article at the maximum coolant flow condition are shown in Figure 119 through Figure 122. From these flowfields, the differences in vortexing between the airfoils can be seen in both the wake shape and the distribution of flow angle.

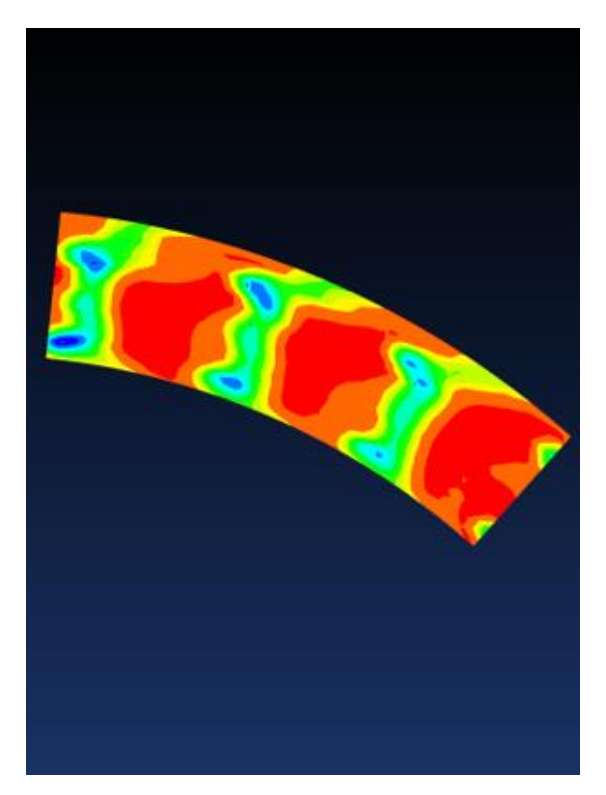


Figure 119: Baseline Contour, PT

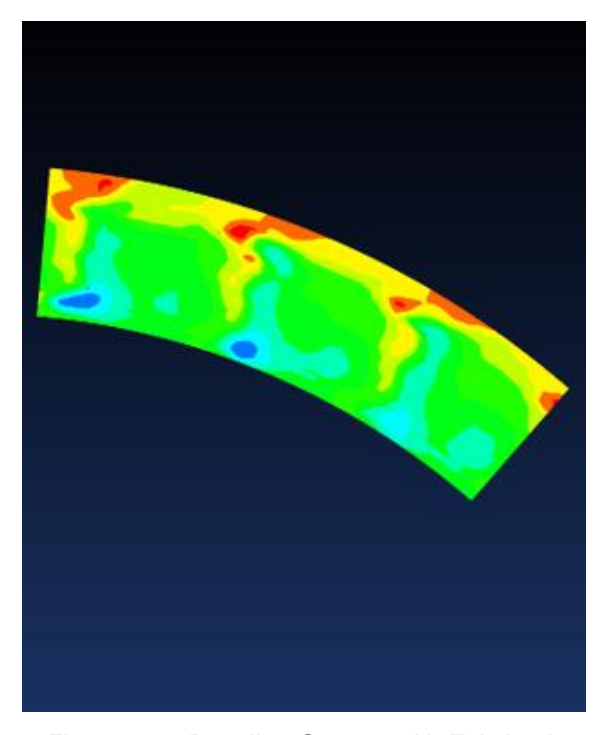


Figure 120: Baseline Contour, Air Exit Angle

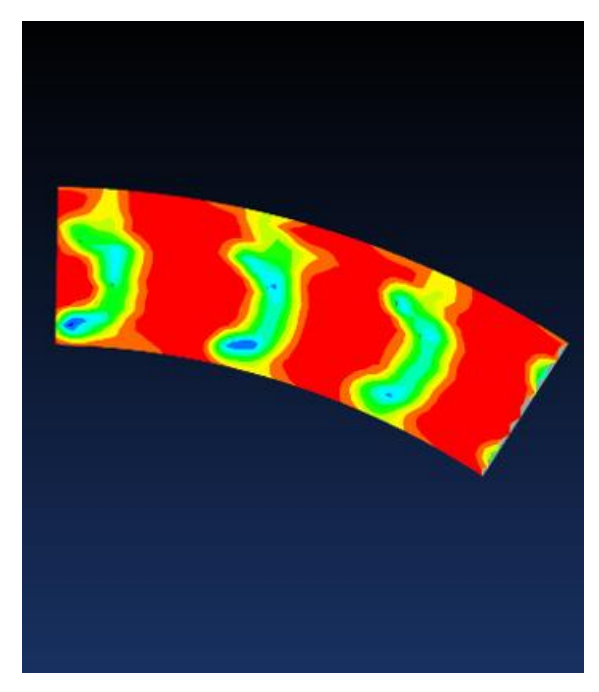


Figure 121: Low Solidity Contour, PT

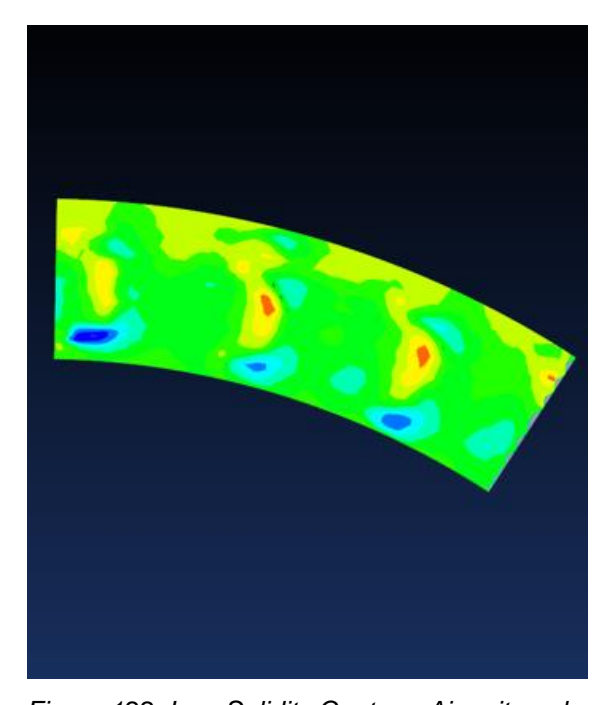


Figure 122: Low Solidity Contour, Air exit angle

The low solidity test article shows improved performance over the baseline as shown in Figure 123. The differences in measured value from baseline to low solidity are shown in Table 41, and the differences between cooling levels (from nominal cooling) are shown in Table 42. This improvement is greatest at the nominal cooling case, however the differences in performance between baseline and low solidity at the various cooling levels are within the uncertainty of the test. Notably, the trend of losses with addition of coolant is not monotonic, but rather a slight reduction in loss was observed when increased coolant levels were introduced. This effect is within the uncertainty of the measurements but did repeat consistently in both test articles and is similar to the results of the linear cascade testing. The most likely cause of this

reduction in loss at higher cooling flows is due to the higher momentum film energizing the suction side boundary layer.

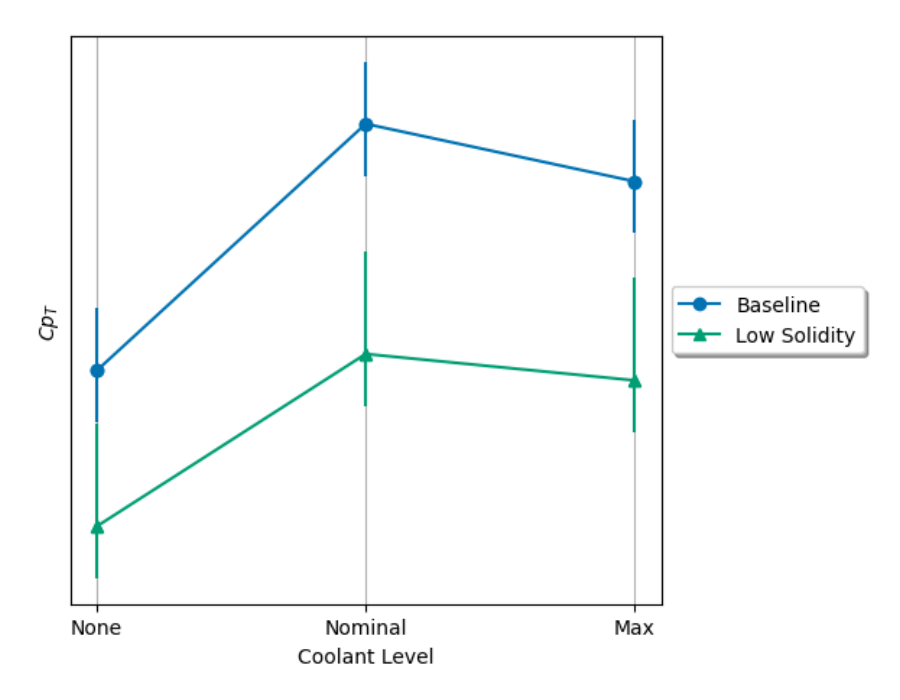


Figure 123: S2N Solidity Comparison of Loss

Table 41: Delta Loss for Solidity Changes

Cooling Level	$C_p,total$		
	[% improvement]		
No Cooling	9		
Nominal Cooling	11		
Max Cooling	10		

Table 42: Delta Losses for Cooling Changes from Nominal Cooling

Solidity	No Cooling	Max Cooling
	C _{p,total} [% improvement]	C _{p,total} [% improvement]
Baseline	12	3
Low Solidity	9	1

The radial profiles of the two test articles can be compared to further understand the differences in losses. Figure 124 shows the radial profiles of each test article and comparison to the pre-test CFD predictions for the no-cooling case to isolate the effects of solidity. In general, the pre-test prediction accurately predicted the trends observed in test, with the baseline outperforming the low solidity in the midspan, while the low solidity, due to its optimized vortexing mitigating the secondary flow losses, outperforms the baseline near the endwalls.

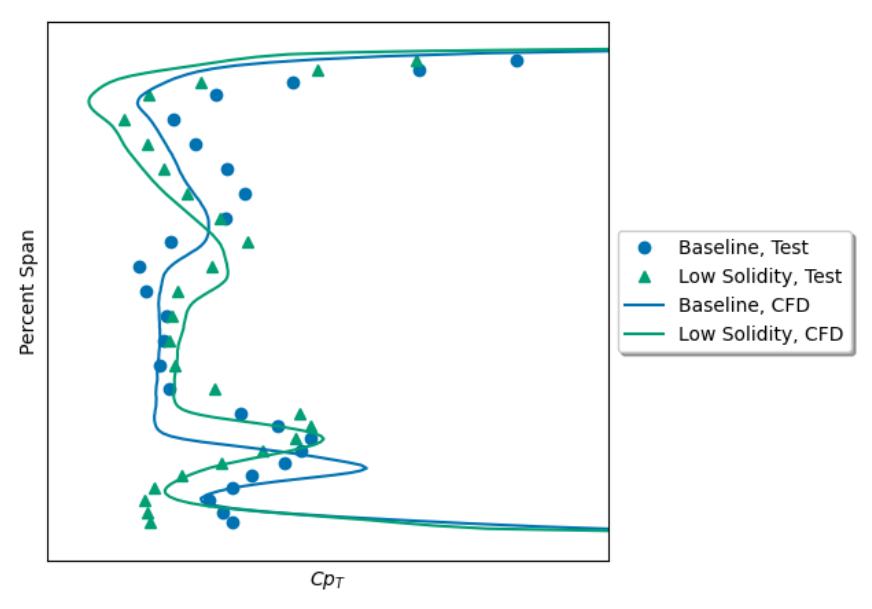


Figure 124: Radial Profile, Baseline Vs Low Solidity

Figure 125 further compares these profiles by taking the difference between the two profiles for both test data and CFD. Due to the presence of the endwall, the probe cannot capture the near wall region in the hub and the data shown are for spans 5% and below are extrapolated using boundary layer theory. In the figure, positive represents areas where the baseline outperforms low solidity. Points to the left of the CFD pre-test prediction indicate areas where the test data outperforms the prediction. Except very near the endwalls and in localized regions in mid-span, there is a slight improvement in performance in the test data over prediction throughout the profile. This accounts for the measurable performance benefit compared to the pre-test prediction that was within measurement uncertainty. The CFD was run as fully turbulent, however the rig runs at low inlet turbulence (~1.5%), and significant portions of the flow may relaminarize on the airfoil and reduce profile drag, which would be missed by the CFD analysis technique. More sophisticated turbulence models may improve the analytical assessment.

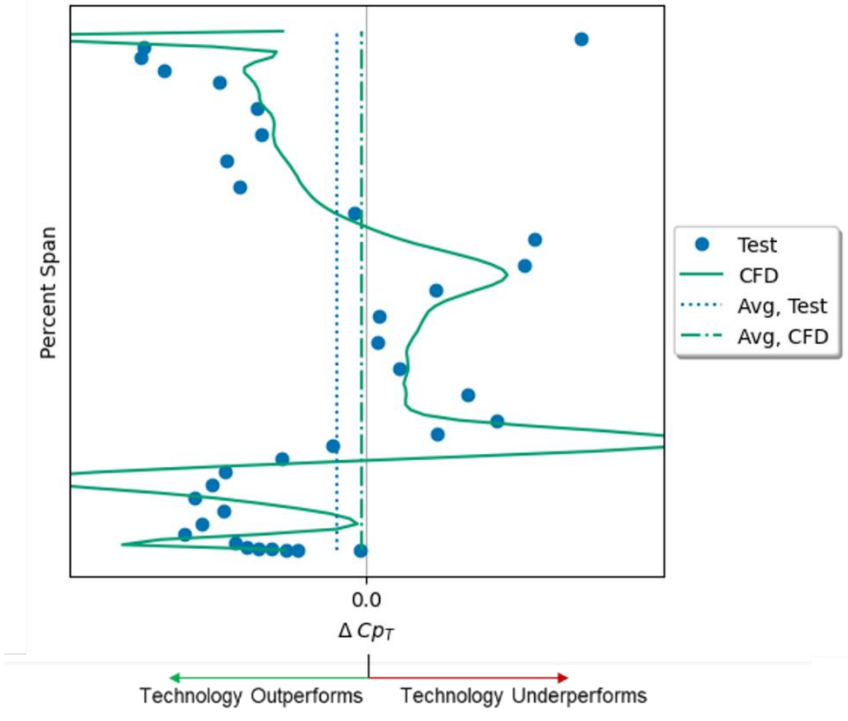


Figure 125: Radial Profile, △Cp_T, Solidity

Figure 126 and Figure 127 show the radial profiles for baseline and low solidity, respectively, at each cooling level tested. As expected, these profiles show that the cooling losses manifest throughout the span, except very near the endwalls, where limited coolant was present in the test articles. Additionally, the profiles align with the 1-D results, where the nominal coolant shows the greatest pressure loss across the span, with the maximum level cooling flow falling between the no-cooling case and the nominal cooling case.

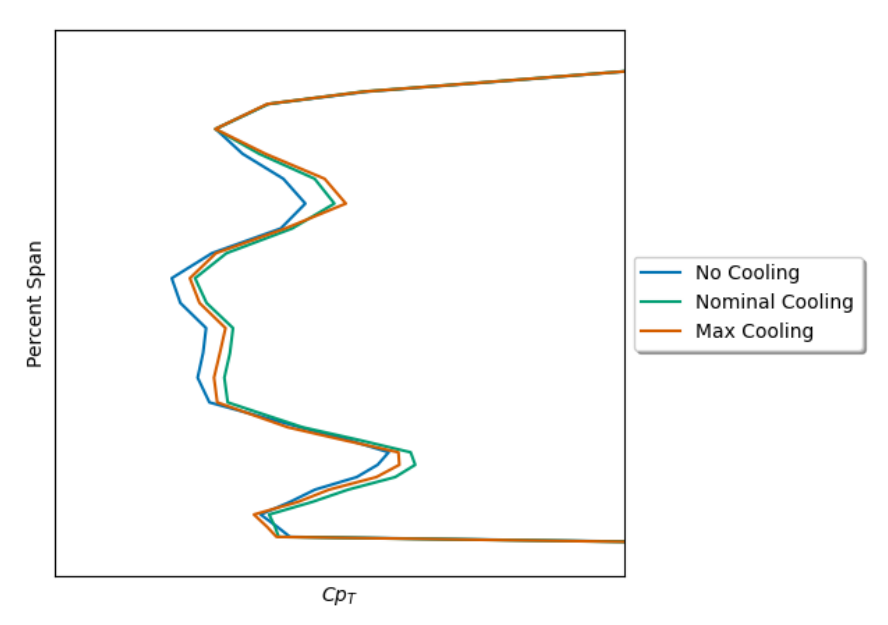


Figure 126: Baseline Loss for Various Cooling Levels

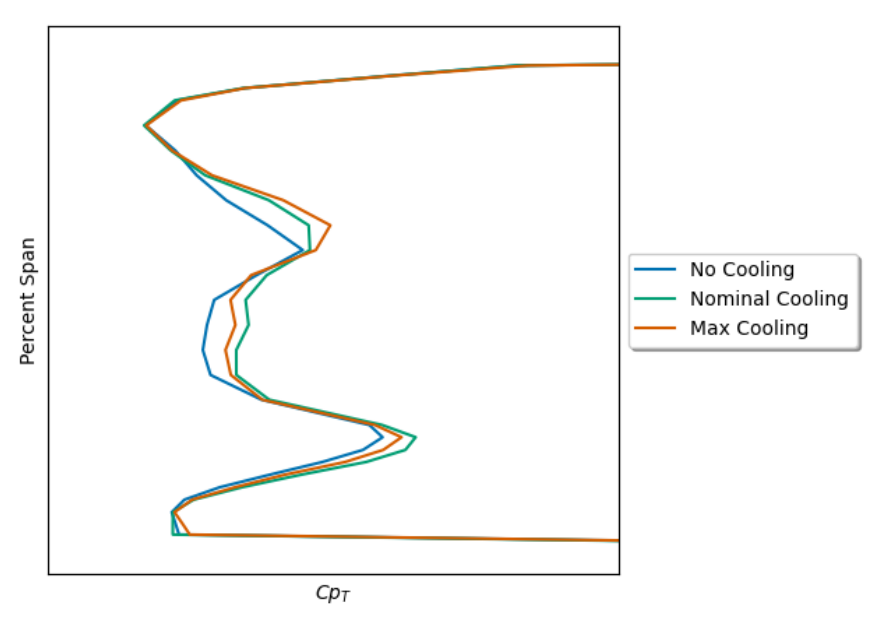


Figure 127: Low Solidity Loss for Various Cooling Levels

Comparing the delta profiles for cooling illustrates where the cooling loss is accumulating. As shown in Figure 128, in regions of the flow which are not near the spanwise location of cooling holes (i.e. near the endwalls), the difference in loss is near zero. In cooled regions that are unaffected by secondary flows, the offset of the loss approaches the levels measured in the linear cascade, which was only concerned with the 2-D region of the flow field. In regions affected by secondary flows, a lower delta loss is observed, indicating that cooling flows may not be greatly affecting the development and loss of the secondary flow features. Additionally, some of the film rows in the annular cascade are under the secondary flow roll-up zones, and are introduced into lower Mach number flows, which reduces the mixing loss. The integration of these regions yields a loss value that is lower than expected based on the linear cascade testing, however it is still a measurable benefit to eliminate cooling aft of the throat.

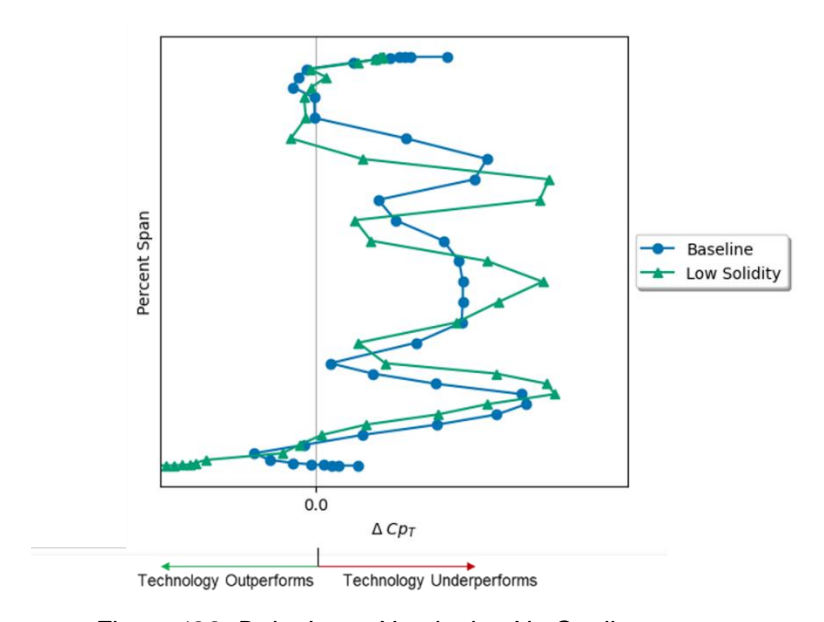


Figure 128: Delta Loss, Nominal to No Cooling

Lastly, the exit angles were compared to ensure that both airfoils provided similar levels of turning. Air exit angles as a function of span are shown in Figure 129 and summarized in Table 43. The profiles differ between the two test articles due to the different vortexing strategies between the test articles. CFD predicts the trends in air angle for each test article within the uncertainty of the measurement.

Table 43: S2N Exit Gas Angles

Solidity	Delta From Predicted		
	Angle		
Baseline	-1.1		
Low Solidity	0.0		

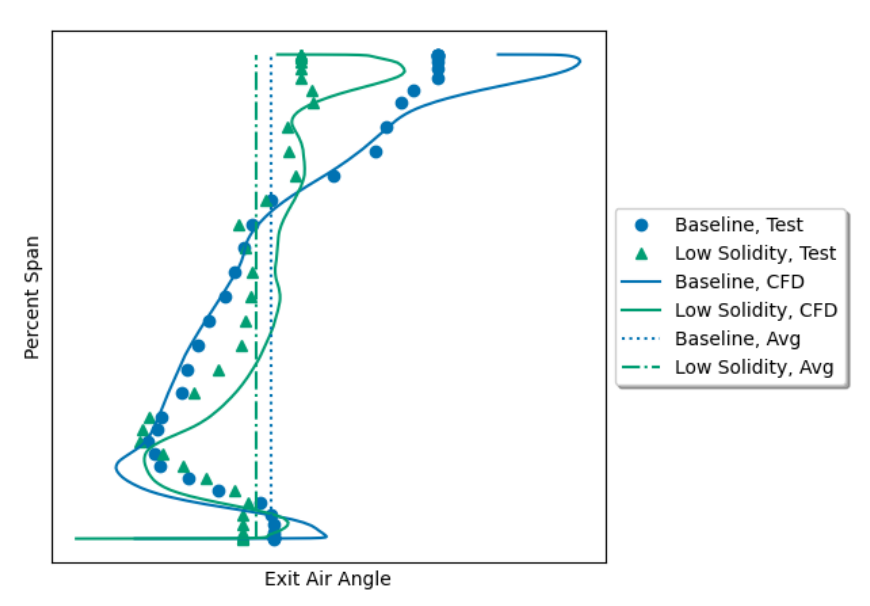


Figure 129: S2N Exit Air Angles

An important point is that for this test, the low solidity row was optimized in isolation. Moving towards higher fidelity rigs, the next step is to perform similar optimization with the full HPT to fully optimize the vortexing for low solidity for the full turbine. This optimization is likely to change the performance of each row as some rows may sacrifice performance to set optimal conditions for adjacent rows.

5.4.5 Test Conclusions

The test results indicate a significant improvement in performance for both low solidity and elimination of post-throat cooling. For assessment against the TPMs, these benefits must be allocated to the respective technologies. To do this, the post-throat cooling effect is taken using only the baseline test article data from nominal cooling to uncooled, representing an improved material system eliminating the need for cooling at this location. Then low solidity is considered by taking the difference in performance of the two test articles for the uncooled condition. This results in a Cp_T benefit of 1% for the compact core S2N technology and a Cp_T benefit of 0.6% for low solidity. The low solidity impact will be credited to both turbine nozzles when assessing against the TPMs in Section 6.

These results differ in magnitude from those measured in the CW22 linear cascade test. In that test, the cooling impact was greater, while the solidity effect was smaller. Solidity losses were successfully mitigated in the annular cascade with the inclusion and optimization of vortexing and stacking of the low solidity airfoil. Cooling losses were similar to the linear cascade in the 2D region in the midspan, but reduced where the vortex rollup zones covered the cooling holes, causing the flow to be injected into lower velocity regions.

6. Assessment Against Technical Performance Measures and Key Performance Parameters

The TPMs and KPPs which test results are assessed against are documented in Section 1.

6.1 Methodology

The impacts of the technologies, in terms of Cp_T measured in the test programs were each obtained by testing a single component in isolation, however the technologies will be applied across multiple locations in the turbine. For low solidity specifically, the results are split between nozzles and blades, as each type of component has unique design constraints – for example, the blade must withstand the high pull stress experienced in a rotating environment, which places constraints on how design sections are stacked. Thus, the achievable benefit is expected to vary for each type of component.

A GEA proprietary mean-line analysis tool was used to convert the pressure loss measurements from each technology into a change in HPT efficiency that can be applied in a cycle analysis. To globalize these results for comparison to the TPMs and KPPs, the benefit of each technology is applied to each relevant location at the same benefit as measured in test. As the tests were performed in isolation, no attempt to combine all technologies into a single turbine benefit value was made. It is likely that interactions between the various technologies affect the overall turbine (either beneficially or detrimentally) – understanding these interaction effects will be an effort under HyTEC Phase 2. For HyTEC Phase 1, each technology was independently assessed against a baseline turbine and the benefit of that technology to the turbine is reported.

For this effort, and for consistency with how the TPMs were developed, designs are considered weight and cooling flow neutral. Additionally, the same cycle level derivatives used to establish the TPMs were used to trade HPT efficiency with specific fuel consumption (SFC). To reach a fuel burn number, credit is taken for the savings of an improved SFC on the mission profile with a weight reduction from the need to carry less fuel. This vehicle level derivative is used to reach a final fuel burn reduction value.

6.2 Assessments

A summary of the assessments for each technology are shown in Table 44. Additional discussion on these assessments for each technology are discussed in the sections below.

Table 44: Aerodynamic Performance Assessment of Each Technology Against TPMs

Technology	Δ Fuel Burn [pts]	TPM Range Δ Fuel Burn [pts]
Low Solidity (Nozzles)	-0.12	-0.1 to -0.23
Low Solidity (Blades)	0.15	-0.1 to -0.23
Low Solidity (Combined)	0.03	-0.1 to -0.23
Tip Treatments	Indeterminate	-0.1 to -0.24
Platform Contouring	-0.0	0 to −0.05
Compact Core S2N	-0.11	-0.2 to -0.3

6.2.1 Low Solidity

Low solidity technology is assessed to meet the TPM range for HyTEC Phase 1. Low solidity technology is compared to current SoA application solidity levels. The expectation for low solidity entering the program, based on CFD analysis, was for a benefit in fuel burn of 0.1-0.23 percentage points. Low solidity was a technology on each of the tests under this program, with different effects attributable for nozzle and blade. For this assessment, low solidity is applied to all rows in the turbine, with both S1N and S2N based on nozzle test results and S1B and S2B based on the blade test results. Low solidity comparisons to TPM values, based on the meanline analysis and system level derivatives, are shown in Table 44.

Low solidity nozzles showed an aerodynamic benefit due to decreased profile losses combined with optimized three-dimensional aerodynamic design. The optimized design effectively managed the secondary loss mechanisms that are generally exacerbated as the solidity of a design is decreased. The measured benefits are above the minimum TPM goal for low solidity. Additional system level benefits from reduced cooling flows, not accounted for in these assessments, are also expected. As a design choice could be made to only insert low solidity where aerodynamic benefits have been demonstrated, the vane benefits alone satisfy the TPM objective.

Low solidity blades showed an increase in aerodynamic losses in the rotating rig, despite the reduced profile losses measured in the linear cascade environment. The additional design constraints inherent in designing rotating blade rows make managing the secondary loss mechanisms more difficult, as vortexing and stacking cannot be pursued as aggressively. Additionally, the specific test article used in this effort required aeromechanics compromises from the desired design. While aeromechanics will always be a design constraint, the mechanical arrangement for this test (a blisk) has a different response than would be expected for an inserted blade arrangement as is typical for an engine application. Additional multi-disciplinary optimization is expected to incrementally improve on the performance measured in this test; as such the results of this test can be considered a floor for the impact of low solidity blading. This blade was a first generation low solidity design; with the learnings from the HyTEC testing improvements to low solidity blades are expected to be realized. Potential changes for the next generation of low solidity blading include biasing the design towards negative incidence, and improving mid-span and tip losses where low solidity underperformed. With this understanding of the potential increase in loss when reducing blade solidity and expected improvements to the design, appropriate systems trades can be made for when the overall system level benefit warrants inclusion of the technology on a blade row by blade row basis. As the primary nonaerodynamic performance benefit for low solidity is a reduction in cooling, the expected benefit will be greater at S1B where coolant levels are highest, with lesser benefits expected for the S2B.

6.2.2 Advanced Tip Treatment

Advanced tip treatments are expected to meet the TPM range for HyTEC Phase 1, however additional work is needed to quantify the test result. Advanced Tip Treatments were compared to current SoA tip geometries. The expectation for advanced tip treatments entering the program, based on CFD analysis, was for a benefit in fuel burn of 0.1-0.24 percentage points. Tip treatments provide an aerodynamic benefit by reducing the strength of the tip vortex. Tip treatments were tested on the TRT rig on a rainbow blisk. Qualitatively the expected physics were measured and matched physics predicted by CFD analysis, however integration of the measured profile produced results inconsistent with the improved flow physics. The winglet geometry was used for the final TPM assessment. Based on available data the result is indeterminate, however GEA expects tip treatment benefits to be in line with the pre-program TPM predictions. The increased uncertainty from the previously undetected whirl mode, discussed in Section 5.3.3.2, means that the expected benefit cannot be fully substantiated with the data available at the time of this report.

6.2.3 Platform Contouring

Platform contouring is assessed to meet the TPM range for HYTEC Phase 1. Platform contouring is assessed compared to a traditional axisymmetric platform geometry. The expectation for platform contouring entering the program, based on CFD analysis, was for a benefit in fuel burn of 0.0-0.05 percentage points. Platform contouring was tested on the TRT rig on a rainbow blisk. Due to the relatively small benefit predicted, it was recognized that this performance change may be hard to discern from the test results. Due to the absence of predicted areas of measurable benefit, no performance credit can be taken for the technology. However, the data from FRAP pressure measurements does not show evidence of degraded performance. The technology is assessed at a neutral effect as shown in Table 44. This is within the pre-test TPM range for HyTEC Phase 1. Any future test that attempts to isolate the effect of platform contouring will likely need additional test design considerations in place to reduce uncertainty to a level that is able to clearly detect these small changes in performance.

6.2.4 Compact Core Stage 2 Nozzle

Compact Core S2N technology is assessed to fall below the TPM range for HyTEC Phase 1. Compact Core S2N is assessed for a compact core application by comparing the cooling arrangement that would be required by a traditionally manufactured CMC S2N in the expected cycle environment against an advanced manufacturing method, envisioned for this contract to be an advanced CMC, that would allow for coolant reduction. Specifically, for this assessment, it is assumed that the CMC nozzle could be adequately cooled while eliminating coolant introduction aft of the throat – no other changes in coolant level are assumed (i.e. any pre-throat cooling would be consistent between the designs). In addition, the cycle level benefit of the overall cooling reduction assumed by this approach is not accounted for in this assessment. The expectation for eliminating post-throat cooling for a compact core S2N entering the program, based on linear cascade data from a previous application, was 0.2-0.3 pts in fuel burn. The compact core S2N was tested in an annular cascade in GEA Cell A8. The estimated benefit from this technology is shown in Table 44.

The benefit measured from the elimination was smaller than anticipated, though still significant, as it was the largest benefit of any technology on a single component in the test program. However, as this result is only applicable to the single blade row it was tested on, the overall benefit does not increase when applied to the full turbine as is the case with the other technologies in this assessment. The primary reason for not meeting the minimum value of this TPM is an overly pessimistic estimation of the penalties associated with post-throat cooling in the pre-program assessment based on the previously available test data for legacy applications.

7. Technology Readiness Assessment

The goal of the present work was to mature each of the technologies to a NASA TRL 4 level, including achieving TRL 3 if not already performed. Entering the program, low solidity nozzles and blades were at TRL 2. Platform contouring and Advanced tips were each at TRL 3, while the compact core S2N was at a TRL 2 level. Each technology is assessed against the target TRL levels below.

7.1 Low Solidity

Low solidity blades and vanes were both demonstrated in a linear cascade during this test campaign, which is considered a TRL 3 environment. For each, performance trends were accurately captured and improved performance was observed for both blades and nozzles for profile losses. Thus TRL 3 was achieved, and testing continued in a TRL 4 environment. For the nozzle, this was an annular cascade. The annular cascade successfully demonstrated that a reduced solidity nozzle could show improvement in performance over the baseline SoA solidity, and that low solidity nozzles are considered to be at a TRL 4 level.

Low solidity blades were demonstrated in a TRL 4 rotating rig environment. Unlike the nozzles, the blades did not show a performance benefit, however they did successfully operate in the rig and the performance was quantified. As systems trades are expected to offset the aerodynamic penalties on the blades, low solidity blades are considered to have met NASA TRL 4 at the demonstrated performance debit. Low solidity technology is considered ready to continue development towards TRL 6.

7.2 Advanced Tip Treatments

Advanced tip treatments were at TRL 3 entering the program, due to previously completed proof of concept demonstrations and usage on other engine programs. This technology was demonstrated in the rotating rig TRL 4 environment and while the results cannot be quantified at this time, the technology is expected to meet the expected performance benefit. Thus, GEA expects that the technology will be considered to have met NASA TRL 4 based on this test program and be ready to continue development towards TRL 6.

7.3 Platform Contouring

Platform contouring was at TRL 3 for a compact core entering the program based on use in various GEA products. The technology was tested in the rotating rig TRL 4 environment. Due to the relatively small magnitude of the predicted benefit for the technology, no improvement could be definitively measured. However, evidence of performance degradation was not noted for this application, and the performance met the minimum TPM range. Thus, the technology is considered to have met NASA TRL 4. As the isolated benefit is difficult to measure in the rotating rig environment due to achievable uncertainty levels and based on success with endwall contouring on other GEA applications, platform contouring technology is considered ready for development towards TRL 6.

7.4 Compact Core Stage 2 Nozzle

The compact core S2N entered the program at TRL 2 due to the unique design requirements and limited test data on the effects of post-throat cooling. This technology was first demonstrated in a TRL 3 linear cascade environment, where the expected benefit was measured. Based on the results of this testing, the technology was considered to have demonstrated TRL 3 and testing continued at a TRL 4 level. In the TRL 4 annular cascade, a benefit was measured for removal of the post-throat cooling, but with the additional flow physics accounted for in the annular rig, the benefit was at a reduced level from that measured in the linear cascade. This technology is considered to have demonstrated NASA TRL 4 at the reduced benefit observed in test and is ready to be developed to TRL 6.

8. Technology Maturity Plan

Through the present effort and parallel test programs, the HPT aerodynamic technology suite has been advanced to TRL 4.

By reaching NASA TRL 4, the technologies have been demonstrated to function in isolation, and the performance impacts in the isolated environment have been quantified. The primary risk to these technologies moving forward is how the benefits will stack when used in combination in close proximity to other technologies which are trying to affect the same flow physics.

The focus of the remaining test program is to understand interaction effects, culminating in the demo core. Technologies will be matured in a stepwise manner, adding complexity in a controlled manner to understand the interaction effects as multiple technologies are combined. This will start in single stage demonstrations of interacting technology, building complexity as technology maturity increases. Then, a full two stage HPT design will be demonstrated in a performance rig to quantify the expected performance level for the turbine that will be included in the demo core.

As a parallel effort, interactions between turbine technologies and adjacent engine modules will be investigated. The primary region where interaction effects must be understood is in the combustor-S1N interface.

The efforts above will mature the technology suite to a TRL 5 level. Inclusion in the demo core will demonstrate inter-operability with remaining core modules. This includes compressor and combustor operability as well as operation in the representative thermal environment. This demonstration will mature the technology suite to TRL6.

9. Conclusion

A comprehensive test campaign was conducted in partnership with NASA Glenn to mature advanced HPT aerodynamics technologies to TRL4. The test campaign successfully met the goals of the program. Additionally, further understanding of loss mechanisms and flow physics was obtained thanks to the detailed measurements made possible by the test teams at NDTL, GEA, and NASA Glenn. GEA will develop a comprehensive suite of technologies that are well positioned to advance the state of the art for next-generation HPT designs.

Appendix A – Lessons Learned

Lessons Learned - CW22 S2N

While testing successfully met all key objectives, several issues were identified throughout the test campaign. The issues were mitigated as they occurred, enabling the test to proceed and meet all requirements. Lessons learned were documented and shared across GEA and NASA. Some of the lessons learned collected during the test campaign are described below.

	Impact to Test Execution	Lesson Learned
Test Plan	Reconfigurations add additional time to test schedule.	Employ a test plan that minimizes reconfigurations
Turbulence Grid	Characterizing turbulence grid adds additional time to test schedule.	Select a pre-characterized grid or plan 2-3 months to characterize new grid
COBRA Disk Space	Additional time needed to replace COBRA disk.	 Ensure sufficient storage space on data system to complete planned runs
Test Facility Mating Hardware	Additional time needed to remachine hardware.	 Fit check hardware for mating features at vendor when possible Require more detailed inspection when fit check not possible
Coolant Temp Control	Some variability in coolant temperature observed.	 Install a heat exchanger immediately before coolant enters blade
Cooling Points	Specifying coolant pressure ratios may create feedback loop from coolant/main flow interactions.	 Consider specifying target mass flow instead of pressure ratio for cooling holes
CO2 Tank	Vacuum jacketed tank made tank setup process easier.	 Lease vacuum jacketed tank instead of foam jacketed tank (requires refrigeration system)
Test Article Leakage	Needed to retake three sets of data. Had to machine test articles to mitigate leakage.	 Leak check prior to testing and seal any leaks Use flexible epoxy or gasket to allow for hardware deflection from coolant pressure Improve assembly process of additive airfoils with sidewalls
Throat Measurements	Inconsistent measurement process introduced variability.	Create repeatable process for measuring throats consistently
Traverse Probe Bow Wave	First 1/3 rd of traverse survey shows non-periodic loadings.	Assess extent of potential bow wave interaction as part of check-out
Avoid Transonic Mach Region	Additional post-processing needed to correct individual data points.	Make shock correction process more robust
BOS	Troubleshooting needed to optimize set-up. Delay in receiving BOS data.	 Take reference image after running CO2 for BOS to post-process out thermal footprint Field-of-view for near-wall effects should be tighter around test article Have improved process to transfer massive datasets and test process ahead-of-time
Inlet Characterization Correction	Correction was required to account for offset C _{p,total} inlet profile, impacting downstream data.	 Characterize the inlet total pressure profile for every configuration to get most accurate inlet total pressure

Lessons Learned - CW22 S1B

While testing successfully met all key objectives, certain obstacles were identified through the test campaign. Obstacles were mitigated as they occurred, enabling completion of all test requirements. Lessons learned were documented and shared across GEA and NASA. Some of the lessons learned collected during the test campaign are described below.

	Impact to Test Execution		Lesson Learned	
As-Manufactured Geometry Miss	Initial CFD predictions did not account for different throat area (inconsistency from scaling)	•	Account for correct scaling process in test article design Update models to most accurately represent as-tested hardware	
Turbulence Grid Blowing Ratio	Test team had to examine inlet characterization data to determine optimal blowing ratio for both Reynolds numbers	•	Test all Reynolds numbers in test matrix to optimize turbulence grid blowing ratio during inlet characterization	
Coefficient of Static Pressure Loading	Re-processing of loading data necessary with different inlet Kiel	•	When loadings result in values of $C_{p,static}>1$, different inlet total pressure measurement should be used	
Data Blips/Spikes	Erroneous points in data results affect post-processing averages and should be removed (or data set not used)	•	Valve sticking results in non-physical blips in survey data. Should be updated in cell before future testing.	
Cascade Resonance	Exit valve position swinging open and closed made it difficult to acquire quality data	•	Attributed to flow resonance. Avoid specific geometry configuration and flow conditions that cause resonance	
Exit Swirl Variation	Required repeat of test cases with skewed exit swirl with new test section blockage configuration	•	Refrain from using upper blockage board extensions that protrude past exit metal angle of test articles. Keeping Blade 1 in the test section produced best results.	
PSP Data Acquisition/Post- Processing	See Below	•	See Below	
Probe Mach Number Correction	Additional post-processing needed to correct individual data points	•	Correct shock correction algorithm to calculate the correct free stream Mach number	

The following describes the Lessons Learned from the PSP objective of the test.

1) Non-Uniform Lighting

- a. Discussion: Use of the data analysis ratio Iref/I was not possible due to non-uniform lighting in the cascade, resulting in an insufficient level of correlation between analyzed PSP data and observed absolute pressure values. The root cause of non-uniform excitation of pressure sensitive paint was the delivery of light on the same axis as data collection.
- b. Recommendation: Lab environment testing should be continued to determine if image quality can be improved by increasing the number of frames collected and decreasing exposure time of each frame.

2) Fiducial Size and Location

a. Discussion: Fiducials were added to the test articles to enable image alignment and shift correction (Figure 130). Fiducials are removed during image processing to display only PSP information. Fiducials were placed too close together, reducing the number of pixels

- available for replacing the fiducials with interpolated data. As a result, the quality of interpolated data replacing the fiducials was questionable. Secondly, the size of the fiducials made it difficult to align them to a single pixel.
- b. Recommendation: Keeping fiducials as small as possible will improve interpolated data quality. Placing fiducials in specific recorded locations will help de-warp the data image more precisely.

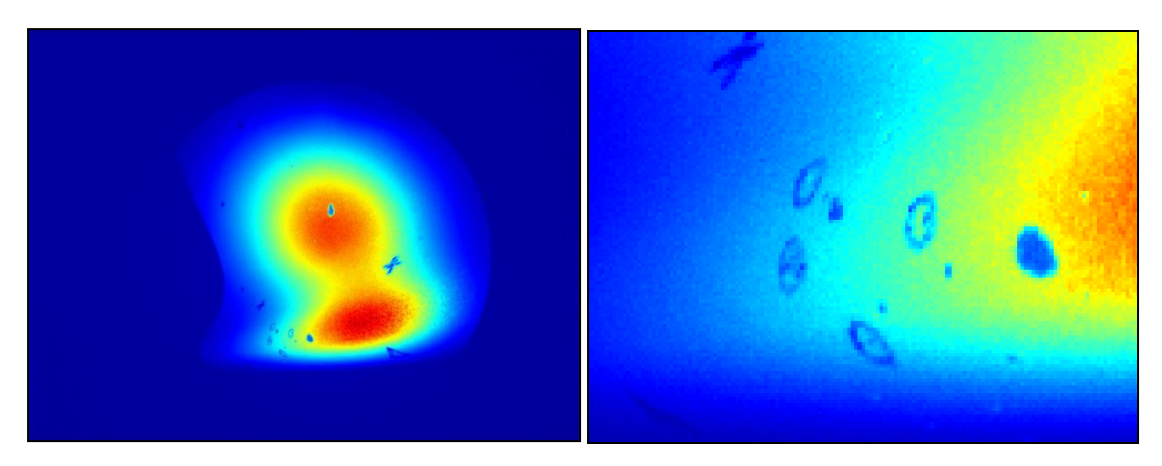


Figure 130: Fiducials and Static Pressure Taps Close-Up

3) Fiducial Proximity to Pressure Taps

- a. Discussion: Fiducials surrounding the pressure taps diminished the confidence level of the values interpolated near the static pressure taps. In turn, this decreased confidence of mean static pressure value surrounding the pressure taps.
- b. Recommendation: Use a data imager with resolution high enough to see pressure taps within the data. Record pressure tap location within image. Use pixels surrounding pressure tap to remove visible pressure tap with interpolation and generate a mean value at the pressure tap.

4) Image Distortion Created by Vibration and Frame Rate

- a. Discussion: The vibration of the equipment and long exposure time created blurry fiducials and nearly invisible pressure taps within the data. The result was questionable image alignment, as shown in Figure 131.
- b. Recommendation: Lab environment testing should be continued to determine if image quality can be improved by increasing the number of frames collected and decreasing exposure time of each frame.

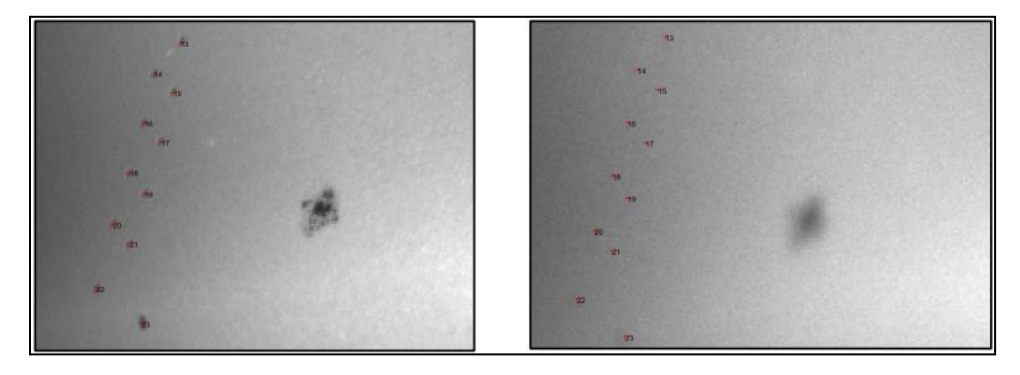


Figure 131: Wind-off Condition (left) and Wind-on Condition with Vibration (right)

5) Non-Stereo Parallax Removal

- a. Discussion: Parallel lines on airfoil no longer parallel when collected as a 2D data image. Current NASA data processing software to remove parallax could not be applied to dataset since there were no usable reference lines on the test article.
- b. Recommendation: Improve NASA method to allow a parallax removal transformation based solely on the visible portions of the airfoil.

6) Insufficient Agreement between PSP Ratios and Absolute Pressures

- a. Discussion: The data could not be collected in a manner capable of being processed using the understood 'ratio-of-ratios' method. The result was an insufficient level of correlation between analyzed PSP data and observed absolute pressure values.
- b. Recommendation: Improve calibration and characterization of PSP by increasing number of wind-off reference images collected.

7) Improvement to Data Reduction Methods

- a. Discussion: A third data reduction method was attempted where fully processed data sets are accurate to within 5% of pressure tap data. The largest error source with the method is image alignment.
- b. Recommendation: Continue to develop this method to support future tests. Develop automated image alignment tools to support the method's success.

Test Lessons Learned - TRT

The final air period for this test campaign occurred on August 23rd, 2023. In hitting all key objectives there were issues which occurred throughout the test campaign. The team addressed these issues as they occurred in consultation with NDTL and GEA experts. This allowed the team to advance towards completion of the campaign, meeting the key objectives and gathering all required data. The events which lead to these lessons learned were categorized into major and minor events. The table below shows the major events which occurred, and the corrective actions taken.

Event	Description	Corrective Action
Drive Motor Failure	A drive motor failure occurred during the phase 1 test campaign. This was due to an overcurrent shorting the drive motor windings. This led to rapid degradation in life and eventually a smoke event.	Overcurrent condition severely degrades the life of the mag bearing windings. If an overcurrent condition is flagged, immediately ramp-down to safe speed. Ensure that NDTL has an inspection interval for the drive motor for health monitoring. Trends of the motor health are needed to assess if excessive degradation has set in.
Rotor Whirl	During test campaign, discovery of a synchronous whirl was found. If using FRAP measurements, the data will show a blade-to-blade variation in performance correlated to an open or closed clearance.	Ensure on build up, the position of the #1 blade, the blisk installation position (trilobe mounting), and tachometer are noted to later correlate specific blade tip clearance.
Surge Relief Valve	The previous surge relief valve was not positioned correctly during test. This led to an overcurrent situation. The relief valve's function is to open and allow atmospheric air to enter the sub-atmospheric main flow during an e-stop or overspeed condition. At ADP this valve is ~40% open.	A new surge relief valve was installed with an upgraded pneumatically powered actuator. Upon triggering, the valve opens from 0-100% within 0.8 second. This actuation would complete within the 5 second overspeed burst window, thereby reducing risk of main shaft overspeed.
CAP probes	Older aerogage probe boxes did not have sufficient bandwidth for the probes. The team discovered that CAP probe processing and hi-band amplifier units can get quite hot during a long test period. When the boxes reach a temperature above 85°F, TCL measurement accuracy degrades substantially.	Acquired and used new aerogage probe boxes having more bandwidth capability than the old boxes. This helped prevent bandwidth saturation with speed. Cooling vents in the cabinet were positioned to cool boxes. Temperatures were monitored during testing.
Drive Train	When operating at ADP speed with this specific rig configuration, there was evidence of a torsional mode. This was likely present for all builds and does not affect quality of data. The team identified a remote chance of overspeed due to shaft failure and implemented safeguards.	NDTL upgraded the surge relief valve actuation response time and integrated it into e-stop circuit to reduce system energy. An overspeed tachometer with fail safe speed monitoring was installed and updated in the programmable logic controller (PLC). This was installed in case an overspeed event will occur in the future. Audit performed of test cell overspeed protection features in the PLC.
Torquemeter	Reading data at a faster acquisition speed led to large variations in measured torque.	Signal filtering for the torquemeter was set to historic level (64ms).

	I	T
Thrust Piston (TP)	The TP needs all the capability of the compressor to successfully get to ADP speed.	Ensure that other White Field facility test cells are not using the TP compressor on TRT test days. NDTL has implemented facility physical lock outs and procedures to warn other cells of TRT testing.
Secondary Compressor	When the secondary compressor was turned off during testing the stability of mass flow readings was degraded substantially leading to large variations in measured mass flow.	Ensure the secondary compressor is turned on between 300-500 rpm during all rig data collection periods.
Purges	During test campaign a large leakage was found in the aft purge line after seeing an unusually low temp to torque reading. After the initial perfection review the purge hose and fittings were not inspected.	Ensure there are no leakages in purge flow lines between the orifice place and rig inlet location. Conduct purge line leak check with soap water prior to the rig being ramped up to ADP.
Safety	Smoke was observed in the test cell during rig startup. The test team inspected the rig and cell and ran another startup procedure to determine the source of the smoke. It was later determined that the drive motor had failed, and testing was halted.	An escalation matrix was developed to clarify when people outside the immediate test team should be consulted and/or notified.
Purge Cavity Line Orifice Plate Measurement Equation	After test audit found purge cavity flow orifice plate had the incorrect equation, resulting lower than measured mass flows calculated during testing.	Purge cavity equations have been corrected. Recommend performing an audit during mechanical checkout period to ensure current readings are calculated.

References

- [1] Thurman, D.R., Flegel, A., Giel, P.W., "Inlet Turbulence and Length Scale Measurements in a Large Scale Transonic Turbine Cascade," 50th AIAA/ASME/SAE/ASEE Joint Propulsion Conference. Cleveland, OH. July 28-30, 2014. https://doi.org/10.2514/6.2014-3934.
- [2] Langston, Lee. (2001). Secondary Flows in Axial Turbines—A Review. Annals of the New York Academy of Sciences. 934. 11-26. 10.1111/j.1749-6632.2001.tb05839.x.
- [3] Bliumentalis, D. (ed.) (2021) Heat Transfer Facilities, NASA Glenn Research Center. Available at: https://www1.grc.nasa.gov/facilities/erb/htf/#transonic-turbine-blade-cascade-test-facility-cw22 (Accessed: April 7, 2023).
- [4] Wernet, M., "Real-Time Background oriented Schlieren: Catching Up With Knife Edge Schlieren," *National Aeronautics and Space Association*, TM 2019-220144, 2019, https://ntrs.nasa.gov/citations/20190002831.
- [5] Giel, P.W., Thurman, D.R., Lopez, I, Boyle, R.J., Van Fossen, G.J., Jett, T.A., Camperchioli, W.P., & La, H. "Three-Dimensional Flow Field Measurements in a Transonic Turbine Cascade." Proceedings of the ASME 1996 International Gas Turbine and Aeroengine Congress and Exhibition. Volume 1: Turbomachinery. Birmingham, UK. June 10–13, 1996. V001T01A036. ASME. https://doi.org/10.1115/96-GT-113
- [6] Porreca, L., Kalfas, A., Abhari, R., Yun, Y., and Song, S., 2009, Interstate Flow Interactions and Loss Generation in a Two-Stage Shrouded Axial Turbine